MEMS Solutions For More Than Illumination

Li, X.

DOI
10.4233/uuid:9d197709-c5a2-4de4-86c0-f350c41b1660

Publication date
2020

Document Version
Final published version

Citation (APA)
Li, X. (2020). *MEMS Solutions For More Than Illumination*. [Dissertation (TU Delft), Delft University of Technology]. https://doi.org/10.4233/uuid:9d197709-c5a2-4de4-86c0-f350c41b1660

MEMS SOLUTIONS FOR MORE THAN ILLUMINATION

MEMS Solutions For More Than Illumination

Proefschrift

ter verkrijging van de graad van doctor
aan de Technische Universiteit Delft,
op gezag van de Rector Magnificus Prof.dr.ir. T.H.J.J. van der Hagen,
voorzitter van het College voor Promoties,
in het openbaar te verdedigen op

maandag 12 oktober 2020 om 10:00 uur

door

Xueming Li

MSc. Microelectronics
Peking University, Beijing, China,
geboren te Pingxiang, Jiangxi, China.

Dit proefschrift is goedgekeurd door de

Promotor: Prof. dr. G.Q. Zhang
Promotor: Prof. dr. P.M. Sarro

Samenstelling promotiecommissie:

Rector Magnificus,	voorzitter
Prof. dr. G.Q. Zhang,	Technische Universiteit Delft
Prof. dr. P.M.Sarro,	Technische Universiteit Delft
Onafhankelijke leden:	
Prof. dr. P.J. French,	Technische Universiteit Delft
Prof. W.D. van Driel,	Technische Universiteit Delft
Dr. ir. S. Vollebregt,	Technische Universiteit Delft
Prof. X.J. Fan,	Lamar University
Prof. C. Bailey,	University of Greenwich

Prof. dr. G.Q. Zhang en Prof. dr. P.M.Sarro hebben in belangrijke mate aan de totstandkoming van het proefschrift bijgedragen.

Keywords: tunable optics, PM $_{2.5}$ detector, PDMS/CNT, fresnel optics

ISBN 978-94-6421-064-4

An electronic version of this dissertation is available at
http://repository.tudelft.nl/.

To my family

CONTENTS

SUMMARY

The development of solid state lighting (SSL) has been involving with improving the luminaire efficiency and integrating non-luminous functions, also known as *More than Illumination*. The objective of this thesis is to investigate different solutions for the concept of *More than Illumination* for SSL applications, to combine general lighting with additional functions. Several distinct topics were explored to serve this purpose, in different forms of SSL packaging. In a higher packaging level, we studied integrated tunable optical system with existing lighting sources, to achieve desired beam shaping, which can be helpful for dynamic lighting applications. In a lower level, a sensor that can be integrated with the lighting system was also explored. Furthermore, we developed a new form of fresnel lens which can be mounted on the LED chip.

The thesis starts with exploring the tunable optics for lighting applications in chapter 2. A tunable optical system with an electromagnetic actuator fabricated on a flexible substrate was demonstrated. The electromagnetic actuator consists of a copper coil and polyimide beams, with a ring shape permanent magnet as the magnetic flux source. When applied with a DC voltage, the Lorentz force generated on the coil drives the polyimide substrate along with the mounted optics, which in turn controls the beam shape. The working principle was simulated in Tracepro to estimate the light distribution change for the light source. The simulation was validated by the following tests on the optical system, which demonstrated that the outgoing angle of the light changed accordingly with the applied voltage.

Apart from the general lighting applications, lighting is also expected to play an essential role in the sensory network for IoT applications. In chapter 3, a sensor for particulate matter (PM) detection which can be integrated into the lighting products was demonstrated. The sensor chip is made by microfabrication methods. It works by capturing the scatter light triggered by particles flowing through a microchamber. The microchamber consists of two submounts with cavities, assembled with a laser diode and a photodiode separately. The chip is also accompanied by an external commercial air flow generator to help the air flow through the microchamber. The principle of this work is validated by exposing the sensor to cigarette smoke, one of the most common sources of $PM_{2.5}$. The sensor output is higher in the presence of cigarette smoke than in clean air

While the previous chapters were focusing on the external applications, in chapter 4, a micro size optical component was developed, which can be mounted on the LED chip for optical beam shaping. The proposed optics is a micro Fresnel lens, fabricated by encapsulating lithographically defined vertically aligned carbon nanotube (CNT) bundles inside a polydimethylsiloxane (PDMS) layer. The composite material combines the excellent optical absorption properties of CNT with the transparency and stretchability of PDMS. By stretching the elastomeric composite in the radial direction, the focal length of the Fresnel lens is tuned accordingly. A good focusing response was demonstrated and a broad focus range was achieved by stretching the lens radially.

In chapter 5, we continued to explore the property of CNT/PDMS composite. With the same format of vertically aligned CNT infiltrated in PDMS as in the previous chapter, the electric property of the composite is investigated for the potential application in flexible interposer. It is based on the PDMS as support material, while the embedded vertically aligned CNT bundles serve as conducting vias with its electrical conductivity. The composite combines the flexibility of the elastic material and the conductivity of the CNTs. The resistivity of the composite much smaller than the resistivity of PDMS, yet its electrical performance falls short of expectations, thus further research is required to improve the electrical properties, including coating the CNT with conductive materials. Furthermore, the material properties, such as mechanical property are also required to be investigated in future work.

SAMENVATTING

De ontwikkeling van solid-state verlichting (SSL) omvatte het verbeteren van de armatuurefficiëntie en het integreren van niet-lichtgevende functies, ook wel bekend als *More than Illumination*. Het doel van dit proefschrift is om verschillende oplossingen te onderzoeken voor het concept van *More than Illumination* voor SSL-toepassingen, om algemene verlichting te combineren met aanvullende functies. Verschillende onderscheidenlijke onderwerpen werden onderzocht om dit doel te bereiken, in verschillende vormen van SSL-verpakkingen. In een hoger verpakkingsniveau hebben we een geïntegreerd instelbaar optisch systeem met bestaande verlichtingsbronnen bestudeerd om de gewenste bundelvorming te bereiken, wat nuttig kan zijn voor dynamische verlichtingstoepassingen. Op een lager niveau werd ook een sensor onderzocht, die kan worden geïntegreerd met het verlichtingssysteem. Verder hebben we een nieuwe vorm van de fresnel-lens ontwikkeld, die op de LED-chip kan worden gemonteerd.

Het proefschrift begint in hoofdstuk 2 met het verkennen van de afstembare optica voor verlichtingstoepassingen. Een afstembare optiek met een elektromagnetische actuator gefabriceerd op een flexibel substraat werd in dit hoofdstuk gedemonstreerd. De elektromagnetische actuator bestaat uit een koperen spoel en polyimidestralen, met een ringvormige permanente magneet als magnetische fluxbron. Wanneer toegepast met een gelijkspanning, drijft de Lorentz-kracht die op de spoel wordt gegenereerd het polyimidesubstraat aan, samen met de gemonteerde optica, die op zijn beurt de straalvorm regelt. Het werkingsprincipe werd gesimuleerd in Tracepro om de verandering van de lichtverdeling voor de lichtbron te beoordelen. De simulatie werd gevalideerd door de volgende tests op het optische systeem, die aantoonde dat de uitgaande hoek van het licht overeenkomstig veranderde met de aangelegde spanning.

Naast de algemene verlichtingstoepassingen, zal verlichting naar verwachting ook een essentiële rol spelen in het sensorische netwerk voor IoT-toepassingen. In hoofdstuk 3 werd een sensor voor fijnstof (PM) detectie gedemonstreerd, die geïntegreerd kan worden in de verlichtingsproducten. De sensorchip is gemaakt door middel van microfabricagemethoden. Het werkt door het verstrooiingslicht op te vangen dat wordt veroorzaakt door deeltjes die door een microkamer stromen. De microkamer bestaat uit twee onderstellen met holtes, die afzonderlijk zijn samengesteld met een laserdiode en een fotodiode. De chip gaat ook vergezeld van een externe commerciële luchtstroomgenerator om de lucht door de microkamer te helpen stromen. Het principe van dit werk wordt gevalideerd door de sensor bloot te stellen aan sigarettenrook, een van de meest voorkomende bronnen van $PM_{2,5}$. Het sensorvermogen is hoger in aanwezigheid van sigarettenrook dan in schone lucht.

Terwijl de vorige hoofdstukken zich concentreerden op de externe toepassingen, werd in hoofdstuk 4 een optisch component van microformaat ontwikkeld, die op de LED-chip kan worden gemonteerd voor optische bundelvorming. De voorgestelde optica is een micro Fresnel-lens, vervaardigd door lithografisch gedefinieerde verticaal uitge-

lijnde koolstof nanobuis (CNT) bundels in een polydimethylsiloxaan (PDMS) laag in te kapselen. Het composietmateriaal combineert de uitstekende optische absorptie-eigenschappen van CNT met de transparantie en rekbaarheid van PDMS. Door het elastomere composiet in de radiale richting uit te rekken, werd de brandpuntsafstand van de Fresnel-lens dienovereenkomstig afgestemd. Er werd een goede scherpstelrespons aangetoond en er werd een breed scherpstelbereik behaald door de lens radiaal uit te rekken.

In hoofdstuk 5 is verdergegaan met het onderzoeken van de eigenschappen van CNT / PDMS-composiet. Met hetzelfde formaat van verticaal uitgelijnde CNT geïnfiltreerd in PDMS, zoals in het vorige hoofdstuk, werd de elektrische eigenschap van composiet onderzocht voor de mogelijke toepassing in flexibele interposer. Het is gebaseerd op het PDMS als ondersteuningsmateriaal, terwijl de ingebedde verticaal uitgelijnde CNT-bundels dienen als geleidende doorgangen met zijn elektrische geleidbaarheid. Het composiet combineert de flexibiliteit van het elastische materiaal en de geleidbaarheid van de CNT's. De soortelijke weerstand van de composiet is kleiner dan de soortelijke weerstand van PDMS, maar de elektrische prestaties voldoen niet aan de verwachtingen, dus verder onderzoek is vereist om de materiaaleigenschappen, zoals mechanische eigenschappen, te verbeteren.

1

INTRODUCTION

1

When I moved to my new house, the first thing I did was to install all the lamps, because I could only start the furnishing work in the house with the lights on. To make it a bit cooler, some lamps in the house are smart lighting, of which the brightness, color, and color temperature can be adjusted through a mobile app on the phone. Here comes the question, since lighting is one of the essential installments for the house, in addition to the current design of lighting, what more can we do to make the lighting even smarter?

1.1. BACKGROUND

LIGHTING accounts for 19% of electricity consumption worldwide, 13% in China, and 14% in the European Union [1, 2]. While the traditional incandescent lamps being phased out, Solid State Lighting (SSL) as the new generation of lighting technology, promises great potential for more advanced and smarter lighting. SSL is poised to play an essential role in improving efficiency and design, as well as creating innovations for the lighting industry. An SSL system is in principle a micro electronic optical system and thereby, can potentially tap into the huge device and technology portfolio of MEMS, IC packaging and similar micro system technologies. One of the key aspects is to combine lighting with additional functions for a variety of applications to enhance the design and create new business opportunities [3].

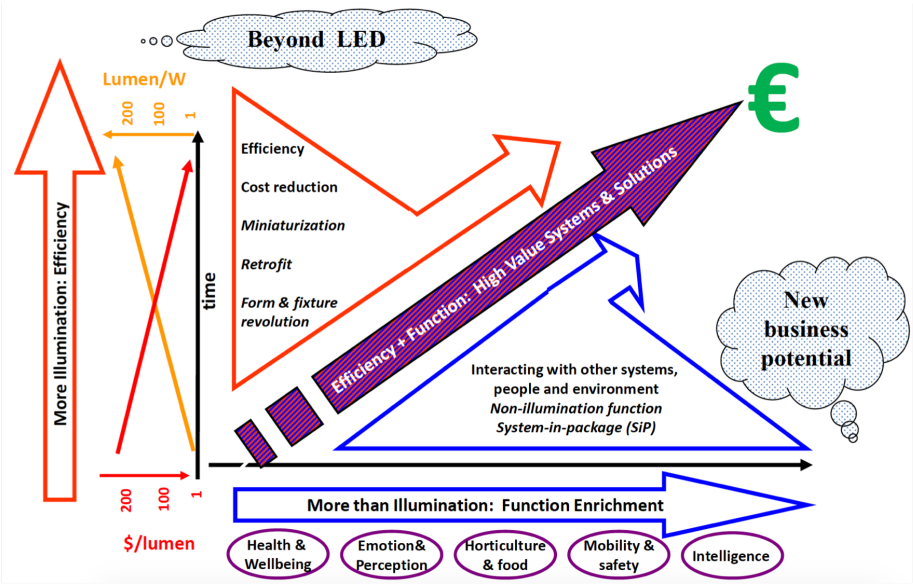

Figure 1.1: The new technology landscape of lighting: *More Illumination* & *More than Illumination*. *More Illumination* refers to improving the illumination efficiency, and *More than Illumination* refers to integrating non-illumination functions to the system [4].

The landscape of the lighting technology is depicted in Figure 1.1[4],with the two axes related to *More Illumination* and *More than Illumination* separately, where *More Il-*

lumination refers to improving the illumination efficiency, and *More than Illumination* refers to integrating non-illumination functions to the system. The development of illumination efficiency of SSL follows the Haitz's Law, which predicts that the illuminance per LED increases by a factor of 20 while the cost per lumen drops by a factor of 10 per decade [5]. Nevertheless, SSL is *More than Illumination*. SSL has been integrated with non-illumination system and functions in various scenarios, such as health wellbeing, emotion perception, etc., where the additional functions are in demand. Furthermore, with the booming of Internet of Things (IoT), lighting is the perfect conduit for the sensory network. As the ubiquitous utility in the building, lighting is throughout the whole building, integrating lighting with sensors makes each light point a node for the sensory network [6].

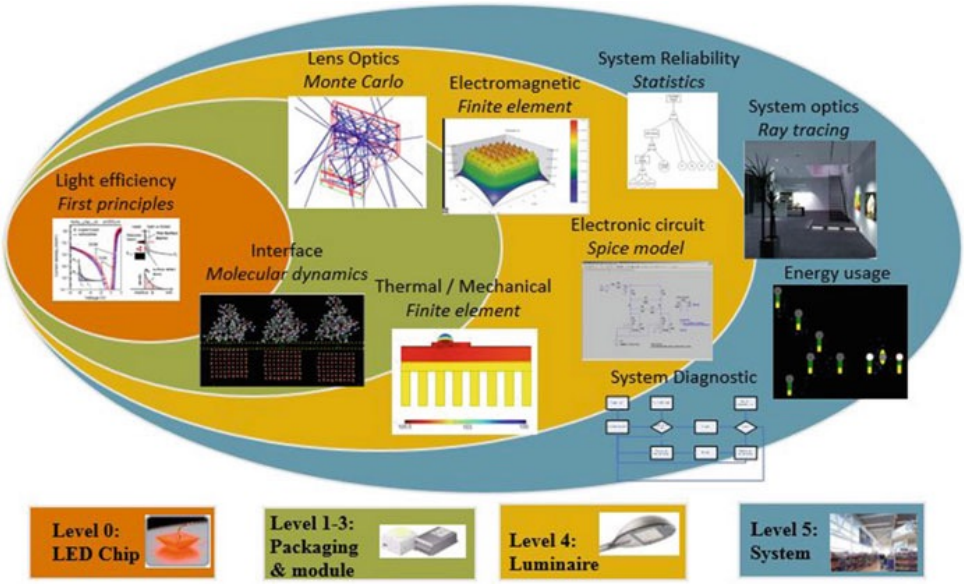

Figure 1.2: The prediction landscape of SSL products interpreted in different packaging levels [7].

An SSL system accounts for the integration of different components. In addition to the LED chips, more functions have been integrated in different packaging levels as shown in Figure 1.2 [7–9]. It can be the integration of a full collection of LED luminaires for an elaborate lighting system, such as dynamic lighting. It may also be in a lower level of packaging that integrates the light module with non-illumination components such as sensors and controls and, at an even lower level, the LED chip can be combined with optical components for pattern modulation.

1.1.1. DYNAMIC LIGHTING

Dynamic lighting is one of the most common functional lighting applications of SSL. Dynamic lighting adapts illumination to where it is needed, it is widely used for both commercial and consumer applications, such as stage lighting in art performance and

task lighting for office lighting and hospital [3, 10]. In stage lighting applications, diverse light effects, for instance, the adjustable beam shape, are required to meet the requirements of the performance [11]. In task lighting applications, uniform illumination with local task luminaries is achieved by adjusting the light intensity and beam shape. Studies have proved that task lighting improves study productivity [12].

One of the solutions to achieve the dynamic lighting is to shape the beam with a secondary lens driven mechanical motors. This type of tunable lens is generally bulky and not affordable, one lens can easily cost hundreds of euros [13]. Another solution is to use an array of LED lights, each of them controlled by programs to achieve the required lighting effect. The array of lamps bring up the cost while not all the lamps are not operated at their peak operating range [14].

1.1.2. LIGHTING EMBEDDED WITH AIR QUALITY DETECTOR

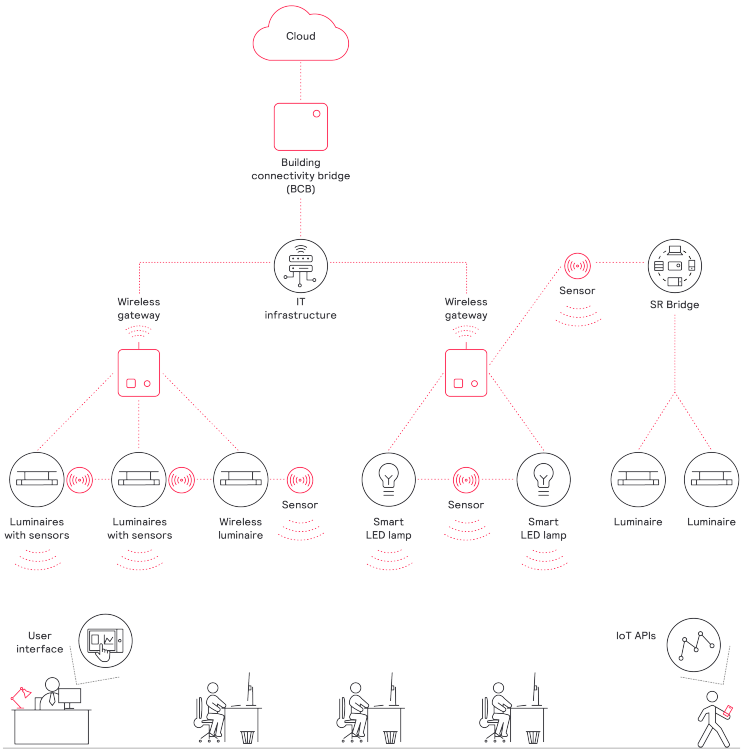

Figure 1.3: The Interactive IoT framework connecting the sensors in the luminaries from Philips [15].

The development of SSL technology has evolved the lighting infrastructure to serve *More than Illumination*. With the approaching of the 5G era, data flow is becoming much faster and at a lower cost [16], IoT is poised to become an integral part of our

economy and lifestyle [17]. IoT, which hosts a sensory network, connects various endpoints('things") and transmits data through the connection [18]. A Gartner report states that smart lighting is one of the most mature IoT aspects and closest to tech adoption [15]. In the lighting domain, the "things" refer to smart luminaires and sensors as the infrastructural elements. In the evolution of the IoT solutions, lighting products as a ubiquitous utility in the building is the perfect intermediate for equipping with sensors and adopting the current lighting system in the building into a data network [15]. With the help of sensors, the light sensory network can perform the sensing for different phenomena, while providing the illumination to the house [19].

Among all the scenarios to integrating SSL with sensors, the air quality detector has drawing lots of attention. Commercial air quality detectors requires particular installment in the rooms, which uses a standalone signal reception with either the switch or mobile phone. What's more, it costs at least hundreds of euros, which makes it expensive to build up a whole network in the building [20]. Within the light sensory network, a MEMS particulate matter (PM) sensor can be integrated into the light system to detect the air quality in the building without causing any extra manual work nor signal reception[21, 22].

1.1.3. INTEGRATION WITH OPTICAL COMPONENTS

The applications mentioned earlier are based on the higher packaging level of SSL products as depicted in Figure 1.2. In a lower packaging level, SSL also has the potential to integrate with different modules, for instance, to incorporate an optics to get pattern modulation of the light in a customized beam shape [23, 24]. The integration of micro optical components is of great significance for further miniaturization and performance improvement of the LED [25]. While the primary optics is a layer of translucent material fixed on the LED chip for the light emission and protects the LED die, the pattern modulator is dependent on the secondary lens. A customized micro optics helps to shape the beam to become homogenized or patterned [26, 27]. Moreover, a well-defined optical component can also help reduce the size of the LED packaging without sacrificing its performance[28, 29]. This can be helpful in applications such as surgical lighting where adaptive optics with adjustable optical performance becomes essential [30, 31].

1.2. OUTLINE OF THIS THESIS

The objective of this thesis is to investigate different solutions of combing MEMS technology with SSL for the concept of *More than Illumination*. From the perspective of different packaging levels of SSL, several distinct topics are explored to serve the purpose. The outline of the thesis is shortly summarized as follows.

Starting from the highest SSL packaging level, in chapter 2 we introduce a tunable optical system controlling the light distribution. The purpose of this work is to build up a tunable optical system for current commercially available LED lights to achieve dynamic lighting. The tunable optical design is based on a flexible actuator fabricated on a polyimide substrate. The actuation of the flexible actuator is based on the Lorentz force. The system can achieve efficient beam shape control by tuning the applied DC voltage. Parts of this chapter have been published in References [32, 33].

Chapter 3 is based on Reference [34], presents a sensor for air quality detection which can be integrated with the SSL products. The sensor chip observes the scatter light triggered by particles in a microchamber, which is formed by two silicon submounts with cavities and metal contacts.

While the previous chapters were focusing on the higher packaging level of SSL applications, in chapter 4, a micro size optical component to be mounted on the LED chip for the SSL applications was proposed. The demonstrated optics is a micro Fresnel lens, which uses micro-structured patterns to spatially modulate the intensity distribution of the light passing through, thereby has strict requirements on the opaque region for the light redistribution. The Fresnel lens is fabricated by encapsulating lithographically defined vertically aligned carbon nanotube (CNT) bundles inside a polydimethylsiloxane (PDMS) layer. The composite material of the lens combines the excellent optical absorption properties of CNT with the transparency and stretchability of PDMS. By stretching the elastomeric composite in the radial direction, the focal length of the lens can be tuned accordingly. This chapter is based on References [35], [36], both coauthored with Dr. Lei Wei. This work was also reported by the electronics industry magazine *EETimes* [37].

In chapter 5, we continued to explore the property of CNT/PDMS composite. With the same format of vertically aligned CNT infiltrated in PDMS as in the previous chapter, a new concept of flexible interposer utilizing the electric property of the composite is studied. The interposer is based on the PDMS as support material, while the embedded vertically aligned CNT bundles serve as conducting vias with its electrical conductivity. The composite combines the flexibility of the elastic material and the conductivity of the CNTs. Chapter 5 is based on Reference [38], a master thesis of Yingjie Shen who has contributed to this project.

Finally, in Chapter 6 conclusions and recommendations for future developments are presented.

REFERENCES

[1] National Development and Reform Commission, *The Deployment Of Solid State Lighting*, Tech. Rep. (2013).

[2] A. De Almeida, B. Santos, P. Bertoldi, and M. Quicheron, *Solid state lighting review - Potential and challenges in Europe,* Renewable and Sustainable Energy Reviews **34**, 30 (2014).

[3] European Commission, *Lighting the future - Accelerating the development of innovative lighting technologies*, Tech. Rep. (Brussels, 2011).

[4] G. Zhang, *Simply enhancing life with light - More than illumination*, Tech. Rep. (2010).

[5] Nature Photonics, *Haitz's law,* Nature Photonics **1**, 23 (2007).

[6] C. Papatsimpa, *Performance of intelligent lighting sensor networks : analysis, modeling and distributed architectures*, Ph.D. thesis, Technische Universiteit Eindhoven (2019).

[7] W. D. Van Driel and X. J. Fan, *Solid State Lighting Reliability: Components to Systems* (2013).

[8] G. Q. Zhang, H. van Zeijl, W. D. van Driel, R. Poelma, Z. K. Esfahani, M. R. Venkatesh, L. Middelburg, and B. El Mansouri, *Smart systems integration in the era of solid state lighting,* Smart Systems Integration 2017 - International Conference and Exhibition on Integration Issues of Miniaturized Systems, SSI 2017 , 159 (2017).

[9] W. Ling, *China's SSL Industrial Development*, Tech. Rep. (Sheffield, 2018).

[10] P. Liu, H. Wang, Y. Zhang, J. Shen, R. Wu, Z. Zheng, H. Li, and X. Liu, *Investigation of self-adaptive LED surgical lighting based on entropy contrast enhancing method,* Optics Communications (2014), 10.1016/j.optcom.2013.12.085.

[11] YajiangAppliedTechnologies, *Dynamic stage effecst in Shanghai international film festival,* (2013), accessed: 16-Jun-2019.

[12] H. Juslén, M. Wouters, and A. Tenner, *The influence of controllable task-lighting on productivity: a field study in a factory,* Applied Ergonomics **38**, 39 (2007).

[13] *Optotune Low Dispersion, VIS Coated, Electrically Focus Tunable Lens | EL-10-30-TC-VIS-12D,* Accessed: 31-Aug-2020.

[14] Y. Zhang, J. Tang, J. Wang, N. Liu, F. Wang, and D. Geng, *Adjustable beam lighting with LED matrix and lens array,* Journal of the Society for Information Display **25**, 496 (2017).

[15] Interact, *How smart lighting is leading the way in IoT adoption,* Accessed: 30-Aug-2020.

[16] Huawei, *5G for IoT and Mobile*, Tech. Rep. (Huawei, 2016).

[17] KPMG, *Converging 5G and IoT : a faster path to smart manufacturing*, Tech. Rep. (KPMG, 2019).

[18] P. Collela, *5G and IoT: Ushering in a new era,* (2019), accessed: 22-Nov-2019.

[19] H. Martin, *6 ways lighting can be used for more than illumination,* Accessed: 18-Jan-2016.

[20] Xiaomi, *Xiaomi PM2.5 Detector,* (2018), accessed: 22-Nov-2019.

[21] J. Higuera, A. Llenas, and J. Carreras, *Trends in smart lighting for the Internet of Things,* arXiv e-prints **aug** (2018), arXiv:1809.00986 .

[22] F. V. Tuijl and B. Pronk, *LpR*, Tech. Rep. 67 (2018).

[23] J. W. Pan, S. H. Tu, W. S. Sun, C. M. Wang, and J. Y. Chang, *Integration of Non-Lambertian LED and Reflective Optical Element as Efficient Street Lamp,* Optics Express **18**, A221 (2010).

[24] J. C. Miñano, P. Benítez, R. Mohedano, and R. Alvarez, *Newer optics efficiently mix, dim, and color-tune LED light,* SPIE Newsroom , 2 (2013).

[25] Z. K. Esfahani, *Monolithic 3D Wafer Level Integration: Applied for Smart LED Wafer Level Packaging,* Ph.D. thesis, Delft University of Technology (2017).

[26] H. P. Herzig, *Micro-Optics: Elements, Systems And Applications* (Taylor & Francis, 1997).

[27] P. Schreiber, S. Kudaev, P. Dannberg, and U. D. Zeitner, *Homogeneous LED-illumination using microlens arrays,* Nonimaging Optics and Efficient Illumination Systems II **5942**, 59420K (2005).

[28] *LED Lighting Requires New Approaches in Optics,* (2018), accessed: 30-Aug-2020.

[29] J.-W. Pan, C.-M. Wang, H.-C. Lan, W.-S. Sun, and J.-Y. Chang, *Homogenized LED-illumination using microlens arrays for a pocket-sized projector,* Optics Express **15**, 10483 (2007).

[30] T. Liu, M. Rajadhyaksha, and D. L. Dickensheets, *MEMS-in-the-lens architecture for a miniature high-NA laser scanning microscope,* Light: Science and Applications **8** (2019), 10.1038/s41377-019-0167-5.

[31] R. RUBIO, J. SANTANDER, L. FONSECA, N. SABATE, I. GRACIA, C. CANE, S. UDINA, and S. MARCO, *Non-selective NDIR array for gas detection,* Sensors and Actuators B: Chemical **127**, 69 (2007).

[32] X. LI, J. Wei, T. Ma, C. Yuan, L. Sarro, and K. Zhang, *Compact tunable optics for dynamic lighting,* in *Classical Optics 2014*, Vol. 1 (OSA, Washington, D.C., 2014) p. JTu5A.35.

[33] Teng Ma, Xueming Li, Jia Wei, G. Zhang, and P. Sarro, *Numerical modeling of flexible actuator for dynamic lighting,* in *2014 15th International Conference on Thermal, Mechanical and Mulit-Physics Simulation and Experiments in Microelectronics and Microsystems (EuroSimE)* (IEEE, 2014) pp. 1–4.

[34] X. Li, E. Iervolino, F. Santagata, J. Wei, C. A. Yuan, P. Sarro, and G. Zhang, *Miniaturized particulate matter sensor for portable air quality monitoring devices,* in *IEEE SENSORS 2014 Proceedings* (IEEE, 2014) pp. 2151–2154.

[35] X. Li, L. Wei, R. H. Poelma, S. Vollebregt, J. Wei, H. P. Urbach, P. M. Sarro, and G. Q. Zhang, *Stretchable Binary Fresnel Lens for Focus Tuning,* Scientific Reports **6**, 25348 (2016).

[36] X. Li, L. Wei, S. Vollebregt, R. Poelma, Y. Shen, J. Wei, P. Urbach, P. Sarro, and G. Zhang, *Tunable binary Fresnel lens based on stretchable PDMS/CNT composite,* in *2015 Transducers - 2015 18th International Conference on Solid-State Sensors, Actuators and Microsystems (TRANSDUCERS)* (IEEE, 2015) pp. 2041–2044.

[37] J. Happich, *Stretchable Polymer Optics Embed Carbon Nanotubes for Better Focus,* (2016), accessed: 23-Feb-2020.

[38] Y. Shen, *Flexible Interposer Based on Carbon Nanotubes and PDMS Composite,* (2015).

2

TUNABLE OPTICS FOR DYNAMIC LIGHTING APPLICATION

Parts of this chapter have been published in Classical Optics 2014 **JTu5A.35**, [1], and EuroSimE **2014**[2].

In this chapter, we demonstrated a tunable optical system for beam shaping, which can be used in dynamic lighting applications. The system is made for controlling the light distribution, specifically for controlling the beam angle of the lighting. Driven by a flexible actuator which generates large actuating force, the system can achieve beam angle control by tuning the applied DC input. The actuator with a copper coil on a polyimide substrate was fabricated using a standard fabrication process of a flexible printed circuit board (PCB), which makes it compatible with mass production.

2.1. INTRODUCTION

THANKS to the cutting edge of research, SSL shows the high potential to combine lighting with new functions and new applications, which makes lighting become much more than illumination [3], [4]. One of the applications benefiting from the SSL development is dynamic lighting. Dynamic lighting works by adapting illumination to where it is needed. It is widely used for both business and consumer applications, such as stage lighting in the art show and task ambient lighting for the office. In such applications, an adjustable beam shape is essential for the light effect [5]. Commercial stage light products use motors to tune the optics mounted on the lamp for precise visual effect [6], however, the generally large motors makes the whole system bulky. Current task ambient lighting illuminates the area of interest by switching on or off a matrix of individual lamps [7], however, this requires many lamps to be integrated without being fully used in most scenarios, which in turn brings up the system costs.

The objective of this work is to build up a solution to achieve an adjustable beam angle for a packaged LED by focusing on the secondary optics design. By combining SSL with MEMS technology, it is possible to integrate additional functionality to lighting products without significantly increasing the size of the system. A large number of existing studies have examined the use of aluminum mirrors to steer the light beam[8][9]. The tilted mirror has been proved to be able to reach large focal change for the beam under precise control, however, this reflective method requires that the modulator is mounted on the light source with an initial angle which brings challenges to integrate the light source with the mirrors. Alternatively, a lens based on liquid filled elastomer shells were used to create a dual mode meniscus lens, by tuning the pressure of the micro chamber[10], [11]. However, it has the drawback of shape instability and temperature sensitivity, thereby in this work a lens with a supported actuator is more preferable because it can be directly mounted on the light source directly without tidal coupling, while the lens itself has steady optical property.

In order to drive the optics on a packaged LED, which generally measures 1.5 mm in diameter, a large force and displacement actuator is required. Electrostatic and electrothermal actuators have the advantages of simplicity and straightforward fabrication, however the actuation force and displacement cannot meet the requirement to drive a lens with a displacement range of several millimeters. While both piezoelectric and shape memory alloy actuation provide large force and displacement, they have a complicated material preparation which makes the fabrication difficult and limits the reliability [12, 13]. Magnetic actuation method has the advantages of its large force and displacement and is employed as the actuation method in this work [14–19].

A magnetic actuator consists of a magnetic flux source, coil, and support layer for

the actuated object. Ring shape magnets are being used for magnetic bearings and coupling due to its magnetic flux density distribution and is employed in this work for the levitation of the optics [20, 21]. Recent work on adopting the flexible PCB in MEMS application [22, 23] has shown that flexible PCB-MEMS combines the flexible PCB and MEMS devices in an appealing method. The flexible PCB assembles electronic components on the polymeric substrate, such as polyimide, with the polyimide layer functioning as both support layer for the sensors and actuator for their movement.

To integrate a large displacement actuator in a tunable optical system, a flexible PCB can be used to integrate the optics and actuator. The tunable optical system proposed in this work combines the electromagnetic actuation and flexible PCB fabrication. A copper coil was fabricated on the flexible PCB substrate. With the help of a permanent external magnet, when applied with a DC input, the Lorentz force on the coil drives the optics on the coil vertically, which in turn controls the beam shape.

2.2. DESIGN PRINCIPLE

2.2.1. OPTICS: BASIC PRINCIPLES

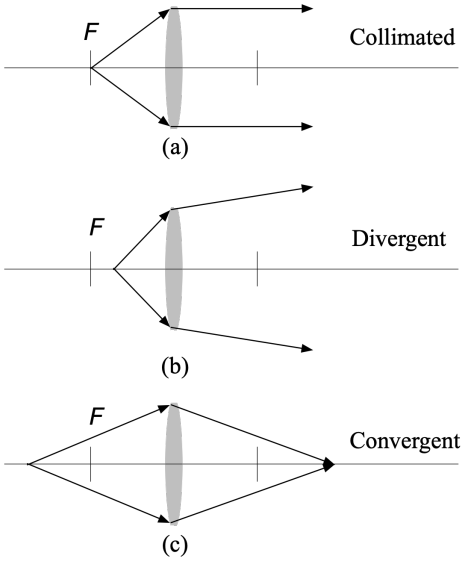

Figure 2.1: Ray trace for biconvex lens at different positions from the focal point. a) light is collimated when the light source is placed at focal point; b) light is divergent when the light source within focal point; c) light is convergent when light source is located further than focal point.

In non-imaging optics theory, when light propagates through a convex lens, the outgoing angle is dependent on the position of the lens to the light source[24, 25]. As shown in Figure 2.1, different beam angle of the light source can be obtained by placing the convex lens at different positions. When the lens is placed at the focal point of the lens, the outgoing light is collimated by the lens, as in Figure 2.1a; by placing the lens within

the focal point from the light source, as in Figure 2.1b, the outgoing light is diverging. When increasing the distance of the optics from the light source, the divergent beam becomes more collimated due to the optics, and the light will become convergent, as in Figure 2.1c [26]. This principle is also widely used in optical collimation and focusing. In this way, the light distribution beyond the lens can be controlled by tuning the position of the optics.

2.2.2. OVERVIEW OF THE OPTICAL SYSTEM

The proposed optical system is depicted in Figure 2.2. The system consists of a light source, a ring shape magnet, an active actuator, and an optics. The light source is a LED. A permanent magnet with ring shape was chosen due to its magnetic flux density distribution, which will be discussed in the following session. The active actuator is a copper coil fabricated on patterned flexible polyimide substrate (indicated by the dark red circuits). The vertical movement of the optics then changes the distance between the light source and the biconvex lens, thus controls the beam shape of the light emitted from the LED, as indicated by the shift of angle α from Figure 2.2 a to Figure 2.2b.

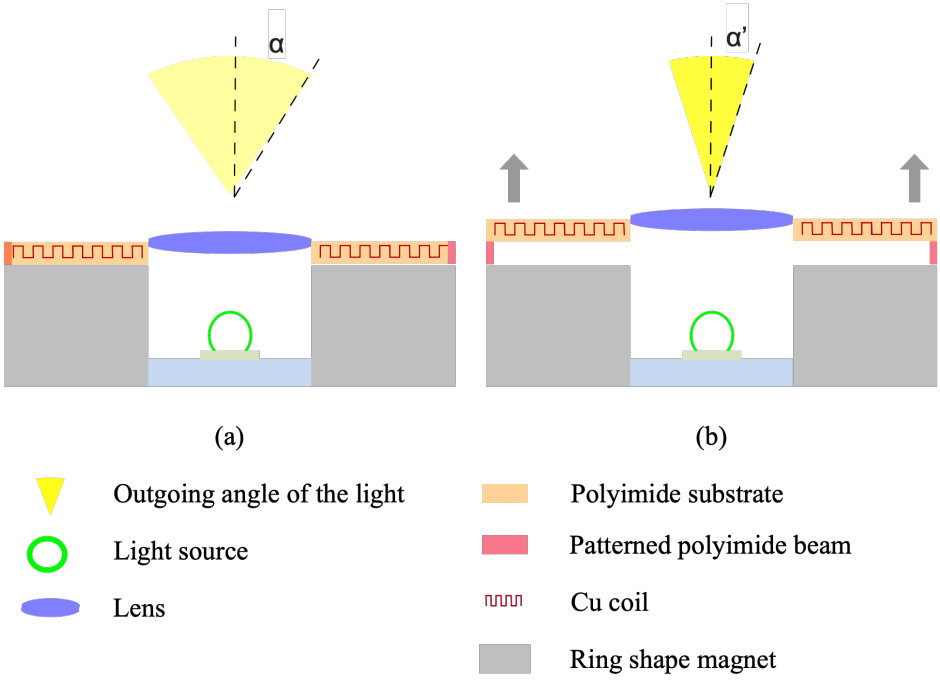

Figure 2.2: The schematic view of the optical system. LED is placed in the center of the ring shape magnets as light source. The magnetic field distribution generated by the magnets will apply a Lorentz force on the coil and changes the distance between the lens on the coil and the light source, thus controls the outgoing angle of the light.

2.2.3. MAGNETIC ACTUATOR

To assess the actuation mechanism, a simulation was carried out with COMSOL Multiphysics 4.3. A 2D axisymmetric magnetic field application model was used due to the symmetry of the system. The model consists of three parts: a ring shape magnet with a hole in the middle, copper coils, and the surrounding air space which was large enough to avoid boundary effects. The detailed parameters of the simulation can be found in Table 2.1.

The electromagnetic AC/DC module in COMSOL is used in the calculation. The magnetic potential, current density and Lorentz force can be expressed as:

$$F = J_e \times B \tag{2.1}$$

Where J_e is the current density and B is the magnetic flux density. The Lorentz force F is dependent on the current density J_e and magnetic flux density B. The permanent magnet has a constant distribution of magnetic flux, thus the Lorentz force F is dependent on the current applied on the coil.

Parameter description	**value**	**units**
Magnetization of magnet	900	KA/m
Coil conductivity	60	MS/m
Air permittivity	1	na
Applied current density J_0	0.112	GA/m^2
Magnet outer radius	9.775	mm
Magnet height	8	mm
Magnet inner radius	2.275	mm
Coil width	50	μm
Coil height	25	μm
Coil spacing	50	μm
Number of coils	24	na
Length of a segment coil	8.2	mm

Table 2.1: Geometric and technical parameters of the magnet and coils used in the COMSOL simulation

The ring shape permanent magnet was employed for the magnetic actuator due to its magnetic field distribution. Figure 2.3 shows the magnetic field distribution around the magnet. As shown in Figure 2.3a, the magnetic flux on top of the magnet is circulating around the edge, reflected by the arrows in the cross-section view. The magnetic flux B is composed of vertical component and horizontal component, thus the generated Lorentz force is also composed of vertical component and horizontal component, among which the horizontal components are cancelled out due to the symmetry of both the magnets and coil, as shown in Figure 2.3b. Hence only the vertical part of the Lorentz force is effective.

The Lorentz force exerted on the coil depends linearly on the magnetic flux density. Figure 2.4a shows the vertical Lorentz force density distribution along the radial direction for different locations above the magnet exerted on a single wire cross section with constant current density J_0. The Lorentz force density starts to increase at r= 2.275 mm

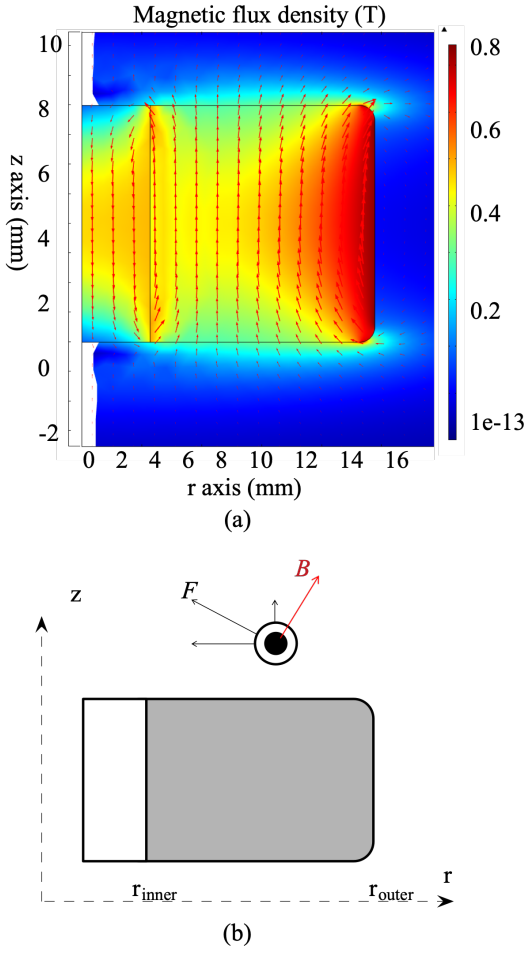

Figure 2.3: (a) Cross section view of the Magnetic flux density distribution of the ring shape magnet; (b) Schematic view of the magnetic flux density distribution above the magnet, the vertical component of the generated Lorentz force can be used to drive the optics, while the lateral components are canceled due to the symmetry of the magnetic field distribution.

which is the inner radius of the magnet, and reaches its peak at 9.775 mm, the outer radius of the magnet where it has the strongest lateral component of the magnetic flux density as indicated by the distribution in Figure 2.3a. Within the inner radius, the Lorentz force is negative especially when the coil is placed at as close as 1 mm to the magnet. This is due to that the lateral component of the magnetic flux is opposite in this area. However, this can be avoided in this case because the area within the inner radius is reserved for the optics and the coil will not be placed in this area.

Figure 2.4b shows that the generated Lorentz force decreases vertically as the magnetic flux density attenuates. The Lorentz force density has the maximum value at the

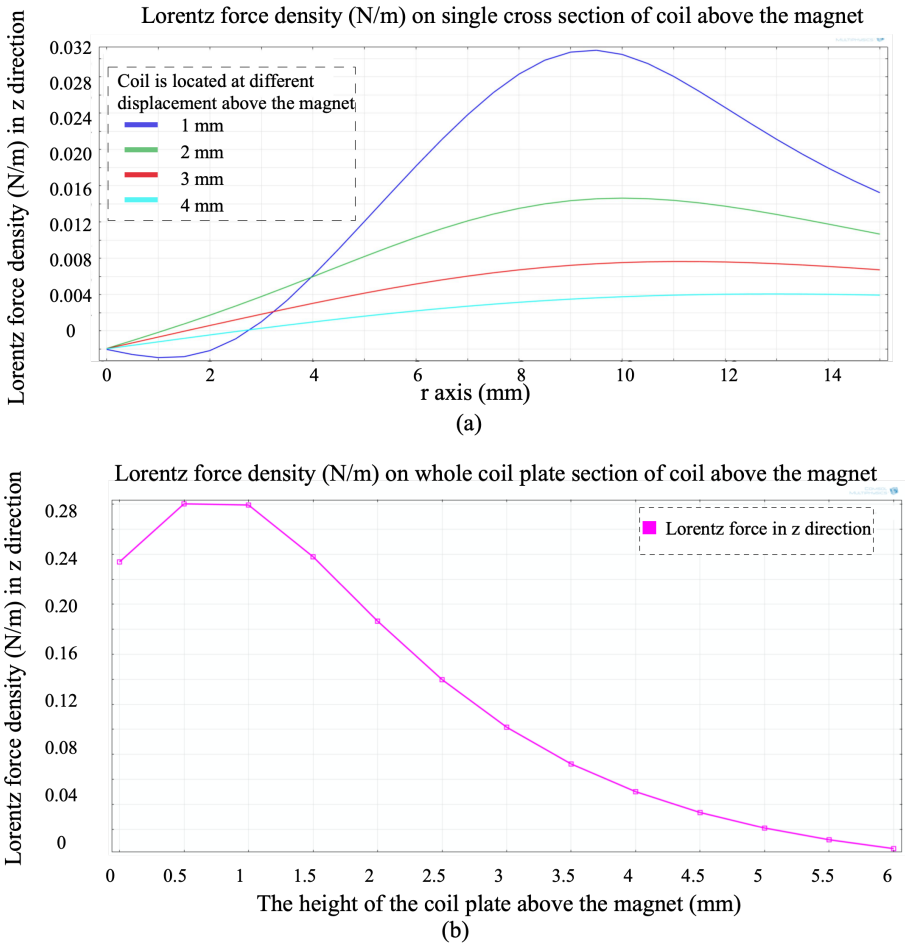

Figure 2.4: (a) Single wire cross-section plot of Lorentz force density F_z along r axis (lateral direction) for different heights above the magnet from the simulation, (b) vertical Lorentz force density F_z along z axis exerted on the whole coil plate when the windings are located at different positions above the ring shape magnet.

range from 0.5 mm to 1 mm above the magnet and decays exponentially along the z direction. This is because the distribution of the magnetic field attenuated as the coils are driven away from the magnet [2]. At the 0 mm above the magnet, the lateral component of the magnetic field is very small, while most of the magnetic flux is composed of the vertical component. As the position moves up, the lateral component of the magnetic field becomes greater and thus the Lorentz force increases. After it reaches its peak, the intensity of the magnetic field drops, which in turn leads to smaller Lorentz force density.

The generated Lorentz force on the optics is counter-balanced by the gravity of the optics on the substrate and elastic restoring force of the polyimide beams. This non-

linear relationship can be used to analyze the height of magnet and vertical Lorentz force density during design. The equations that describes the relationship between the vertical Lorentz force and the gravity force of tunable optics system are shown below:

$$F_Z = G_{total} \pm F_{sprint} \tag{2.2}$$

$$G_{total} = (m_{lens} + m_{beams} + m_{substrate}) * g \tag{2.3}$$

where m_{lens}, m_{beams} and $m_{substrate}$ are the mass of optics, beam and substrate respectively, g is the gravitional constant, and F_{sprint} is the force provided by the four beams.

2.2.4. OPTICAL SIMULATION

A corresponding ray tracing simulation of the light intensity distribution change is made using TracePro. The simulation discusses the light intensity distribution when a biconvex lens is located at two different positions. The light source has a beam angle of 25°, while the biconvex lens is 5 mm in diameter and focal point of 4.9 mm. When the lens is at 2 mm away from the light source, the light is mostly distributed at an angle of 20°, as the optics move to 4 mm away from the light source, the beam angle is tuned to 15°, as shown in the Candela plot in Figure 2.5(a,b) separately. The corresponding irradiance maps in Figure 2.5(c,d) show that besides the beam angle change, the peak incident flux jumped to 4431.6 W/m^2 from 14354 W/m^2, meaning that more rays passed through the lens with the smaller incident angle but with stronger intensity.

2.3. RESULTS

2.3.1. FABRICATION: PROOF OF CONCEPT

An LED of only 3 mm in diameter and an outgoing angle of 25° was used as the light source. A biconvex lens of 5 mm in diameter, 2.3 mm in thickness and 25 mg in weight was employed to tune the light for the proof of concept.

A schematic view of the device is shown in Figure 2.6(a). With the ring shape permanent magnet functioning as the magnetic source, the copper coils on patterned polyimide substrate are mounted on the top of the magnet, with holders fixing the pads for the wiring. The cube shape holder is installed with the magnet and coil on a polyimide substrate. The four beams around were patterned directly on the polyimide thus support and drive the coil with Lorentz force. All pillars and molds are fabricated using 3D printing. The fabricated Cu coil on the polyimide substrate is shown in Figure 2.6(b).

As shown in Figure 2.7, two layers of copper coil were fabricated with precise through hole connection alignment, each layer is isolated with polyimide. The layers of Cu coil can be added up to multiple layers when necessary. This can be of great significance when a higher Lorentz force is needed for the actuator. Through holes were then made to connect both sides of the coil and connected with the wiring pads for the voltage input.

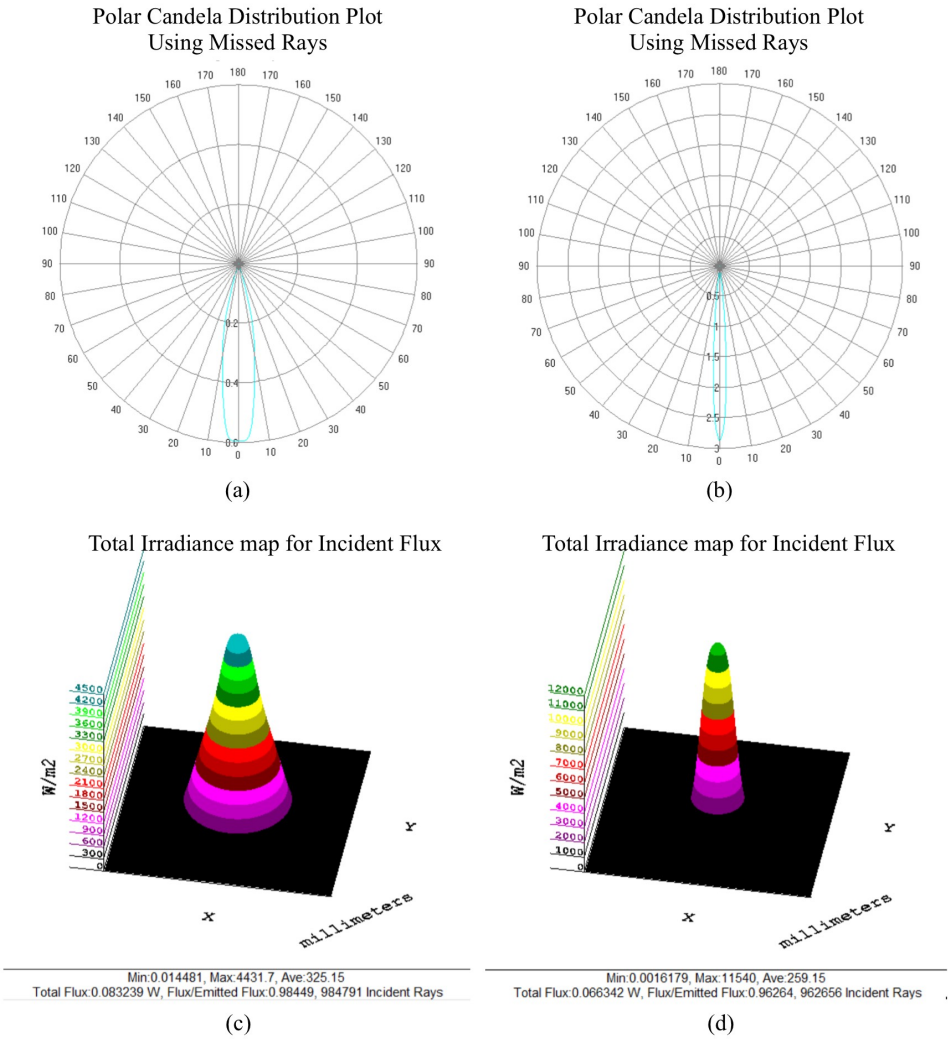

Figure 2.5: Light distribution changes with the position of the biconvex lens above the light source. (a, b) The polar Candela distribution plots when the optics is 0 mm and 4 mm away from the light source, leading to the beam angle shift from 20° to 15° separately; (c, d) The corresponding total irradiance map for incident flux for each situation, the peak incident flux increased from 14354 W/m^2 to 4431.6 W/m^2.

2.3.2. TEST SETUP

A function generator was used to provide the DC input for the coils to control the position of the optics, and two pieces of 1.5 V batteries were driving the LED lamp. A reception plate was located 50 cm away above the LED lamp to measure the spot size to visualize the effect of the moving optics. The movement of the optics, caused by different DC inputs, will lead to a change of the spot size projected on the reception board.

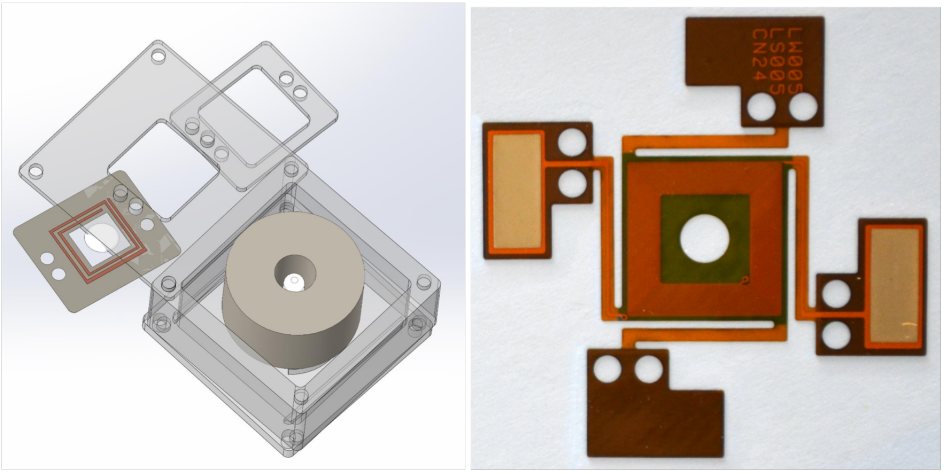

Figure 2.6: (a) A schematic view of the whole system, ring shape permanent magnet is installed in a 3D printed holder, while the cover is mounted with the flexible actuator, (b) the fabricated device, with Cu coil on patterned polyimide substrate.

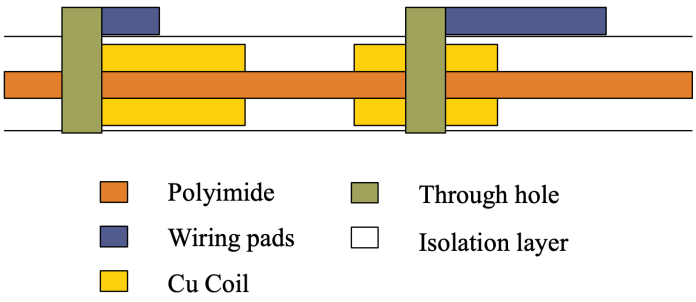

Figure 2.7: Layout of the coil fabrication. Cu coils were coated and patterned on the polyimide substrate, followed by isolation layer to isolate the Cu layer from directly exposure to the air. Through holes were then made to connect both sides of the coil and connected them with the wiring pads for the voltage input.

The test was performed in a dark room to avoid any noise. The light illuminated from the device at different conditions was recorded by a white reception plate. The light spots projected on the plate were then recorded by a camera with consistent exposure parameters for comparison.

The difference of light distribution can be easily distinguished as shown in Figure 2.8, a reception plate was used to visually demonstrate the spot size changes. Figure 2.8a shows the setup when the current input is set to be 0, while in Figure 2.8b, 5 V DC was applied on the coils, and the lens is driven up by the flexible actuator.

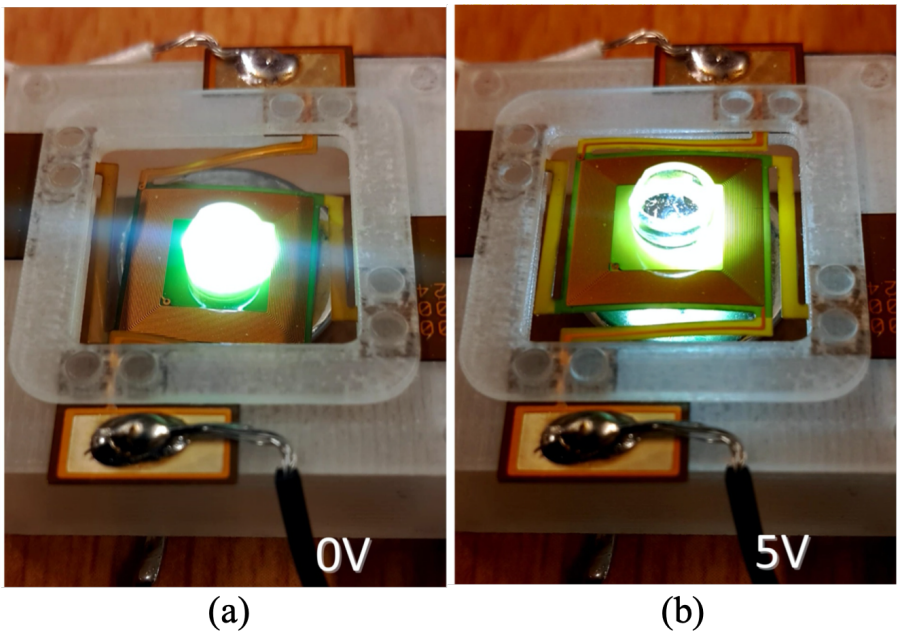

Figure 2.8: Set up for testing the light distribution change (a) The default situation when without any input; (b) The lens is driven up by the flexible actuator when applied with 5 V.

2.3.3. TUNING THE LIGHT

Different spot sizes were captured by changing the applied DC input on the actuator. As shown in Figure 2.9, without applied voltage, the measured spotsize on the reception plate is 15 cm in diameter. When applying with voltage from 1 V to 5 V in 5 steps, the diameter of the spot size changes from 15 cm to 12.95 cm, 12.24 cm, 11.29 cm, 10.5 cm, and 10.18 cm separately. As the spot size became smaller, the intensity of the spots is observed to become stronger, reflected by the brighter spots captured in the pictures.

The change of the spot size is not linearly dependent on the input DC, due to the fact that the flexible actuator has tensile stress which becomes stronger when the displacement of the optics increases and attenuated magnetic flux density which leads to weakened Lorentz force. The Large spot size provides a wider lighting area, with blurred light, while the small spot size provides more a focused lighting area, with high intensity.

In order to accurately evaluate the optical performance of the system, a measurement of the near-field luminance distribution was made to compare the irradiance map for the light source when applying DC input of 0 V and 5 V separately [27].

Irradiance flux data were obtained using near field interferometer. As shown in Figure 2.10, without any DC input, the irradiance map collected by the interferometer shows a big spot size, with around 20 mm in diameter, and incident flux maximum of 372.66 W/m^2. The corresponding rectangular Candela distribution plot on the bottom picture

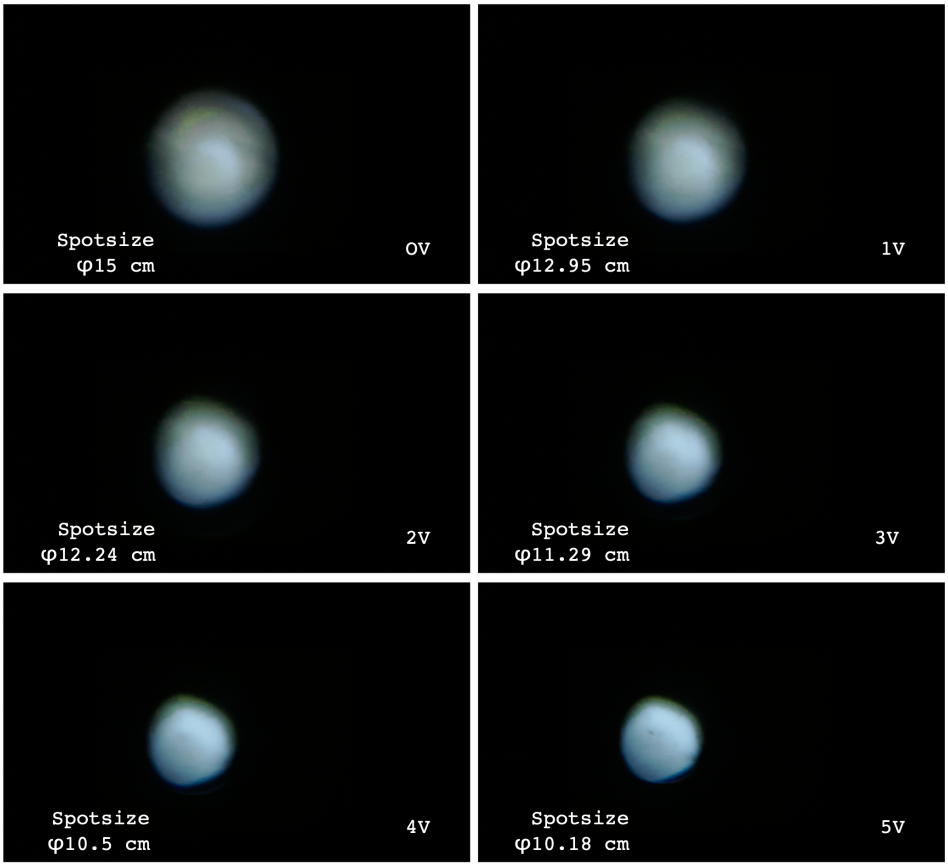

Figure 2.9: Spot size changes with applied voltage on the actuator. By applying DC input from 0 V to 5 V, the spot size shrinks from 15 cm in diameter to 12.95 cm, 12.24 cm, 11.29 cm, 10.5 cm, and 10.18 cm separately, while the intensity of the brightness is getting much stronger.

shows that a beam angle of 22.0° was detected. This beam angle is slightly smaller than 25°, the original beam angle of the light source, due to that there are already space between the optics and the light source at 0 V thus the beam is already slightly converged.

The same setup of near field interferometer has been applied on the system when applying with 5 V DC input. As shown in Figure 2.11, without the DC input, the irradiance map collected by the interferometer shows a much smaller spot size, with around 10 mm in diameter, which is only half size as before. The incident flux maximum increased to 1658 W/m^2. The corresponding rectangular Candela distribution plot on the bottom picture shows that a light source of 16.2° was detected. The outgoing angle of the system when applied with 5 V DC input has been adjusted to much smaller than its original outgoing angle. The results also match well with the simulation discussed in Figure 2.5 which indicates a change from 20° to 15° for the beam angle change.

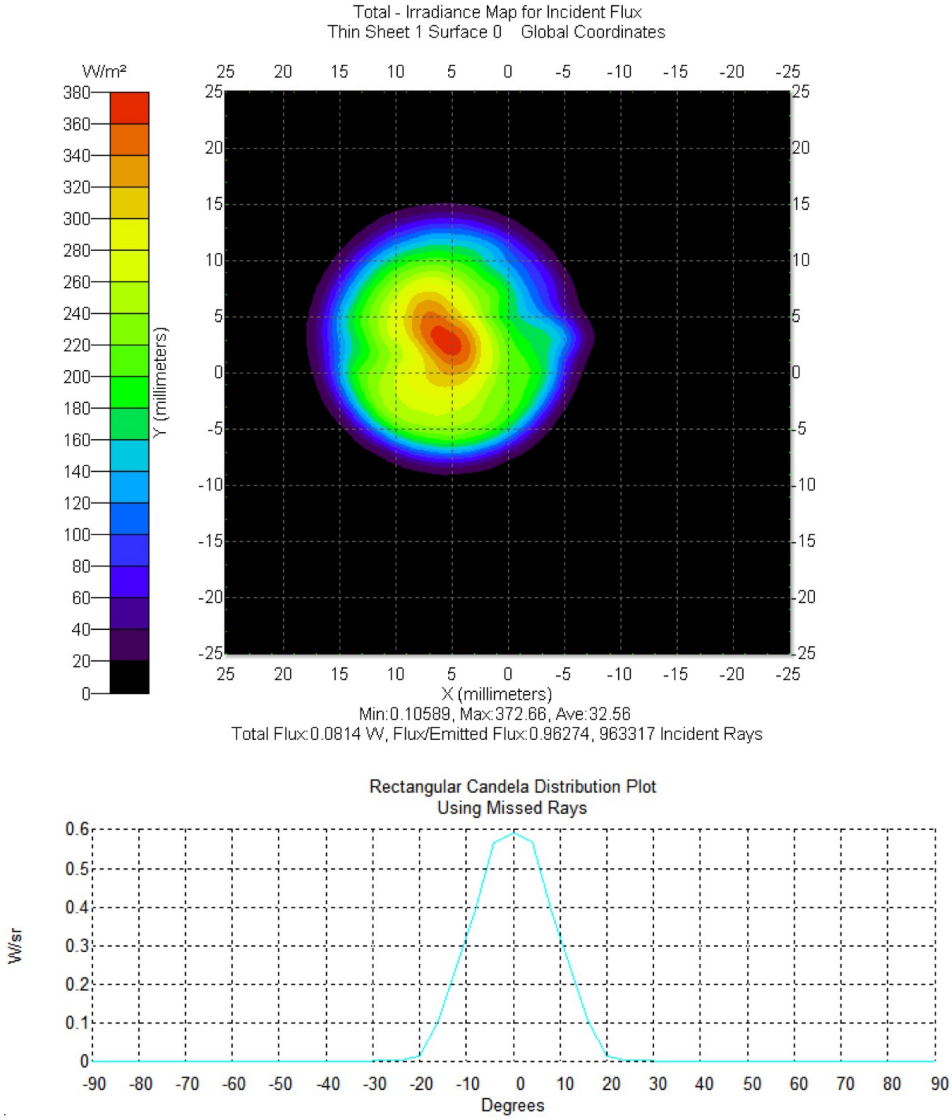

Figure 2.10: Irradiance flux data were obtained using near field interferometer. Without DC input, the irradiance map shows a big spot with maximum of 372.66 W/m^2. The corresponding Rectangular Candela distribution Plot indicates that the light source has outgoing angle of 22.0°.

2.4. CONCLUSION

A compact tunable optical system for dynamic lighting application was demonstrated in this chapter. Light distribution can be manipulated by applying an appropriate DC input to control the distance of the optics from the light source.

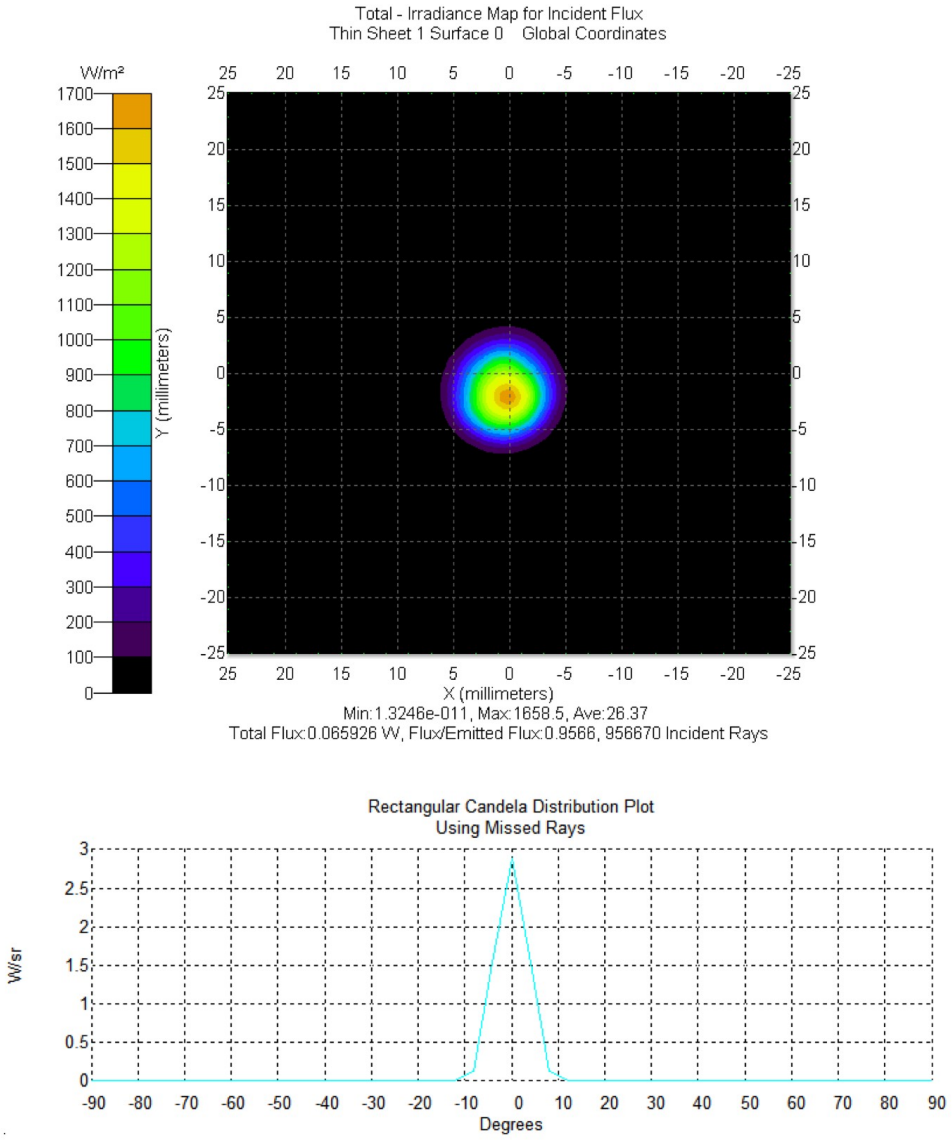

Figure 2.11: Irradiance flux data were obtained using near field interferometer when applied with 5 V DC input. The irradiance map shows a big spot with much higher maximum of 1658 W/m^2. The corresponding Rectangular Candela distribution Plot indicates that the light source has a beam angle of 16.2°.

The flexible actuator was fabricated using commercially available flexible PCB fabrication, suitable for mass production of the actuator, which is also suitable for the integration and packaging with LED. In this work we used two layers of coils stacked to drive the lens with significant displacement. However, if a larger Lorentz force is required, for

example to drive a larger lens, the straightforward fabrication method allows it to stack more than two layers of coils.

In some applications with more strict requirements on the compact size, the magnet in this system can be replaced with another coil design as the source of magnetic field. With one of the coils fixed, by applying opposite DC input, the other coil plate can be driven in the same way as with a permanent magnet.

The tunable optical system utilized a feasible solution without adding bulky motors or extra light sources to compensate for the required outgoing angle thus provides more freedom for the lighting designs. This system provides a new way to tune the light distribution with a compact size, a matured fabrication, and easy handling, promising a big potential in dynamic lighting applications.

REFERENCES

[1] X. LI, J. Wei, T. Ma, C. Yuan, L. Sarro, and K. Zhang, *Compact tunable optics for dynamic lighting*, in *Classical Optics 2014*, Vol. 1 (OSA, Washington, D.C., 2014) p. JTu5A.35.

[2] Teng Ma, Xueming Li, Jia Wei, G. Zhang, and P. Sarro, *Numerical modeling of flexible actuator for dynamic lighting*, in *2014 15th International Conference on Thermal, Mechanical and Mulit-Physics Simulation and Experiments in Microelectronics and Microsystems (EuroSimE)* (IEEE, 2014) pp. 1–4.

[3] G. Zhang, *Simply enhancing life with light - More than illumination*, Tech. Rep. (2010).

[4] European Commission, *Lighting the future - Accelerating the development of innovative lighting technologies*, Tech. Rep. (Brussels, 2011).

[5] LePower, *Task ambient lighting providing efficient and smart illumination to a room,* (2019), accessed: 16-Jun-2019.

[6] YajiangAppliedTechnologies, *Dynamic stage effecst in Shanghai international film festival,* (2013), accessed: 16-Jun-2019.

[7] Y. Zhang, J. Tang, J. Wang, N. Liu, F. Wang, and D. Geng, *Adjustable beam lighting with LED matrix and lens array,* Journal of the Society for Information Display **25**, 496 (2017).

[8] U. Hofmann, T. Wantoch, G. Eberhardt, I. Kinski, M. Moeser, F. Senger, C. Mallas, F. Isit, D. Itzehoe, L. D. T. Laser, and D. Technology, *Dynamic shaping of the basic intensity profile of adaptive laser headlights based on resonant MEMS scanning mirrors,* Vision , 1 (2016).

[9] C. Pollock, J. Morrison, M. Imboden, T. D. Little, and D. Bishop, *Beam shaping with tip-tilt varifocal mirror for indoor optical wireless communication,* Optics Express **25**, 20274 (2017).

[10] K. Mishra, C. Murade, B. Carreel, I. Roghair, J. M. Oh, G. Manukyan, D. Van Den Ende, and F. Mugele, *Optofluidic lens with tunable focal length and asphericity,* Scientific Reports **4**, 1 (2014).

[11] H. B. Yu, G. Y. Zhou, F. K. Chau, F. W. Lee, S. H. Wang, and H. M. Leung, *A liquid-filled tunable double-focus microlens,* **17**, 2370 (2009).

[12] Z. Qiu, J. S. Pulskamp, X. Lin, C. H. Rhee, T. Wang, R. G. Polcawich, and K. Oldham, *Large displacement vertical translational actuator based on piezoelectric thin films,* Journal of Micromechanics and Microengineering **20** (2010), 10.1088/0960-1317/20/7/075016.

[13] B. Holschuh and D. Newman, *Low spring index, large displacement Shape Memory Alloy (SMA) coil actuators for use in macro- and micro-systems,* Reliability, Packaging, Testing, and Characterization of MOEMS/MEMS, Nanodevices, and Nanomaterials XIII **8975**, 897505 (2014).

[14] D. J. Bell, T. J. Lu, N. a. Fleck, and S. M. Spearing, *MEMS actuators and sensors: observations on their performance and selection for purpose,* Journal of Micromechanics and Microengineering **15**, S153 (2005).

[15] Y. Q. Fu, J. K. Luo, M. Hu, H. J. Du, a. J. Flewitt, and W. I. Milne, *Micromirror structure actuated by TiNi shape memory thin films,* Journal of Micromechanics and Microengineering **15**, 1872 (2005).

[16] G. Vdovin and M. Loktev, *Deformable mirror with thermal actuators.* Optics letters **27**, 677 (2002).

[17] K. H. Koh, T. Kobayashi, and C. Lee, *A 2-D MEMS scanning mirror based on dynamic mixed mode excitation of a piezoelectric PZT thin film S-shaped actuator,* Optics Express **19**, 95 (2011).

[18] D. Niarchos, *Magnetic MEMS: key issues and some applications,* Sensors and Actuators A: Physical **106**, 255 (2003).

[19] P. Zheng, *Magnetic MEMS and Its Applications*, Ph.D. thesis, Florida State University (2004).

[20] B. Delinchant, F. Wurtz, J. P. Yonnet, and J. L. Coulomb, *Interaction between ring-shaped permanent magnets with symbolic gradients: Application to magnetic bearing system optimization,* IEEE Transactions on Magnetics **47**, 1418 (2011).

[21] T. Azukizawa, S. Yamamoto, and N. Matsuo, *Feasibility study of a passive magnetic bearing using the ring shaped permanent magnets,* IEEE Transactions on Magnetics **44**, 4277 (2008).

[22] A. Petropoulos, D. N. Pagonis, and G. Kaltsas, *Flexible PCB-MEMS flow sensor,* Procedia Engineering **47**, 236 (2012).

[23] S. Tung, S. R. Witherspoon, L. A. Roe, A. Silano, D. P. Maynard, and N. Ferraro, *A MEMS-based flexible sensor and actuator system for space inflatable structures,* Smart Materials and Structures **10**, 1230 (2001).

[24] H. Zappe, *Fundamentals of Micro-Optics* (Cambridge University Press, 2010) p. 646.

[25] M. Félix, C. Anguiano, A. Medel, D. Salazar, and H. Márquez, *Optimization of the optical setup for a SMT devices infrared soldering rework station,* 1st International Congress on Instrumentation and Applied Sciences ICIAS , 1 (2010).

[26] H. P. Herzig, *Micro-Optics: Elements, Systems And Applications* (Taylor & Francis, 1997).

[27] I. Ashdown and M. Salsbury, *A near-field goniospectroradiometer for LED measurements,* in *International Optical Design Conference 2006*, Vol. 6342, edited by G. G. Gregory, J. M. Howard, and R. J. Koshel (2007) p. 634215.

3

Miniaturized Particulate Matter Sensor For Air Quality Monitoring

Parts of this chapter have been published in IEEE Sensors 2014 Proceedings **2151-2154**, (2014) [1].

When it comes to smart lighting, the objective is to achieve SSL functions beyond illumination. Along with the booming of Internet of Things (IoT), lighting is expected to play a role in the sensory network for IoT applications. In this chapter, we demonstrated a sensor for particulate matter (PM) detection, which can be integrated into lighting. The sensor chip observes the scattered light triggered by particles in a microchamber. The principle of this work is validated by exposing the sensor to cigarette smoke, one of the most common sources of $PM_{2.5}$. Preliminary measurements have demonstrated that the device is capable of detecting the presence of cigarette smoke.

3.1. INTRODUCTION

PARTICULATE matter, specifically fine particles known as $PM_{2.5}$, can be hazardous to human health [2]. $PM_{2.5}$ refers to particles with a diameter of less than 2.5 μm, which comes from various sources, such as power plants, car emission, fire smoke, etc. [3]. These types of fine particles are so small in size that they can penetrate deep into human lungs and bloodstreams without being filtered [4]. It has been reported in many studies that the exposure to heavy $PM_{2.5}$ environment, either from the polluted air or passive smoking, can cause severe issues including increasing asthma attack, lung cancer and cardiovascular disease-related mortality, thus the $PM_{2.5}$ level is often mentioned in the air quality reports as an indicator for the air pollution[5–9].

Measurement of the $PM_{2.5}$ concentration in air is essential to evaluate the air quality[10]. By the time when this study was performed, the approaches for the $PM_{2.5}$ readings are mostly from the official reports published on the internet, which provides the average air quality status for a whole region [11]. However, since the air pollution differs for each place and varies over time, real time locally monitoring devices are desirable to determine individual exposure to $PM_{2.5}$ where people live, work or relax. Very often, lighting is also present in such areas, hence the combination of a $PM_{2.5}$ sensor in a lighting system is the logical next step. The most commonly available detectors, such as nephelometers, cost more than $10K, which are not affordable for personal use [12]. One of the affordable options is Planttower, which costs only around 30$ for one sensor. The detecting chamber from Planttower PMS3003 sensor measures 5.0 cm (length) x 4.3 cm (width) x 2.1 cm (height) in size, with extra PCB modules for the control unit and external modules, which makes the product bulky to integrate with current lighting products [13]. The application of Internet of Things (IoT), specifically the sensory networks, is the great battlefield for the $PM_{2.5}$ detection to be integrated into current lighting products[14–16]. MEMS technology has been considered as a promising technology to miniaturize the sensor chip and offers the possibility to achieve high accuracy with the benefit of lower cost[17, 18].

MEMS particle detectors, such as corona dischargers and micro-film bulk acoustic resonators [19–21], provide good detection results. However, either the high voltage or the complicated fabrication process required are significant challenges. Another $PM_{2.5}$ monitor device based on MEMS technology has been presented by Paprotny [22]. The microfabricated mass-sensitive Film Bulk Acoustic Resonator (FBAR) achieved good sensitivity of 2 $\mu g/m^3$. However, the chip takes up to 10 min integration time to capture the particle signal, limiting the real-time feedback of the device [23]. Among all the different kinds of detection methods, optical methods provide good real-time measure-

ment with promising accuracy [24, 25].

This chapter presents a MEMS $PM_{2.5}$ sensor for air quality detection. The small size (5.2 mm x 4.2 mm x 1 mm) of the whole system allows integration in portable devices and smart lighting resources. Furthermore, a relatively straightforward fabrication process is required, which results in higher yield and, consequently, lower cost for the sensors. Inspired by the nephelometers, the principle used to detect $PM_{2.5}$ in this work is based on light scattering in a microfabricated chamber. The sensing chamber consists of two micromachined silicon chips, one containing a laser diode mounted on top of another one assembled with a photodiode.

The presence of $PM_{2.5}$ in the microfabricated chamber is detected by an increase of the light scattered and sensed by the photodiode. The signal received by the photodiode reflects the detailed information of the particles. The principle of this work is validated by exposing the sensor to cigarette smoke, which is a common $PM_{2.5}$ source. Preliminary measurements show that the sensor is capable of detecting the presence of cigarette smoke. The sensor output (1.235 V) is in a factor of 4.47% higher in the presence of cigarette smoke than in clean air.

3.2. DESIGN PRINCIPLE

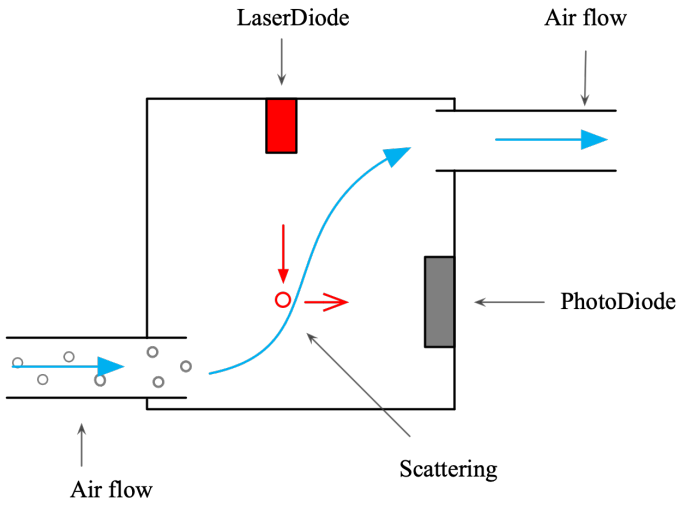

Figure 3.1: The work principle of the optical detection of particles in the microchamber. Without particles in the chamber, the light emitted from the laser diode can hardly reach the photo diode, while when particles are present in the chamber as air flows through, light is scattered by the particles and reaches the photo diode. The signal difference of the photodiode reveals the information about scattering of the particles.

THE particle detector in this work consists of:

1. An inlet which allows the airflow through the microchamber;

2. A measurement chamber assembled by two submounts with cavities, assembled with a laser diode and a photodiode separately;
3. An outlet to exhaust the air;
4. An external fan that provides a constant airflow.

The principle of the optical detection for particles is shown in Figure 3.1. The detection takes place in a microchamber, which contains a laser diode and a photodetector, acting as light source and detector, respectively. Without particles in the chamber, the light emitted from the laser diode can hardly reach the photodiode, while if particles are present in the chamber as air flows through, light is scattered by the particles and reaches the photodiode. The signal difference of the photodiode reveals the information about the scattering of the particles.

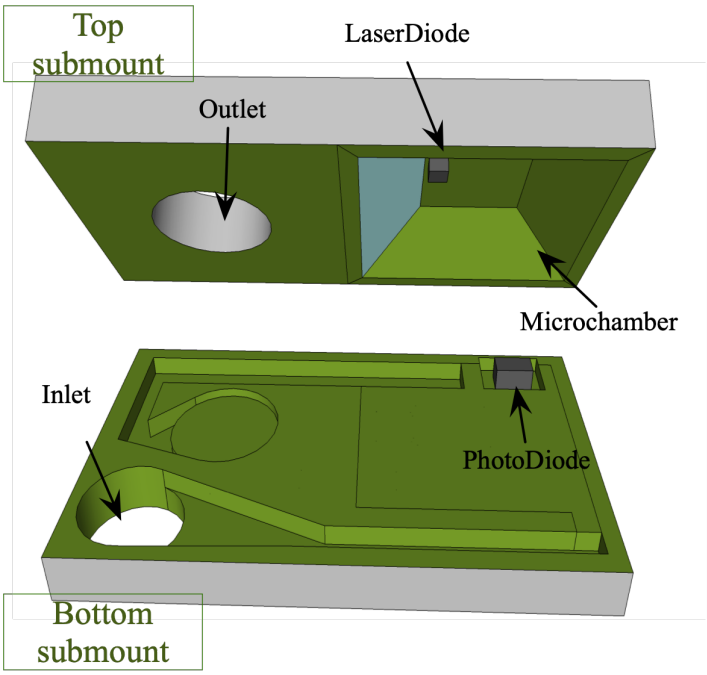

Figure 3.2: Schematic view of the PM sensor, consisting of a microchamber formed by silicon cavity, laser diode as light source, and photo diode as detecting component.

A schematic view of the microsensor is shown in Figure 3.2. A laser diode and photodiode are assembled on different submounts. A patterned Si_3N_4 layer with a controlled thickness was deposited inside the chamber to function as an anti-reflective layer, which absorbs the stray light and increases the signal to noise ratio[26]. The two components are mounted crossing each other inside the microchamber so that light emitted by the

laser diode cannot reach the photodiode directly. When particles flow through the chamber with the airflow, part of the scattered light on the particle comes to the photodiode. The signal obtained from the photodiode provides information about the particles in the air.

3.3. SIMULATION

ACCORDING to the working principle, the scattering of light by the particles will provide the signal that can be detected using a photodiode. To capture the signal as much as possible, it's essential to make sure that:

1. The laser diode is installed in the chamber where it can beam light in the airflow to be scattered on the particles;

2. The laser diode and photodiode are oriented orthogonal from each other so that the photodiode does not receive the direct light from the laser diode, but only captures scattered light from the particles.

Two different types of simulations were made to evaluate the design. A particle trajectory simulation was made to assess the airflow trajectory, to ensure that the laser diode will be located in the chamber where its emitted light can project on the airflow, with minimal stray light on the photodetector, followed by a TracePro simulation to estimate the raytracing in the microchamber, specifically the light that the laser diode can receive where particles are scattering the light.

3.3.1. PARTICLE TRAJECTORIES

A simplified 3D structure of the microsensor is built up to simulate the airflow trajectories in the microchamber. The simulations are performed with Comsol using the models: *laminar flow* and *particle tracing for fluid flow*. The initial values for the simulations have been calculated using the performance curve of the micro fan and assuming that the fluid is incompressible and Newtonian. The flow is assumed to be laminar, and the channel is approximated to be cylindrical. A pressure drop of 2 Pa and a flow rate of 0.1 m^3/s have been used in the calculation.

The simulated particle trajectories are presented in Figure 3.3, with the lines representing the airflow trajectories and lateral bars indicating the velocity of the flow. As indicated by the simulation, the trajectories in the microchamber focus on where the laser diode and photodiode are placed, indicating that the airflow will pass by the laser diode, which projects lights in the chamber. The particles along with the airflow, can then scatter the light from the laser diode and reach the photodiode placed in the chamber.

3.3.2. RAYTRACING IN THE MICRO CHAMBER

In order to assess the impact of the scattering, the distribution of light reaching the photodiode in the microchamber is calculated with TracePro. The laser diode and photodiode characteristics are imported from the respective datasheet [27, 28]. In an ideal clean air situation when there are no particles in the microchamber, light emitted from the

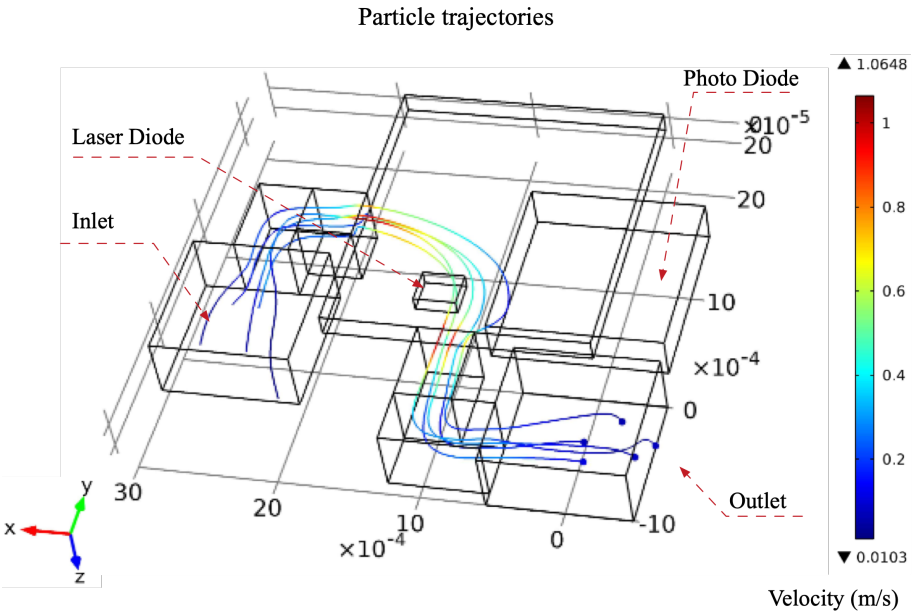

Figure 3.3: Simplified 3D geometry. Airflow goes through the chamber where the laser diode is installed so that the particles along with the airflow scatter the light which is in turn detected by the photodiode

laser diode can hardly reach the laser diode. At the presence of particles, light is scattered by particles passing through the chamber, where the particle trajectory discussed as aforementioned, and a significant part of the scattered light can directly reach the photodiode. In this way, the signal received by the photodiode gives information about particles in the airflow.

The ray traces simulations in the chamber are shown in Figure 3.4, where the colour of each ray traced indicates the flux of the ray. Red rays represent flux from 100 to 66 percent of their beginning ray flux, while green rays have flux between 66 and 33 percent, and blue rays are between 33 and 0 percent. In Figure 3.4a while there are no particles in the chamber, the rays get attenuated in the chamber and only blue rays (very low percentage ranging from 0 to 33% of the ray flux) can reach the photodiode. In Figure 3.4b, when particles are passing through the beam path of the laser diode, many more rays, including red and green rays, which have a much higher percentage of the beginning ray flux, can reach the photodiode.

The spatial distribution of the rays on the photodiode surface can be found in Figure 3.5. (a) While there are no particles in the chamber, only a small part of the light reaches the photodiode. This is reflected by the irradiance map where only one single dot is showing up; (b) When particles are showing up along the pathway of the laser diode, as per the densely distributed dots on the irradiance map, a significant increase of scattered light reaches the photodiode.

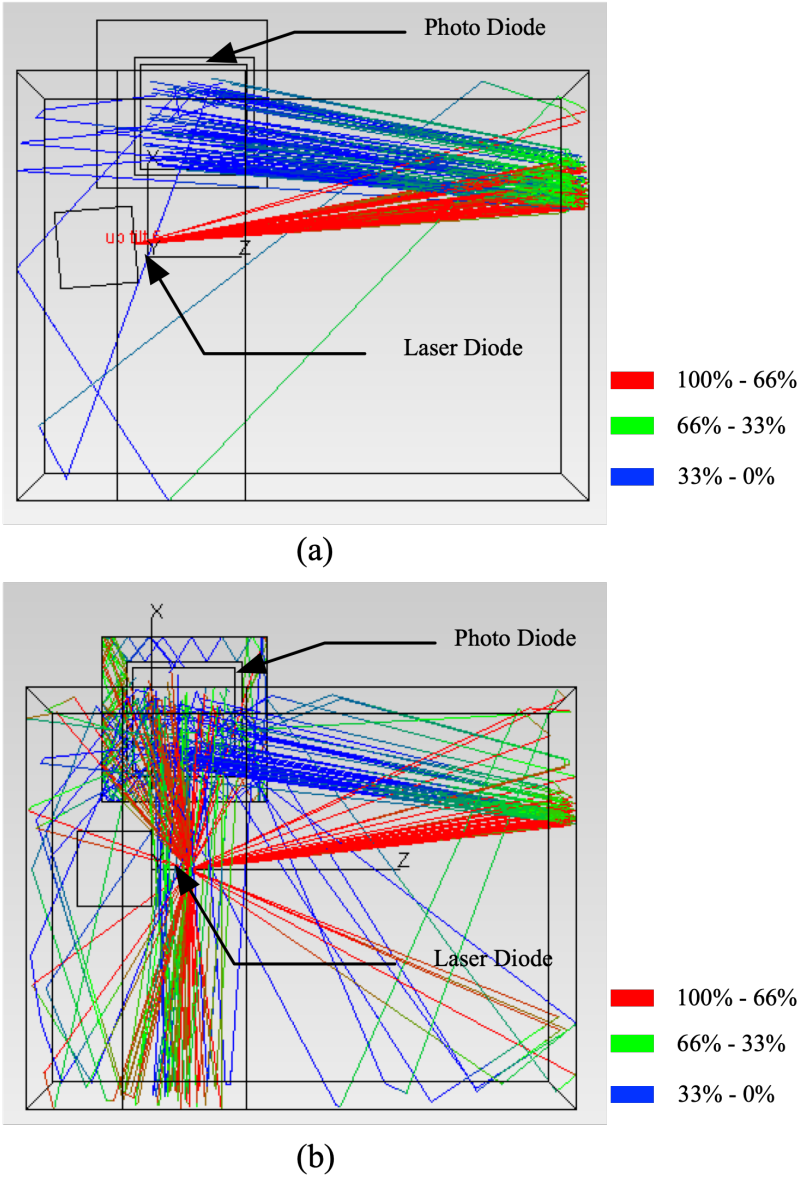

Figure 3.4: Raytracing in the micro chamber using TracePro, with RGB color indicating the percentage of the beginning ray flux from the laser diode. (a) When there's no particles in the chamber, only blue rays which is very low percentage of beginning ray flux reaches the photodiode (b) When there's particles in the chamber, red and green rays reach the photodiode, indicating much higher percentage of beginning ray fluxes are received.

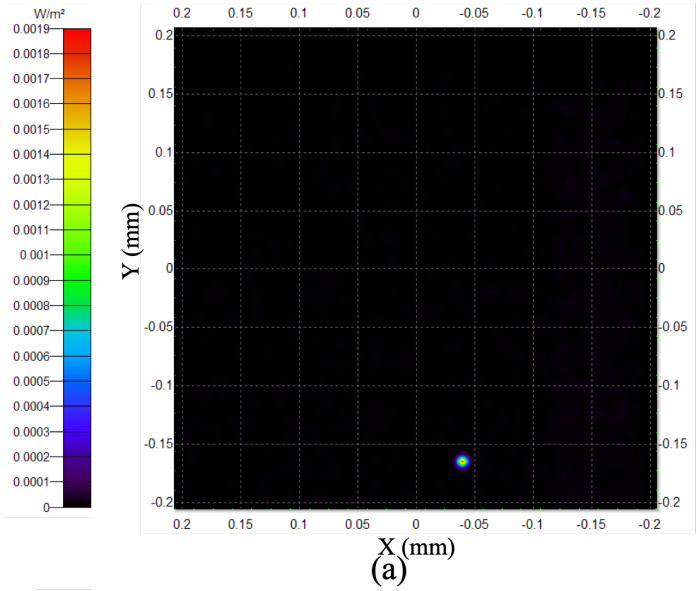

Figure 3.5: Irradiance illuminance map for the photodiode surface. Only small part of the light reaches the photodiode with no PM in the microchamber; (b) significant increase of scattered light that reaches the photodiode when the presence of particles is simulated in the microchamber.

3.4. CONTROL CIRCUIT

AN in-house control circuit was designed to process the signal received from the designed sensor unit. The schematics of the control circuit are as shown in Figure 3.6. A laser diode is powered by a pulse width modulation (PWM) signal. At the reception side, a photodiode captures the scattered light, and the signal is amplified by an amplifier and readout by an oscilloscope.

As the light source in the detector, the laser diode (Roithner Chip-650-P10) emits light with a wavelength of 650 nm. A liner driver is used to drive the laser diode, generated by the PIC16 MCU, sourced by 3.6 V programmed by the function generator with a pulse signal. The reception of the photodiode (EPIGAP EPC-660-0.5) is equipped with an MCP6191 operational amplifier functioning as the core of the readout circuit, from which the signal can be read out by the oscilloscope.

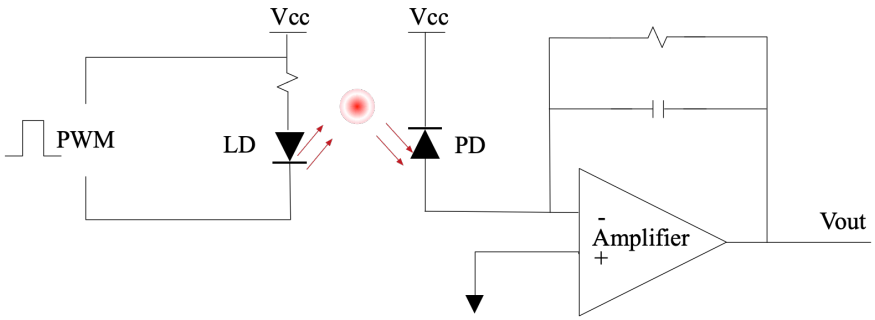

Figure 3.6: Schematics of the control circuit of the sensor. The Lasor diode is powered by PWM signal, the scattered light captured by photodiode is amplified and read out by oscilloscope.

3.5. FABRICATION

THE micro PM sensor chip consists of two submounts, including a top wafer with a laser diode, and a bottom wafer mounted with the photodiode. Both submounts are fabricated with cavities and electric pads. The fabrication of the two submounts is using the same process, though the masks used for patterning the structures on each wafer are different. The main fabrication steps, depicted in Figure 3.7, are as follows:

1. Deposition of Si_3N_4 (500 nm) using low pressure chemical vapor deposition (LPCVD) on both sides the Si wafer, followed by plasma etching to get the Si_3N_4 pattern on the front side, which severs as the mask for KOH etching.

2. Silicon etching in KOH to create cavities on the front side of the Si wafer, to form a microchamber for the air to flow through;

3. Wet etching till the whole nitride layer is stripped;

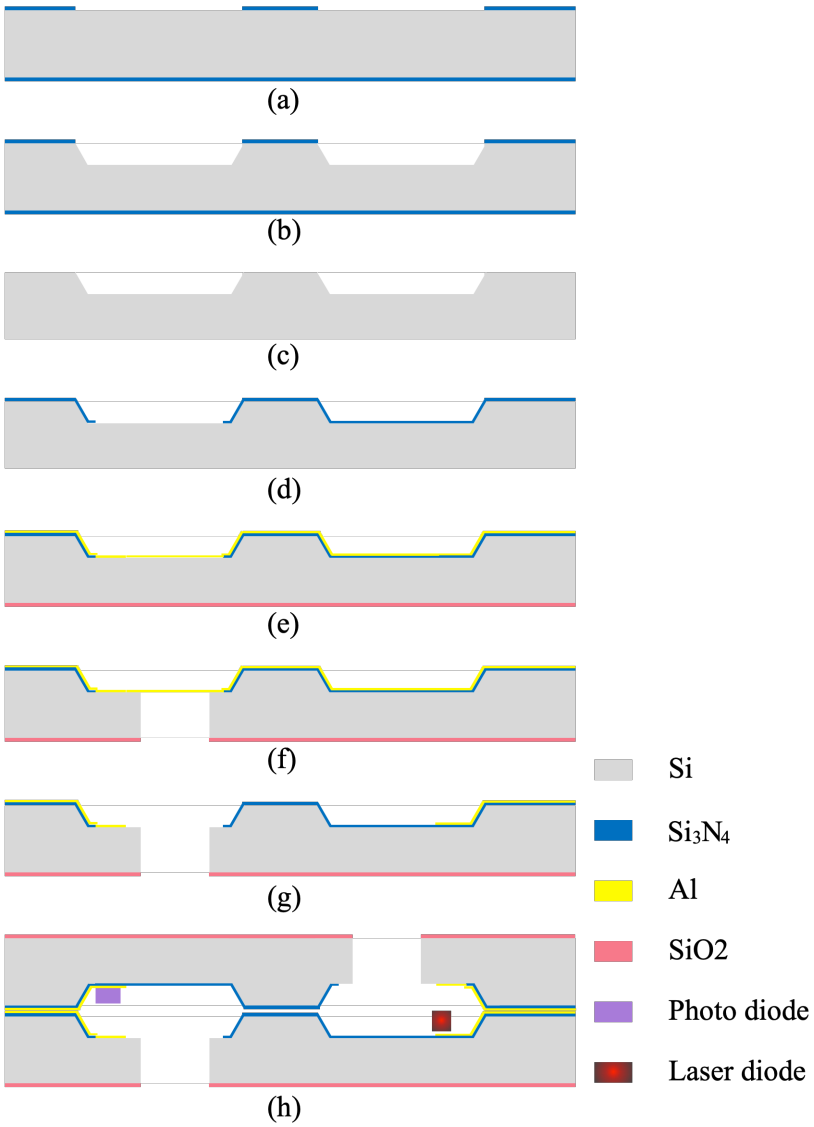

Figure 3.7: Main process steps for the fabrication: (a) LPCVD Si_3N_4 layer for KOH pattern; (b) KOH etching for cavity; (c) remove residual Si_3N_4 layer; (d) LPCVD another Si_3N_4 layer as anti-reflective coating; (e) deposit SiO_2 layer on the backside, and sputter Al layer on the front side; (f) DRIE etching for though hole opening on the backside; (g) pattern the Al layer on the front side for electricity contact; (h) assemble the two submounts after bonding photodiode and laser diode on each one.

4. Deposition of another layer of Si_3N_4 of 100 nm using LPCVD, followed by plasma etching for Si_3N_4 on the front side for anti-reflective coating pattern in the cavi-

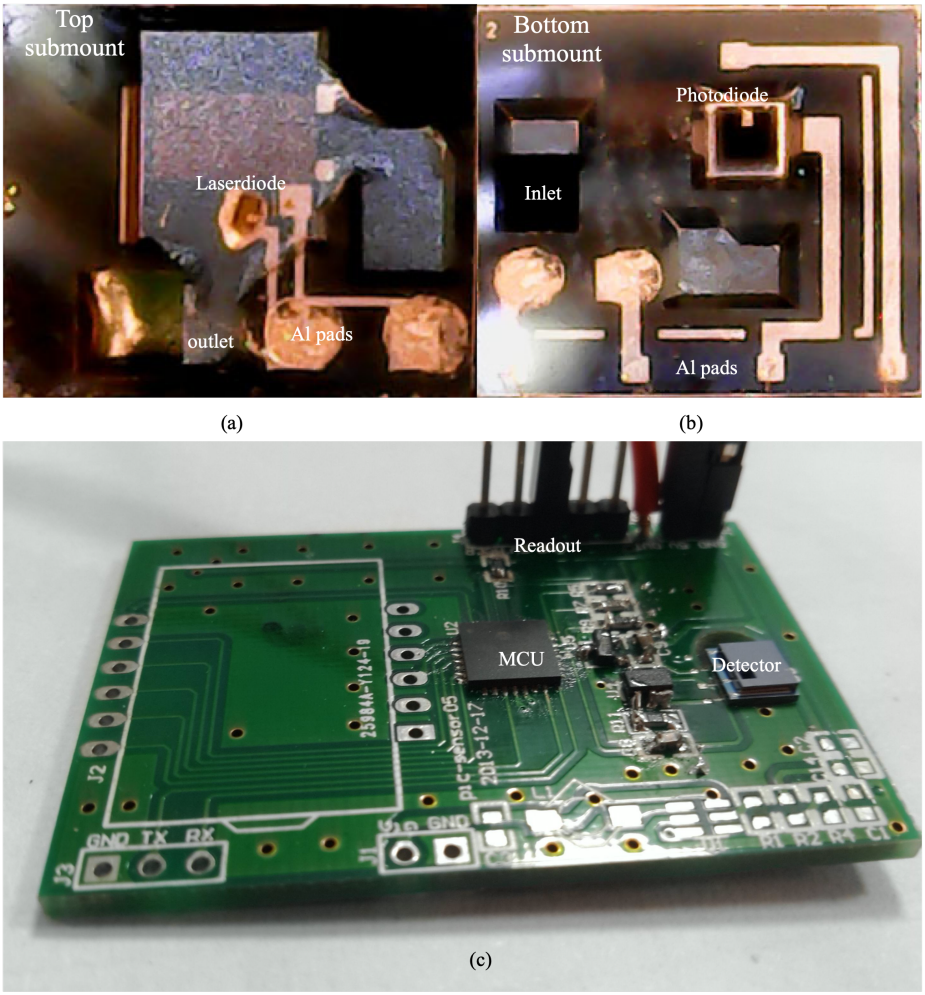

Figure 3.8: (a) Top submount and (b) bottom submount with cavities and Al contacts to form the micro chamber; (c) The bonded submounts packaged on PCB board with a control circuit design.

ties, and etch the whole backside. This remaining Si_3N_4 layer in the cavities are acting as an anti-reflective coating layer to help attenuate the direct light from the laser diode and prevent them from reflecting to the photodiode, thus enhance the signal-to-noise ratio for optical detection;

5. Deposition of SiO_2 on the backside of 6 μm (PECVD) as a mask layer for the following Deep reactive-ion etching (DRIE) etching, sputtering of an Al layer on the front side which provides a stop layer on the front side for the upcoming DRIE processing, and a metallization layer for electrical contacts in the last step;

6. DRIE etching for through wafer opening from the backside, to create the inlet and outlet connecting with the microchamber;

7. Patterning of the Al layer (wet etching) on the front side of the Si wafer, to define the electric contacts;

8. Assembling of the photodiode on the bottom submount, and of the laser diode on the top submount, and adhesive bonding of the two submounts after wirebond for the contacts.

The fabricated device is shown in Figure 3.8(a,b). The two submounts were bonded together and assembled on a PCB with an ad-hoc control circuit design, as shown in Figure 3.8c. Under the laboratory environment, the airflow going through the microchamber is very low. To accelerate the verification process, a Sunon micro fan FB385 was used to create a constant accelerated airflow so that the air in the micro-chamber will exchange with air from the environment much quicker, which in turn makes the sensor detecting the environmental change with low latency.

3.6. EXPERIMENTAL RESULTS

THE fabricated prototype of the microsensor unit was tested in a closed chamber blown with particulate matter source to simulate the environmental change. A single lit cigarette is used as the particulate source in the test, the test setup is as depicted in Figure 3.9. Cigarette smoke particles range from 0.1 to 0.01 μm in diameter, and it is a source of high concentration smoke giving particle concentration values as high as 300 $\mu g/m^3$ [29, 30]. The drastic particle concentration of cigarette smoke makes it a great source for the demonstration of the sensor performance.

The baseline of the laser diode reception is recorded by installing the detection unit in the aforementioned closed chamber with clean air. The clean air here indicates that the detector is placed in the same environment as the lab, where no clear pollutant was present. It indicates the baseline of the test, instead of looking for the absolute clean air without any particles. The average output from the detector is around 1.182 V at the on the state of the pulse. With the same setup, we then lit a cigarette into the chamber, the output of the photodiode went up to 1.235 V. A 54 mV difference between the two measurements was observed as shown in Figure 3.10. The gap between the two readouts indicates that the existence of the cigarette particles brings more scattering thus more light could reach the photodiode.

The statistics of the data collected from the measurements can be found in Table 3.1. Two full pulses from each readout were captured, represented by the state S_{AB}, where A means the pulse on or off, and B indicated the sequence of the state. Under *Non Smoke* environment, the first readout at pulse on state S_{ON_1} has average 1.182 V, with a standard deviation of 0.0054 V. While under the Smoke environment, the first readout at pulse on state S_{ON_1} has increased to average of 1.24 V, with a standard deviation of 0.019 V, contributing a difference of:

$$\Delta = 1.24–1.182 = 0.053V \tag{3.1}$$

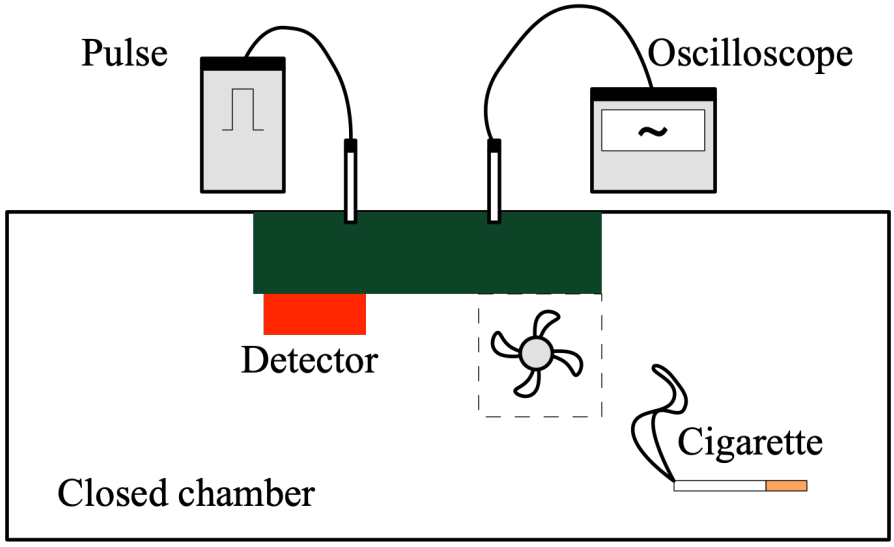

Figure 3.9: The particle detector is placed in a closed chamber to measure the readout when lit with a cigarette. A pulse signal powered by PWM signal is used to drive the laser diode, along with an oscilloscope to record the readout of the photodiode. A fan is used to help circulate the air into the microchamber in the detector.

Non Smoke				
	S11 (V)	**S01 (V)**	**S12 (V)**	**S02 (V)**
mean	1	0.001378	1.179467	0.001452
std	0.005435	0.002454	0.005937	0.002443
25%	1.17849	-0.000186	1.17531	-0.000186
50%	1.18231	0.001306	1.1792	0.00137
75%	1.18608	0.002862	1.18335	0.002927

Smoke				
	S11 (V)	**S01 (V)**	**S12 (V)**	**S02 (V)**
mean	1.235136	0.004716	1.23457	0.004925
std	0.018556	0.00531	0.018192	0.006645
25%	1.22117	0.001111	1.22097	0.000008
50%	1.23096	0.003186	1.23051	0.0039
75%	1.24776	0.007078	1.24672	0.008181

Table 3.1: The statistics of the processed data collected from the measurements. A clear difference of mean value is obtained from the two datasets collected with cigarette lit before (*Non Smoke*) and after (*Smoke*).

$$r = 0.053/1.182 = 4.47\% \tag{3.2}$$

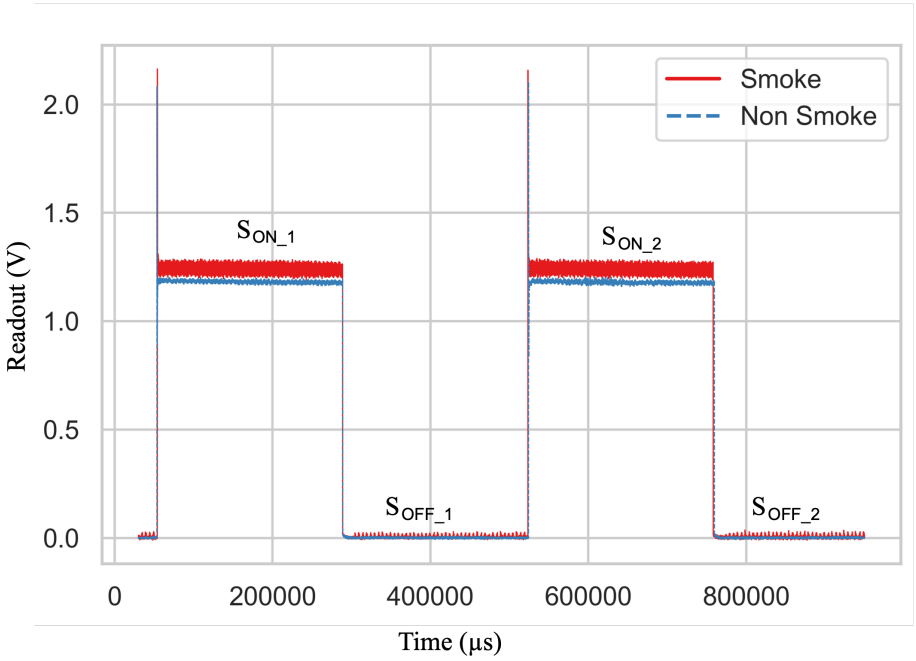

Figure 3.10: Results obtained from a cigarette lit before and after. A 54 mV difference between the two measurements was observed, indicating that much more light was scattered by the smoke and reached the photodiode.

In order to compare the two distributions of the readouts, specifically when the pulse is on (S_{ON_1}), a violin chart is plotted to show the distributions of the signals captured from both the readout. As shown in the plot in Figure 3.11, the three lines in each violin represent the third quartile, mean, and first quartile separately. The range between the first quartile and third quartile indicates the interquartile range as a measure of the statistic dispersion. The width of the violins represents the kernel density of the data distribution. Wider sections of the violin plot represent a higher population of the measured data are distributed, while the skinnier sections represent a lower probability. The violin distribution for *Smoke* state is taller, with a higher interquartile range, indicating a greater standard deviation for the readout, while under *Non Smoke* state, the distribution is very much normally distributed, which serves as a baseline for the readout. Despite that the *Smoke* violin has greater deviation, the 54 mV difference is in a factor of 4.47% higher.

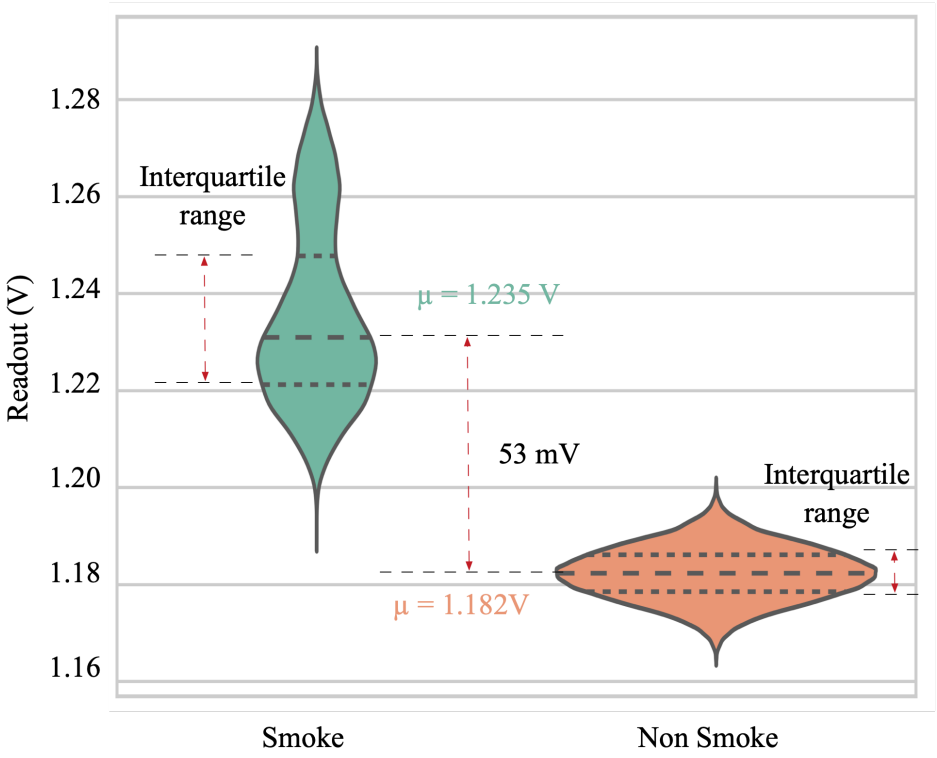

Figure 3.11: A violin plot to show the distribution of the two readouts at pulse on state S_{ON_1}. The readout distribution for *Smoke* environment is widely spreaded, with much higher interquartile range, indicating a greater standard deviation for the readout, while under *Non Smoke* environment, the distribution is very much normally distributed. The 54 mV difference between the two readouts are distinguishable.

Due to the limitation of the equipment, by the time when the experiments were performed, we didn't have the perfect setup to measure the particle counts in the air, without which it's not possible to conclude a clear prediction on the sensitivity of the detector. from the reference, we can estimate that the particle concentration in the cigarette smoke sample is approximately 200 $\mu g/m^3$, while 25 $\mu g/m^3$ represents the EU standard for good air quality[2]. We can briefly obtain a rough sensitivity to cigarette smoke of

$$S = 53/(200-25) = 0.30 mV/\mu g/m^3 \tag{3.3}$$

Under this assumption, and considering that the signal standard deviation in clear air is 5.4 mV, we obtain a Limit of Detection (LoD) of

$$LoD = 5.4/0.30 = 18 \mu g/m^3 \tag{3.4}$$

However, the sensitivity is still low compared to the normal polluted air, which is around 150 $\mu g/m^3$ as a hazardous indication. Several reasons may account for its low

sensitivity. First, during the assembling process, the laser diode and photodiode are mounted on the wafers manually, of which the direction and the location will bring lots of deviation to the detection; second, the laser diode is emitting light from a wider angle than the angle defined in its product instruction, which brings much noise to the detector. These parameters shall be considered in future work.

The objective of the MEMS $PM_{2.5}$ sensor is to have a direct relationship between the output of the photodiode and the $PM_{2.5}$ concentration in the air. However, like any other light-scattering instrument, the MEMS sensor can respond differently to particles of varying compositions, thus the sensor will require a separate mass calibration factor for specific aerosols. In this work, only the design, fabrication, and measurement principle of the sensor is presented. The calibration of the device requires an extensive work and has been mentioned in Dr. Mingzhi Dong's work [31]. With more precise equipment to measure the particle size and concentration data, and most importantly, the upgraded design, the detection for particles has been approved to be qualified for detecting the air quality with great potentials in the commercial applications.

3.7. CONCLUSION

IN this chapter, we proposed a miniaturized particulate matter sensor based on light scattering. Particles passing through the microchamber can be detected due to the light scattering signal captured by the photodiode in the microchamber. Preliminary results show that tobacco smoke can be detected by this device. The presence of tobacco smoke gives an output (1.235 V), which is 4.47% higher than in in the clean air. The device was fabricated in unsophisticated processing, which allows for higher yield and low cost

This work is an initial demonstration of the idea of MEMS integrated design for $PM_{2.5}$ detection. The compatible design with a clear signal for the air quality has demonstrated its use to be integrated into the sensory networks for air quality detection.

REFERENCES

[1] X. Li, E. Iervolino, F. Santagata, J. Wei, C. A. Yuan, P. Sarro, and G. Zhang, *Miniaturized particulate matter sensor for portable air quality monitoring devices,* in *IEEE SENSORS 2014 Proceedings* (IEEE, 2014) pp. 2151–2154.

[2] E. Commission, *Air Quality Standards,* Accessed: 26-Oct-2019.

[3] U.S. Environmental Protection Agency, *Particulate Matter,* Accessed: 08-Jul-2014.

[4] S. K. Sahu, M. Tiwari, R. C. Bhangare, and G. G. Pandit, *Particle size distribution of mainstream and exhaled cigarette smoke and predictive deposition in human respiratory tract,* Aerosol and Air Quality Research **13**, 324 (2013).

[5] R. D. Brook, S. Rajagopalan, C. A. Pope, J. R. Brook, A. Bhatnagar, A. V. Diez-Roux, F. Holguin, Y. Hong, R. V. Luepker, M. A. Mittleman, A. Peters, D. Siscovick, S. C. Smith, L. Whitsel, and J. D. Kaufman, *Particulate matter air pollution and cardiovascular disease: An update to the scientific statement from the american heart association,* (2010).

[6] C. A. Pope, R. T. Burnett, M. J. Thun, E. E. Calle, D. Krewski, K. Ito, and G. D. Thurston, *Lung cancer, cardiopulmonary mortality, and long-term exposure to fine particulate air pollution,* Journal of the American Medical Association (2002), 10.1001/jama.287.9.1132.

[7] C. Arden Pope, R. T. Burnett, M. C. Turner, A. Cohen, D. Krewski, M. Jerrett, S. M. Gapstur, and M. J. Thun, *Lung cancer and cardiovascular disease mortality associated with ambient air pollution and cigarette smoke: Shape of the exposure-response relationships,* Environmental Health Perspectives **119**, 1616 (2011).

[8] R. D. Peng, H. H. Chang, M. L. Bell, A. McDermott, S. L. Zeger, J. M. Samet, and F. Dominici, *Coarse particulate matter air pollution and hospital admissions for cardiovascular and respiratory diseases among medicare patients,* JAMA - Journal of the American Medical Association **299**, 2172 (2008).

[9] J. Fan, S. Li, C. Fan, Z. Bai, and K. Yang, *The impact of PM2.5 on asthma emergency department visits: a systematic review and meta-analysis,* Environmental Science and Pollution Research (2016), 10.1007/s11356-015-5321-x.

[10] O. Raaschou-Nielsen, Z. J. Andersen, R. Beelen, E. Samoli, M. Stafoggia, G. Weinmayr, B. Hoffmann, P. Fischer, M. J. Nieuwenhuijsen, B. Brunekreef, W. W. Xun, K. Katsouyanni, K. Dimakopoulou, J. Sommar, B. Forsberg, L. Modig, A. Oudin, B. Oftedal, P. E. Schwarze, P. Nafstad, U. De Faire, N. L. Pedersen, C. G. Östenson, L. Fratiglioni, J. Penell, M. Korek, G. Pershagen, K. T. Eriksen, M. Sørensen, A. Tjønneland, T. Ellermann, M. Eeftens, P. H. Peeters, K. Meliefste, M. Wang, B. Bueno-de Mesquita, T. J. Key, K. de Hoogh, H. Concin, G. Nagel, A. Vilier, S. Grioni, V. Krogh, M. Y. Tsai, F. Ricceri, C. Sacerdote, C. Galassi, E. Migliore, A. Ranzi, G. Cesaroni, C. Badaloni, F. Forastiere, I. Tamayo, P. Amiano, M. Dorronsoro, A. Trichopoulou, C. Bamia, P. Vineis, and G. Hoek, *Air pollution and lung cancer incidence in 17 European cohorts: Prospective analyses from the European Study of Cohorts for Air Pollution Effects (ESCAPE),* The Lancet Oncology (2013), 10.1016/S1470-2045(13)70279-1.

[11] V. Isakov, S. Arunachalam, R. Baldauf, M. Breen, P. Deshmukh, A. Hawkins, S. Kimbrough, S. Krabbe, B. Naess, M. Serre, and A. Valencia, *Combining dispersion modeling and monitoring data for community-scale air quality characterization,* Atmosphere **10** (2019), 10.3390/atmos10100610.

[12] J. G. Watson, J. C. Chow, H. Moosmuller, M. Green, N. Frank, and P. Marc, *Environmental Protection Agency Research Triangle . . .*, Tech. Rep. May (1998).

[13] T. Zheng, M. H. Bergin, K. K. Johnson, S. N. Tripathi, S. Shirodkar, M. S. Landis, R. Sutaria, and D. E. Carlson, *Field evaluation of low-cost particulate matter sensors in high-and low-concentration environments,* Atmospheric Measurement Techniques **11**, 4823 (2018).

[14] Huawei, *5G for IoT and Mobile*, Tech. Rep. (Huawei, 2016).

[15] KPMG, *Converging 5G and IoT : a faster path to smart manufacturing*, Tech. Rep. (KPMG, 2019).

[16] H. Martin, *6 ways lighting can be used for more than illumination,* Accessed: 18-Jan-2016.

[17] H. P. Herzig, *Micro-Optics: Elements, Systems And Applications* (Taylor & Francis, 1997).

[18] Z. K. Esfahani, T. Ma, H. V. Zeijl, and G. Q. Zhang, *Blue Selective Photodiodes for Optical Feedback in LED Wafer Level Packages,* (2014).

[19] J. Black, A. Elium, R. White, M. Apte, L. Gundel, and R. Cambie, *6D-2 MEMS-Enabled Miniaturized Particulate Matter Monitor Employing 1.6 GHz Aluminum Nitride Thin-Film Bulk Acoustic Wave Resonator (FBAR) and Thermophoretic Precipitator,* in *2007 IEEE Ultrasonics Symposium Proceedings*, Vol. 4 (IEEE, 2007) pp. 476–479.

[20] A. Wexler, N. Tien, D. Niemeier, and B. Holmen, *Electrical Mobility Separation of Airborne Particles Using Integrated Microfabricated Corona Ionizer and Separator Electrodes,* Journal of Microelectromechanical Systems **18**, 4 (2009).

[21] A. Hajjam, J. C. Wilson, and S. Pourkamali, *Individual air-borne particle mass measurement using high-frequency micromechanical resonators,* IEEE Sensors Journal **11**, 2883 (2011).

[22] I. Paprotny, F. Doering, P. a. Solomon, R. M. White, and L. a. Gundel, *Microfabricated air-microfluidic sensor for personal monitoring of airborne particulate matter: Design, fabrication, and experimental results,* Sensors and Actuators A: Physical **201**, 506 (2013).

[23] H. Lim, D. Park, J. Maeng, J. Hwang, and Y. Kim, *Mems based integrated particle detection chip for real time environmental monitoring,* in *19th IEEE International Conference on Micro Electro Mechanical Systems*, Proceedings of the IEEE International Conference on Micro Electro Mechanical Systems (MEMS) (2006) pp. 62–65.

[24] B. Giechaskiel, M. Maricq, L. Ntziachristos, C. Dardiotis, X. Wang, H. Axmann, A. Bergmann, and W. Schindler, *Review of motor vehicle particulate emissions sampling and measurement: From smoke and filter mass to particle number,* Journal of Aerosol Science **67**, 48 (2014).

[25] M. Dong, E. Iervolino, F. Santagata, G. Zhang, and G. Zhang, *Silicon microfabrication based particulate matter sensor,* Sensors and Actuators, A: Physical (2016), 10.1016/j.sna.2016.05.036.

[26] T. Iwahashi, M. Morishima, T. Fujibayashi, R. Yang, J. Lin, and D. Matsunaga, *Silicon nitride anti-reflection coating on the glass and transparent conductive oxide interface for thin film solar cells and modules,* Journal of Applied Physics (2015), 10.1063/1.4932639.

[27] EPIGAP, *Photodiode EPC-660-0.5,* (2014), accessed: 06-Jun-2014.

[28] Roithner, *Laser Diode Chip-650-P10,* (2014), accessed: 06-Jun-2014.

[29] M. H. Becquemin, J. F. Bertholon, M. Attoui, F. Roy, M. Roy, and B. Dautzenberg, *Particle size in the smoke produced by six different types of cigarette,* Revue des maladies respiratoires **24**, 845 (2007).

[30] D. M. Bernstein, *A review of the influence of particle size, puff volume, and inhalation pattern on the deposition of cigarette smoke particles in the respiratory tract,* Inhalation Toxicology **16**, 675 (2004).

[31] M. Dong, *TU Delft*, Ph.D. thesis, TU Delft (2016).

4

STRETCHABLE BINARY FRESNEL LENS FOR FOCUS TUNING

Parts of this chapter have been published in conference proceeding Transducers 2015 [1] and Scientific Reports **6**, 25348 (2016) [2]. The results of this work has been reported on electronics industry magazine EETimes [3]

In the previous chapters, the spotlight was on the external applications of solid state lighting (SSL). Nevertheless, smart lighting is much more than that. When it comes to the microfabrication universe, the core Light-emitting diode (LED) chip units powering the illumination can also be integrated with micro systems to gear up with characters to achieve tunable optics. In this chapter a micro flat optics with focus tuning is demonstrated to be equipped in the SSL chips.

The proposed optics in this chapter is a micro Fresnel lens produced by wafer-level microfabrication. The lens is fabricated by encapsulating lithographically defined vertically aligned carbon nanotube (CNT) bundles inside a polydimethylsiloxane (PDMS) layer. The composite material of the lens combines the excellent optical absorption properties of CNT with the transparency and stretchability of PDMS. By stretching the elastomeric composite in a radial direction, the the focal length of the lens is tuned accordingly. The good focusing response is demonstrated and a large focus change was achieved by radially stretching the lenses.

4.1. INTRODUCTION

A tuneable lens plays a significant role in adaptive illumination, beam shaping and optical communication, where controllable focal length is required for many scenarios [4]. Various and remarkable techniques to obtain focus change are proposed in the literature. For example, a lens based on liquid filled elastomer shells was used to create a dual mode meniscus lens, by tuning the pressure of the micro chamber formed by the elastomer [5], it has the drawback of lens shape instability and temperature sensitivity. Less robust solutions have also been proposed which rely on electrostatically controlling the contact angle of a liquid lens on a substrate [6], [7]. In another approach, a fixed optical element was mounted on a large displacement actuator to adjust the lens focal length [8], [9], which results in a bulky system not suitable for miniaturization due to the assembly of individual parts. Depending on the applications, the reported concepts have different focal length ranges to support their specific applications. However, significant challenges are encountered when the systems are miniaturized and when the size and shape of the lens need to be adaptive.

A micro binary amplitude Fresnel lens uses micro-structured patterns to spatially modulate the intensity distribution of the light passing through. It is a type of diffractive optics that is flat in surface but achieves the same optical property as curved optics due to wave propagation [10]. The micro Fresnel lens has been demonstrated in applications such as holograms [11], 3D integral imaging [12], and laser processing [13]. When it comes to the miniaturization of lenses, traditional optics suffer from lens surface curvature, small numerical apertures which results in increased difficulty in fabrication. Diffractive optics, which doesn't require perfect curve shape for the optics, but a rather patterned structure which manipulate the lights with the same amplitude, have the advantages of being flat and thin. Furthermore, their structure shows excellent compatibility with micro fabrication technologies, thus bringing more freedom to the lens design [14].

In diffractive optics, the opaque region is critical for the redistribution of light. Materials such as aluminum [15], silicon [16], CNT [10] and graphene [17] have been reported as suitable opaque materials. Among them, CNT is an excellent candidate ma-

terial due to the very high optical absorption of the material [18]. Furthermore, the fast growing CNT bundles in photo-lithographically defined patterns, have been recognized as an excellent structural material for the fabrication of high-aspect-ratio deformable 3D micro-structures [19]. Most of the reported micro Fresnel lenses are fabricated using rigid materials and cannot be adaptive. However some recent progress has been made using silicon nanowires combined with a flexible polymer to show that a large field of view change is possible by bending the substrate [20].

In this chapter, we report on a micro Fresnel lens composed of CNT embedded inside PDMS, a polymer with great optical transparency, stretchability and bio-compatibility [21]. The PDMS is employed as both the transparent optical lens material and as stretchable substrate supporting the CNT lens. The vertically aligned CNT, with excellent light absorption properties, is employed as the opaque material for the binary amplitude Fresnel lens [1]. The lens formed by the CNT/PDMS composite changes its focal length by stretching the substrate.

4.2. DESIGN PRINCIPLE

A binary amplitude diffractive lens consists of alternating opaque and transparent zones, as shown in Figure 4.1, where the blue zones represent the opaque zones, and the pitches between the blue zones represent the transparent zones. The focal length f of the lens is related to the ring number n (n=1,2,...), the ring radius r_n and the wavelength λ of the illuminating light [22].

$$f = \frac{r^2}{n\lambda} \tag{4.1}$$

The zones between the adjacent rings are the alternating opaque and transparent. In this work the optics fabrication is strongly dependent on the opaque material, thus we focus on the opaque zones, denoted as z_1, z_2, etc. As depicted in Figure 4.1, z_1 represents the primary focus (n=1), while z_2 is the zone between r_2 and r_3, and z_3 is the zone between r_4 and r_5. The rest can be done in the same manner as:

$$z_1 = r_1 \tag{4.2}$$

$$z_2 = r_3 - r_2 \tag{4.3}$$

$$z_3 = r_5 - r_4 \tag{4.4}$$

...

$$z_n = r_{2n-1} - r_{2n-2} \tag{4.5}$$

When the ring radius r_n increases by the stretching factor s to $r'_n = s * r_n$, the new focal length f' of the lens increases by a factor of s^2,

$$f' \quad = \frac{r'^2_n}{n\lambda} \quad = \frac{(sr_n)^2}{n\lambda} \quad = \mathbf{s^2} f \tag{4.6}$$

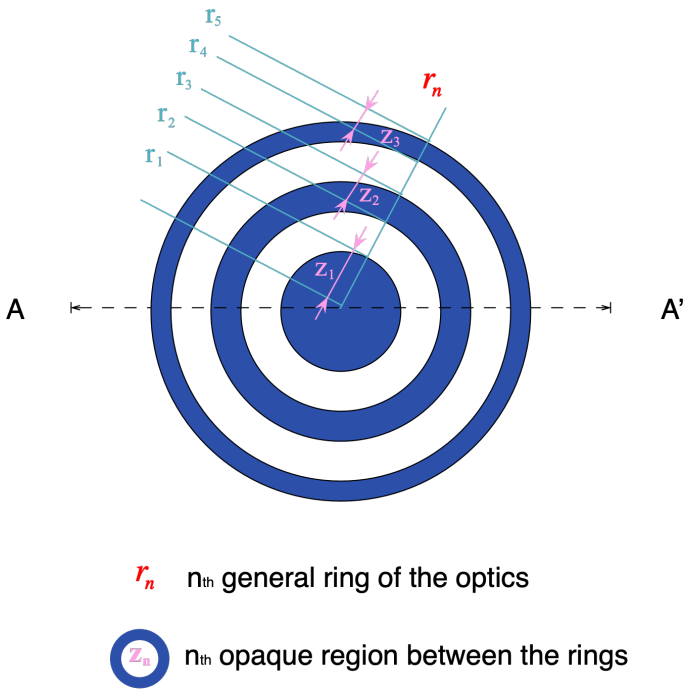

Figure 4.1: Schematics of the Fresnel lens. The focal length f of the lens is related to the ring number n (n=1,2, ...), the ring radius r_n.

According to Equation 4.1 and Equation 4.5, the focal length is dependent on the radii of the ring patterns. Given that the lens is working under the same conditions (wavelength of the light and the ring numbers of the optics are constant), a lens with a higher radius (with a factor of s) of the rings has a higher focal length (by a factor of s^2). Meaning that when increasing the radii of the rings, the focal length gets amplified by s^2 accordingly.

n_{th} **ring's radii** (μm)	**n=1**	**n=2**	**n=3**	**n=4**	**n=5**
f=7 (mm)	66.7	94.3	115.5	133.3	149.1
f'**=7.7 (mm)**	69.9	98.9	121.1	139.8	156.4
r'_n/r_n	1.0488	1.0488	1.0488	1.0488	1.0488

Table 4.1: Comparison of two Fresnel optics with different focal length. The ratio between the ring size (r_n v.s. r'_n) is a constant.

To get a better feeling on the radius for each ring, a comparison of two Fresnel optics

with different focal lengths is listed in Table 4.1. For the wavelength of 635 nm, the focal length is set to be 7 mm and 7.7 mm. The details of the radii for the rings of each optics are as shown in the table. The ratio of the n_{th} radius r'/r is in a factor of 1.0488 (e.g. the primary ring r_1 for f is 66.7 μm, while the primary ring r_1' for f' is 69.9 μm), which contributes to a factor of the focal length that f'/f = 1.04882 = 1.1.

The diffraction efficiency of the lens is majorly determined by its primary focus(the inner zone in the center, n=1) [22], due to that the light beam at the primary ring has the highest intensity. We can design a lens with adaptive size and highly sensitive focus tuning which strongly depends on the radius of the inner ring, as schematically depicted in Figure 4.2.

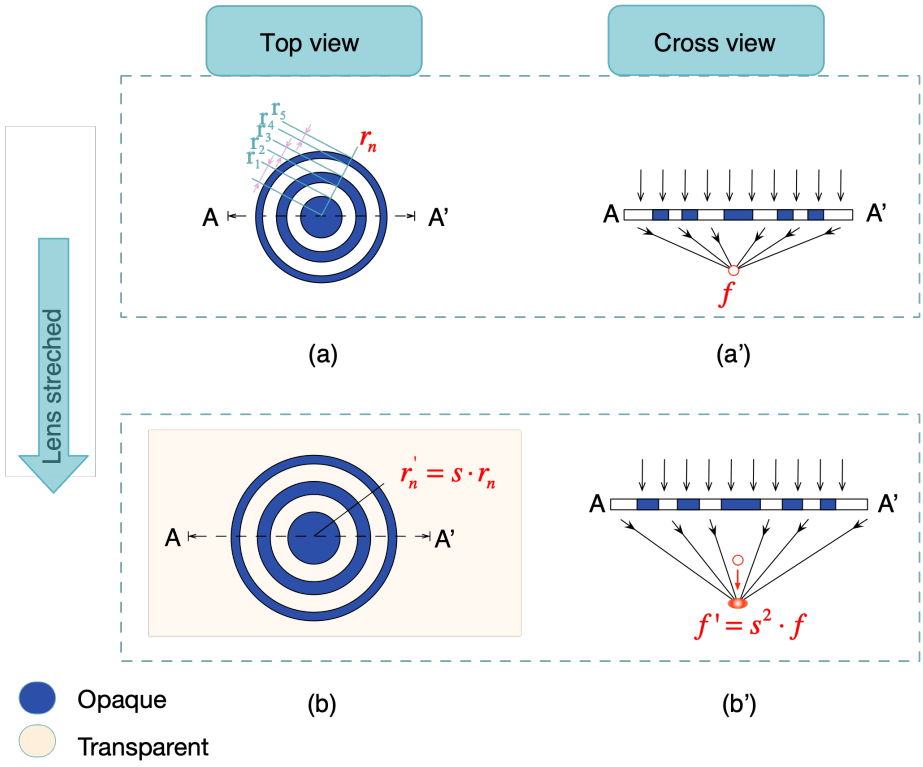

Figure 4.2: Schematic illustration of the tunable Fresnel lens. When stretching the flexible substrate radially by a factor of s from (a) to (b), the radius of the n_{th} zone increases from r_n to r_n' and the focal length changes from f to f' by a factor of by s^2.

The Fresnel lens configuration presented here utilizes CNT as the opaque areas, and PDMS as transparent material as well as stretchable substrate. A lens with a focal length of 7 mm is designed in this demonstration. According to Equation 4.1, with a wavelength of 635 nm, the diffractive lens pattern has an innermost radius r_1 of 66.7 μm, with 30 zones, as it provides a good focusing performance with a reliable fabrication process.

Higher zone numbers provide sharper focus by suppressing higher order focus. However, according to Equation 4.5, a high zone number results in a small z_n, meaning a smaller pitches for the high order zones, which may bring challenges to the CNT growth process. The CNT are 10 μm high as this height promises perfect optical absorption [18]. For this Fresnel optics with 7 mm focal length and 30 rings, the outer zone z_{15}(= r_{29}-r_{28}) has a CNT bundle pitch of 6.3 μm. A pitch smaller than that will make some CNT bundles distorted due to the high ratio of depth/pitch, thus we keep the ring number as 30. The PDMS layer has a thickness of 2 mm, making it easy to handle the slab during the fabrication, while keeping great stretchability of the lens.

To analyze the wave propagation and the focusing performance of the tuneable Fresnel lens, a 2D computation of the distribution after light propagates through the optics was made with Matlab R2015a (Mathworks, B.V.). Figure 4.3 compares the lens, designed for the wavelength to be λ=635 nm, before and after stretching the size by 10%.

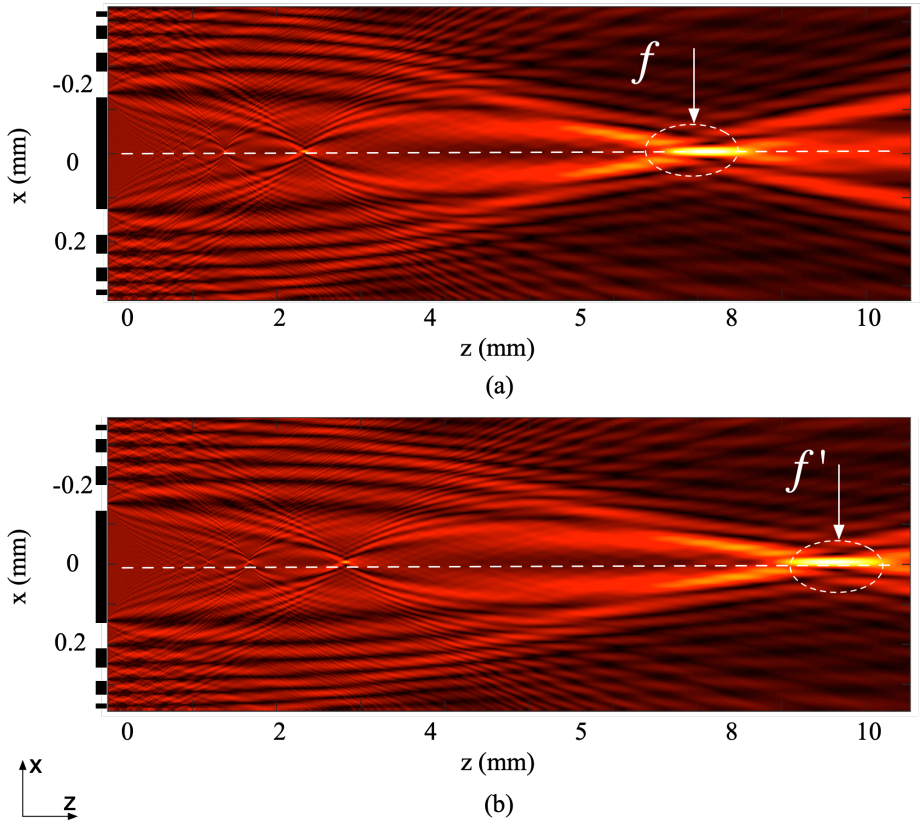

Figure 4.3: Computed wave propagation and focus change when the lens size is changed. (a) Light focuses at the focal point (7 mm) after it propagates through the lens; (b) When the lens is radially stretched by 10%, light redistributes and focuses at the new focal point at around 8.47 mm.

The analysis is based on the cross-section view along the symmetric center of the optics. The X-axis is along with the radial direction of the Fresnel zone plate, and the Z-axis is perpendicular to the Fresnel zone plate. Figure 4.3a shows the calculated focal point distance of the lens as indicated by the bright area outlined by the white ellipse. This indicates that the computed focal length is about 7 mm, which closely matches our initial calculation. Figure 4.3b shows the light redistribution and focus point at around 8.47 mm when the size of the Fresnel lens pattern is increased by 10%.

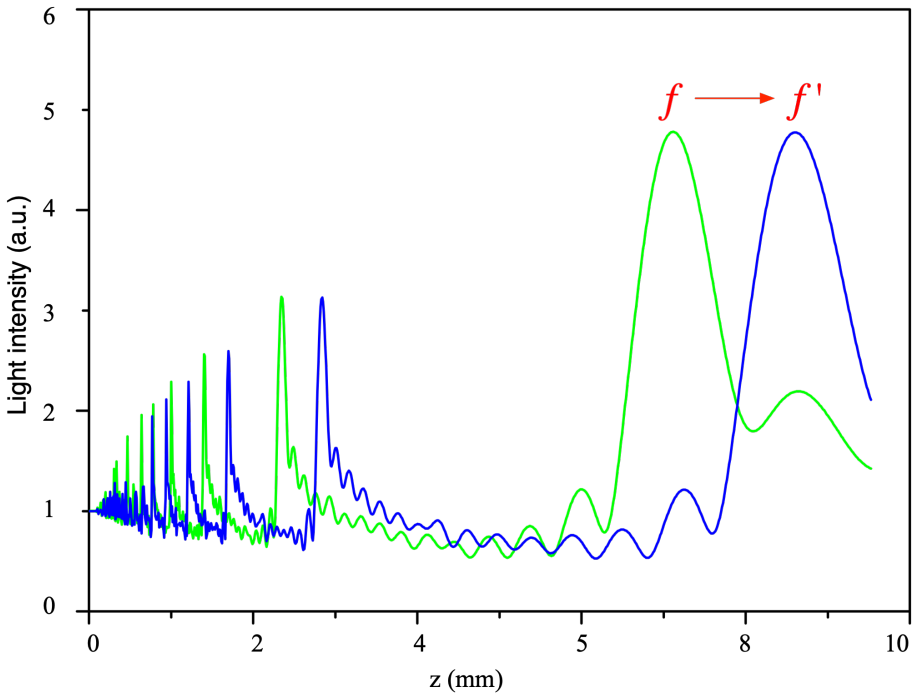

Figure 4.4: The light intensity along the z-axis of the focal plane, shows a clear shift of the peak intensity, indicating a focal point change from f indicated in green line to f' indicated in blue line.

Figure 4.4 depicts the contour for the light intensity value along the z-axis for the configuration in Figure 4.3a and Figure 4.3b. The light intensity reaches its peak at z=7 mm and 8.47 mm separately, indicating a focus difference of about 1.47 mm has been achieved. Given that the size increment is s=10%, while the others are constant, the focus difference agrees well with $\Delta f = (s^2 - 1) f$ as in the formula aforementioned. This demonstrates the exponential increase in focal distance.

4.3. FABRICATION

4.3.1. FABRICATION PROCESS

The fabrication of the optical device was performed in the cleanroom using a wafer level fabrication. The main steps are as follows, along with a schematic illustration depicted in Figure 4.5:

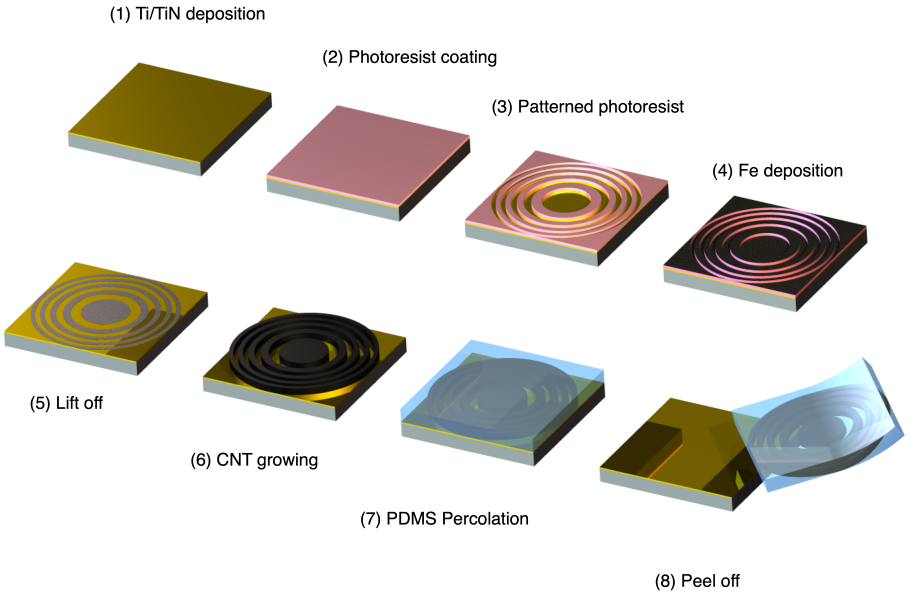

Figure 4.5: Schematic illustration of the microfabrication process of the stretchable Fresnel lens (not to scale). (1) Ti/TiN (10 nm/50 nm) was sputtered on a silicon wafer to prevent diffusion of the catalyst into the substrate, with silicon wafer as the substrate for growing CNT and following PDMS layer; (2) 1.4 μm photoresist was coated on the wafer and pretreated in the oven to increase the adhesion; (3) The photoresist was then exposed to transfer the optics pattern, which will be transferred into the pattern of the CNT; (4) Iron (5 nm) as catalyst was evaporated on the wafer; (5) After the catalyst evaporation, a lift-off process was executed to define the CNT growth regions; (6) Vertically aligned CNT bundles (10 μm in height) were grown at a temperature of 550 $^{\circ}C$ in 10 min; (7) PDMS was then mixed with the curing agent by a ratio of 10:1 and poured on the horizontal silicon wafer substrate with the defined CNT patterns. Followed by degassing at room temperature for 30 min and curing at 65 $^{\circ}C$ for 1 hour. The degassing process before curing is critical as to prevent trapping of gas bubbles inside the PDMS, which will break the balance of the optical propagation and thus deteriorate the optical performance; (8) The device is released by peeling off the PDMS layer together with the encapsulated CNT from the silicon substrate.

1. **Prepare for CNT growth**. In order to get a stable and uniform CNT growth condition, a catalyst layer is required to be deposited on the Silicon wafer. Before depositing the catalyst on the Silicon wafer, a Ti/TiN layer measures 10 nm/50 nm was deposited to prevent diffusion of the catalyst into the silicon substrate;

2. **Coat and bake of Photoresist layer**. To get a patterned CNT structure, we need to first transfer the pattern to the catalyst which grows the CNT. A lift-off process was used to get the pattern on the photoresist layer first. In this step, a 1.4 μm

photoresist layer was coated on the Silicon wafer as the medium for the pattern transfer;

3. **Expose and develop the photoresist**. The photoresist was then exposed, with the CNT patterns as the mask, followed by developing to get the inversed CNT patterns transferred on the cured photoresist;

4. **Deposit iron catalyst layer**. A 5 nm layer of Iron (Fe) as catalyst was evaporated. On the wafer where there's cured photoresist, the Fe will be deposited on top of the photoresist, and where there's no photoresist, the Fe will be deposited on the Ti/TiN layer directly;

5. **Lift-off to transfer the pattern on the catalyst**. A lift-off procedure was carried on in a beaker on a hotplate with NMP solvent constantly stirred at 65 °C and 250 rpm for 4 min. The Fe catalyst evaporated on the patterned photoresist will be removed along with the dissolved photoresist during this step, while the Fe evaporated directly on the Ti/TiN layer will stay, thus the pattern of the lens was then transferred to the catalyst layer;

6. **Grow CNT in the furnace**. Vertically aligned CNT bundles (10 μm in height) were then grown in an AIXTRON Black Magic chemical vapor deposition reactor, at a temperature of 550 °C in 10 min using conditions as specified in reference [23];

7. **Infiltrate PDMS in the CNT forest**. PDMS (Sylgard 184) was mixed with the curing agent by a ratio of 10:1 by weight, and then poured on the horizontal silicon wafer substrate with the defined CNT patterns. Followed by degassing at room temperature for 30 min and curing at 65 °C for 1 hour. The degassing process before curing is critical as to prevent trapping of air bubbles inside the PDMS, which will break the balance of the optical propagation and thus deteriorate the optical performance;

8. **Peel off the PDMS slab**. After curing the PDMS, the whole lens unit is formed thoroughly. The device is then released by peeling off the PDMS layer together with the encapsulated CNT from the silicon substrate.

4.3.2. FABRICATED DEVICES

A fabricated device containing 2x2 lens units, with each unit 6 x 6 mm^2 in size, is shown in Figure 4.6a. In each unit, the central part is the demonstrated lens part with the Fresnel zone rings. The surrounding of the lens pattern, visually shown as dark area, is purely CNT forest. The outer CNT area is to block the light passing through outside the lens area, so as to avoid the interference of the non-optics area, which is critical for investigating the optical property of the lens. The thickness of the lens unit is 2 mm, much higher than the CNT bundle height (10 μm). The thickness of the lens unit can vary from each application. In this case, we need to use the whole lens unit for testing with a mechanical stretching equipment, the thickness of 2 mm for the slab is the right size for better handling, and the stable for the elasticity. An optical microscopy image of a single lens is shown in Figure 4.6b. The darker parts are the CNT rings, while the brighter parts are PDMS area through which light can pass.

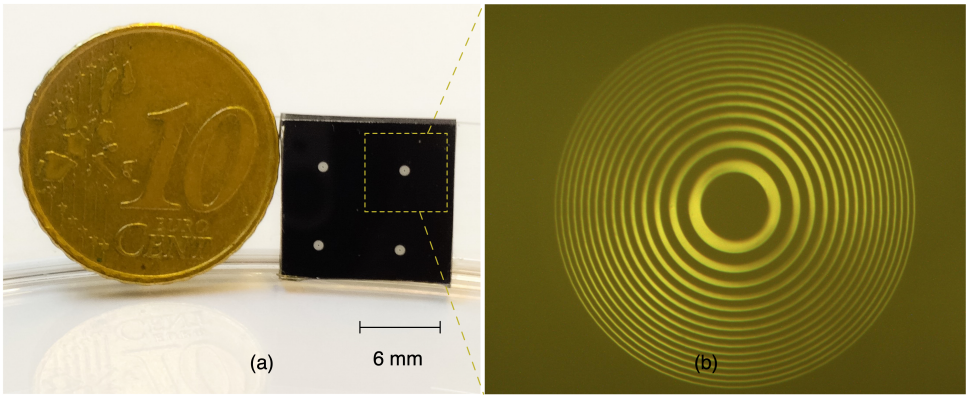

Figure 4.6: Fabricated device containing 2x2 lens units (f=7 mm), with each unit size 6x6 mm^2; (b) Optical microscope image of one lens pattern.

4.3.3. CNT QUALITY

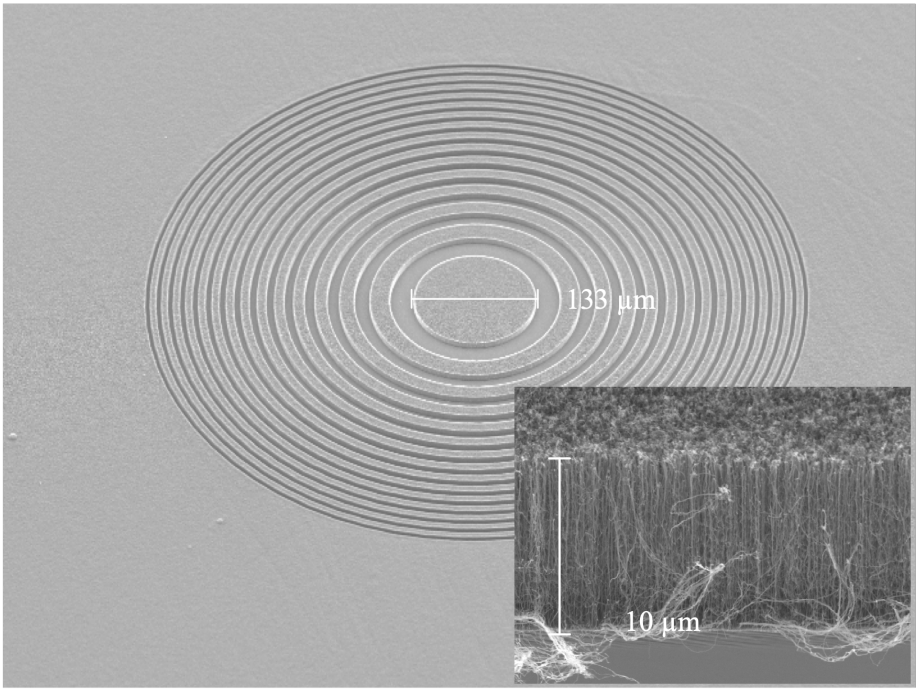

Figure 4.7: Tilted SEM image of the diffractive CNT pattern, the inset shows a close-up view of the vertically aligned CNT which are 10 μm in height (before PDMS percolation)

A scanning electron microscopy (SEM) image (tilted view) of a single lens unit, with

7 mm in focal length and an innermost zone diameter of 133 μm, before PDMS infiltration, is shown in Figure 4.7. The image shows that the flat surface of the CNT surface is obtained, promising for uniform optical properties of the CNT area, which is critical for the lens performance. More details of the CNT structure can be found in the close-up view. The fabricated CNT tubes are well aligned vertically. The tips of the CNT forest is uniform, with an equivalent height of 10 μm.

The binary Fresnel lens requires a high contrast on the opaque and transparent regions. As the opaque region in the optics, great quality CNT forest, specifically black and uniform CNT, is essential for fabricating the high quality lens. Maintaining the well defined pattern of CNT during the following process is also of great significance.

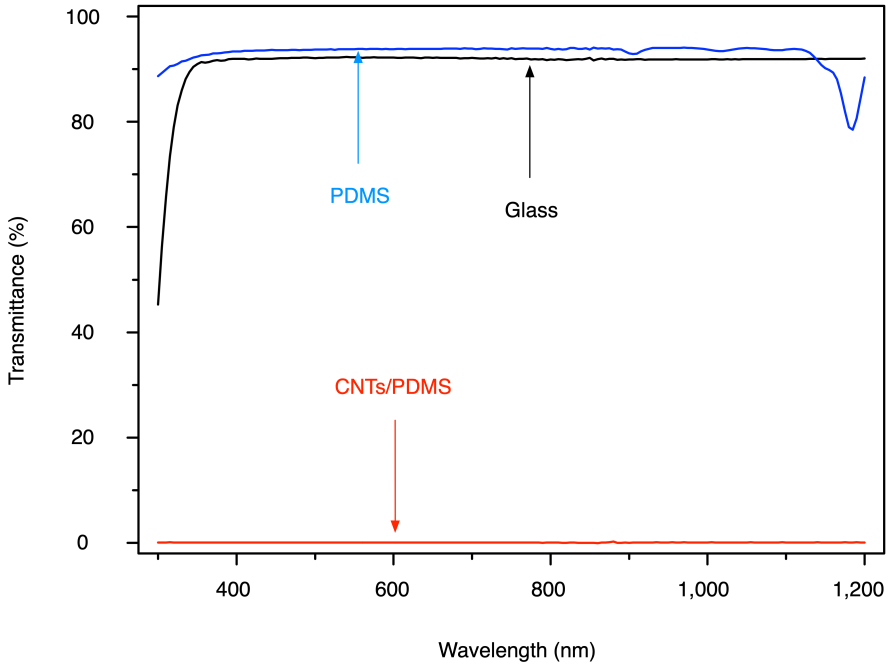

Figure 4.8: The measured transmittance of the transparent PDMS area and the opaque CNT/PDMS area, with glass as reference. The PDMS has a transmittance of 93.9%, higher than glass (91.8%), while the CNT/PDMS has transmittance of 0.06%.

The transmittance of the transparent PDMS area and the opaque CNT/PDMS area are measured with a spectrophotometer (PerkinElmer 950), as shown in Figure 4.8. The PDMS area has a transmittance of around 93.9% in the visible light spectrum, which is higher than glass (91.8%); while the CNT/PDMS area shows transmittance of 0.06% over the 300-1,200 nm spectral range. The great transparency of the PDMS area and the low transmittance of the CNT/PDMS composite area provide great contrast between the transparent areas and opaque areas, which in turn promise the Fresnel lens good focusing performance.

Figure 4.9 shows an SEM image of the CNT/PDMS composite to inspect the penetration of the polymer into the CNT forest. To get a better view of the percolation of polymeric PDMS, a higher CNT bundle (100 μm in height) is used. We observe that the CNTs inside the PDMS are still well aligned after the PDMS percolation, thus maintaining the CNT patterns and the excellent optical absorption properties. Furthermore, the thorough penetration of PDMS promises good flexibility for the composite, which is important for the tuneability of the lens. The transparency of the PDMS material and the absorption of the opaque area of the patterned CNT are fundamental to the optical performance of the Fresnel lens.

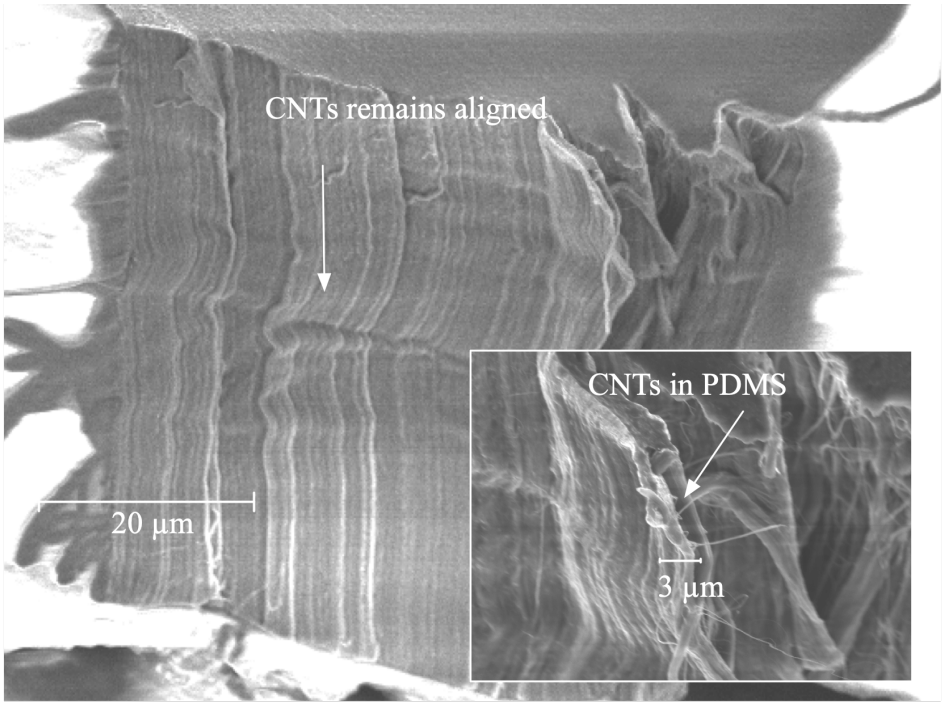

Figure 4.9: SEM image of the CNT with the PDMS percolated thoroughly into the CNT bundles. The CNT bundles remain aligned in the PDMS, indicated by the vertically aligned strips in the SEM image. The close-up view shows CNT bundle in the PDMS, in contrast to the CNT floss which was exposed after tearing up the sample.

4.4. MEASUREMENT SETUP

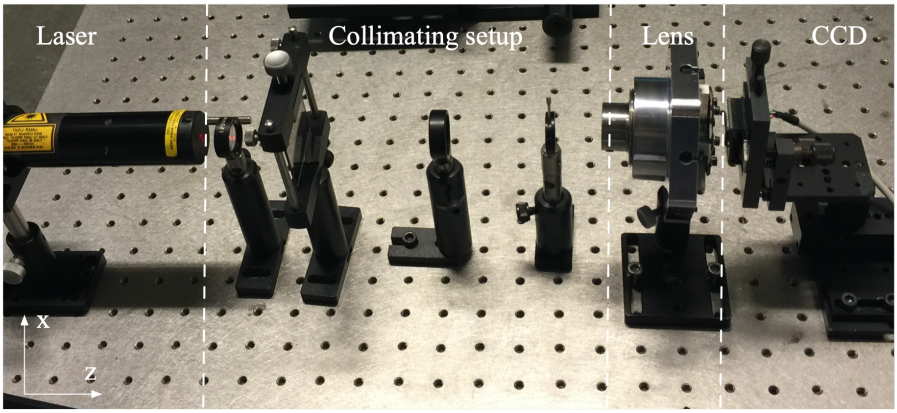

(a)

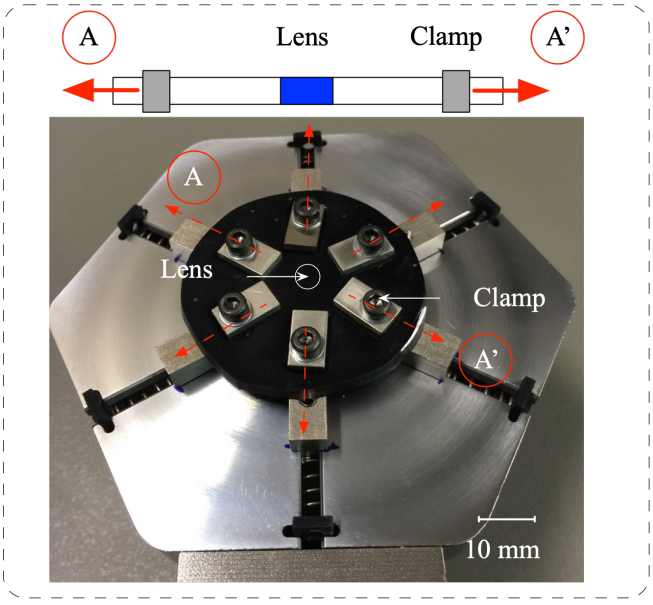

(b)

Figure 4.10: (a) The experimental setup used for the lens characterization. A 635 nm laser is used to illuminate the Fresnel lens, which is adjusted by two convex lenses, a filter and a diaphragm to improve collimation. A CCD camera captures the image of the focal region of the lens. By moving the camera along the z-axis, the focus intensity distribution can be detected; (b) The lens is maintained on a customized sample holder with six clamps for holding and stretching the lens in the radial direction.

THE measurement setup used to characterize the stretchable Fresnel lens is shown in Figure 4.10a. The lens is clamped on a customized holder and is illuminated by a 635 nm laser, which is adjusted by two convex lenses, a filter and a diaphragm to improve the collimation. The axis of the movement is set up based on the Fresnel lens. The vertical direction in space, which is also the radial direction of the lens is denoted as the x-axis, while the horizontal direction in space, which is the direction perpendicular to the lens surface, is denoted as the z-axis. With the other components fixed, by moving the charge-coupled device (CCD) camera along the z-axis to capture the diffraction pattern spatially, diffraction pattern shall change with the distance from the CCD camera to the converging lens as aforementioned in Figure 4.3. The holder used to stretch the lens in the radial direction is shown in Figure 4.10b. Six symmetrically distributed clamps are maintaining the lens on the holder. Each clamp can be adjusted by the same amount in increments of 0.289 mm in the radial direction. Considering the full sample is 30 mm in diameter, the radius of the lens pattern will increase by 1.9% with each increment. Diffraction patterns were captured by a CCD camera with two additional convex lenses after the light propagates through the Fresnel lens.

4.5. OPTICAL PERFORMANCE

4.5.1. DIFFRACTIVE PATTERN ANALYSIS

Fifty shots of diffractive patterns from z= 5.6 mm to 8.05 mm are captured with a CCD camera, with a step-size of Δz= 0.05 mm for each image. The diffraction patterns are normalized (white represents the maximum light intensity and black is the off state of the camera). The intensity profiles from the x-axis (y=0) of each image are then extracted and reconstructed to an intensity map with Matlab R2015a (Mathworks, B.V.), as shown in Figure 4.13. The focus position with astigmatism can be determined when the two axes of the cross are completely symmetric [24]. The focal length of the lens is measured by recording the distance from the lens plate to the focal point.

4.5.2. STATISTICAL ANALYSIS

The focus change measurement under stretching was repeated on the same lens for three times. The focal point changes of the lens were recorded and analyzed. Data are expressed as the mean ± standard deviation ($\mu \pm \sigma$), as indicated in corresponding Figure 4.13.

4.5.3. DIFFRACTION PATTERNS

The light distribution of the lens is measured near the focal plane (z= 7 mm). A CCD camera is employed to capture the diffraction images along the z-axis. With the collected images an intensity distribution was reconstructed. The captured pictures as shown in Figures 4.11a-f, are indicated as the positions A-F (with z= 5.6 mm, 6 mm, 6.5 mm, 7 mm, 7.5 mm, 8 mm separately) in Figure 4.11h.

Figure 4.11a shows that at position A, a ring is obtained. The diffraction pattern at position B becomes smaller and brighter, and a light spot started to form in the center (Figure 4.11b). The light spot becomes brighter and smaller when moving to position C (Figure 4.11c). A focused light spot is then observed at position D (Figure 4.11d), which

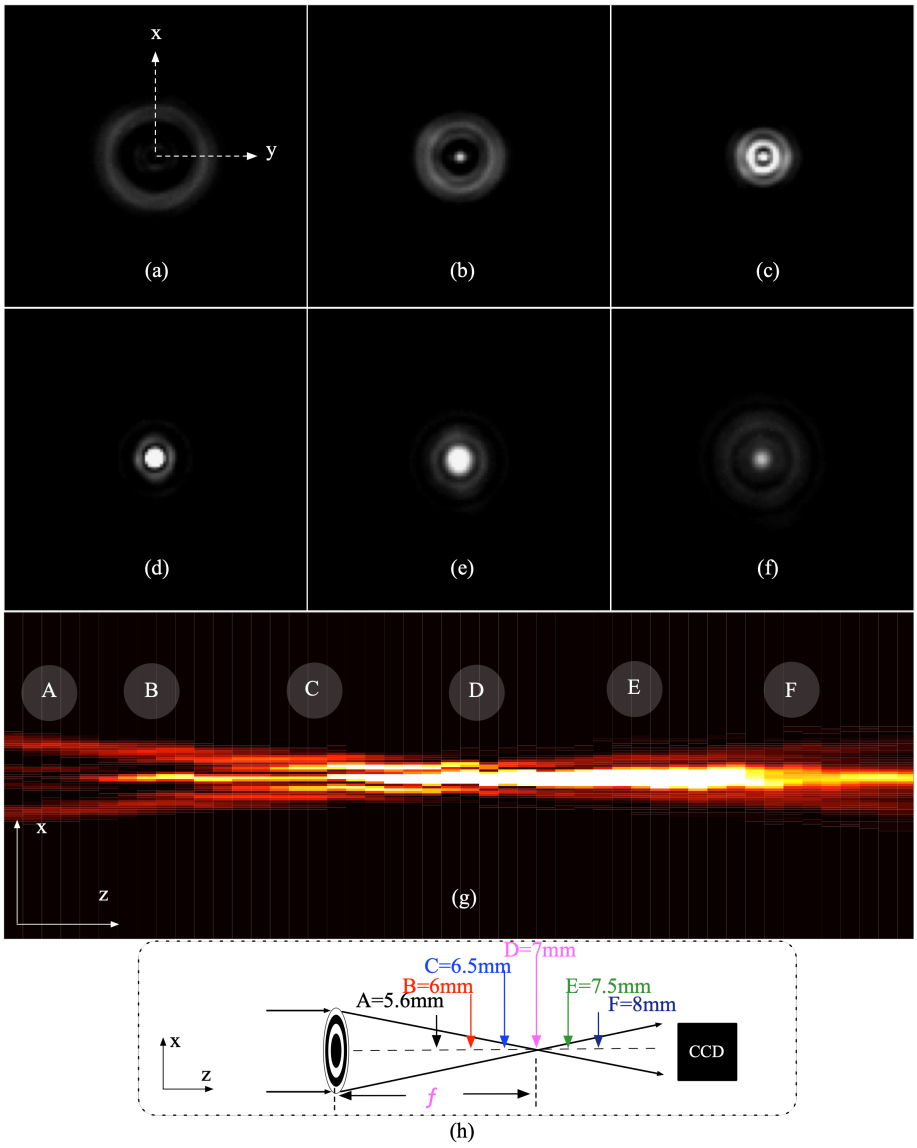

Figure 4.11: Diffraction patterns along the z-axis near the focal plane captured by a CCD camera. (a) A ring is observed at position A; (b) Diffraction pattern size becomes smaller and a bright spot appears in the center at position B; (c) The light spot becomes smaller and brighter at C; (d) An clear light spot is formed at D, which indicates the focal plane; (e, f) moving further towards position E and F the pattern becomes dimmer, wider and it eventually defocuses; (g) The reconstructed intensity distribution from z= 5.6 mm to 8.05 mm are shown; The captured pictures from (a-f) are indicated as the positions A-F as shown in (h). The intensity distribution can be compared with the computed intensity reported in Figure 4.3a in the regime of z= 5.6 mm to 8.05 mm.

indicates the position the focal plane. Beyond the focal plane, the light spot becomes dimmer and wider. Defocused patterns are observed at E (Figure 4.11e) and F (Figure 4.11f), with the light spot getting smaller. The overview of the intensity distribution from z=5.6 mm to z= 8.05 mm is shown with a reconstructed intensity map, by collecting 50 distributed images of the diffraction patterns along the z-axis, with an increment of 0.05 mm. The diffraction patterns are normalized (white represents the maximum light intensity and black is the off state of the camera). The intensity profiles from the x-axis (y=0) of each image were then extracted and reconstructed to an intensity map, as shown in Figure 4.11g. The intensity along z-axis starts with low intensity in the center at A, and forms a light spot at around B and C, after it reaches a peak at D, which also indicates the focal point, it then becomes wider at around E and defocused at around F. The intensity distribution can be compared with the computed intensity reported in Figure 4.3a. The changing diffraction patterns were measured to demonstrate the focal length changes when stretching the Fresnel lens. As the lens is stretched in the radial direction with increments of 1.9%, a theoretical increase of 3.88% of the focal length f is expected.

4.5.4. DIFFRACTION PATTERNS CAPTURED FROM THE STRECHTED LENS

Figure 4.12 shows diffraction patterns captured at four positions along the z-axis, indicated by A-D in the inset figure at different amounts of applied strain. The diffraction patterns of the lens at a relaxed state are in accordance with Figure 4.11, and the bright light spot was found at 7 mm in Figure 4.12, which shows the initial focus point. After stretching the lens along the radial direction by 1.9%, clear diffraction pattern changes can be found at the same positions, even though the focal point stays at around 7 mm. As applied strain goes up 3.8%, the diffraction patterns experience greater changes, and the focused pattern has shifted from 7 mm to around 7.3 mm, which indicates the focus point increased by 0.3 mm due to the stretch. Astigmatism was noticed during stretching. The focus spot with astigmatism can be determined when the two axes of the cross are completely symmetric as described in reference [24].

The focus change performance of the lens is shown in Figure 4.13, to compare the measured focal changes with the expected changes. The measurement data are presented as the mean ± standard deviation ($\mu \pm \sigma$), while the mean is the average of the three times measurement, and the error bars indicate the standard deviation (σ). The focal length is measured by recording the distance from the lens plate to the focus point, while a strain is applied to the sample, increasing from 1.9% to 15.2% with stepped increments of 1.9%. The focal length increases with the applied strain, which agrees with the computational simulation. For instance, a strain of 11.4%, the focal point shifts from 7 mm to 8.7 mm, indicating that a change of 24% is achieved. A small σ of around 0.1 mm is obtained when the strain ranges from 1.9% to 11.4%. However, when the strain increases to 13.3% and 15.2%, the σ becomes larger than 0.29 mm, meanwhile the diffraction patterns get distorted and the focal points from the captured images are less clear. This indicates the limit of the lens with respect to the maximum amount of strain has been reached, thus no higher stretchment was applied on the lens.

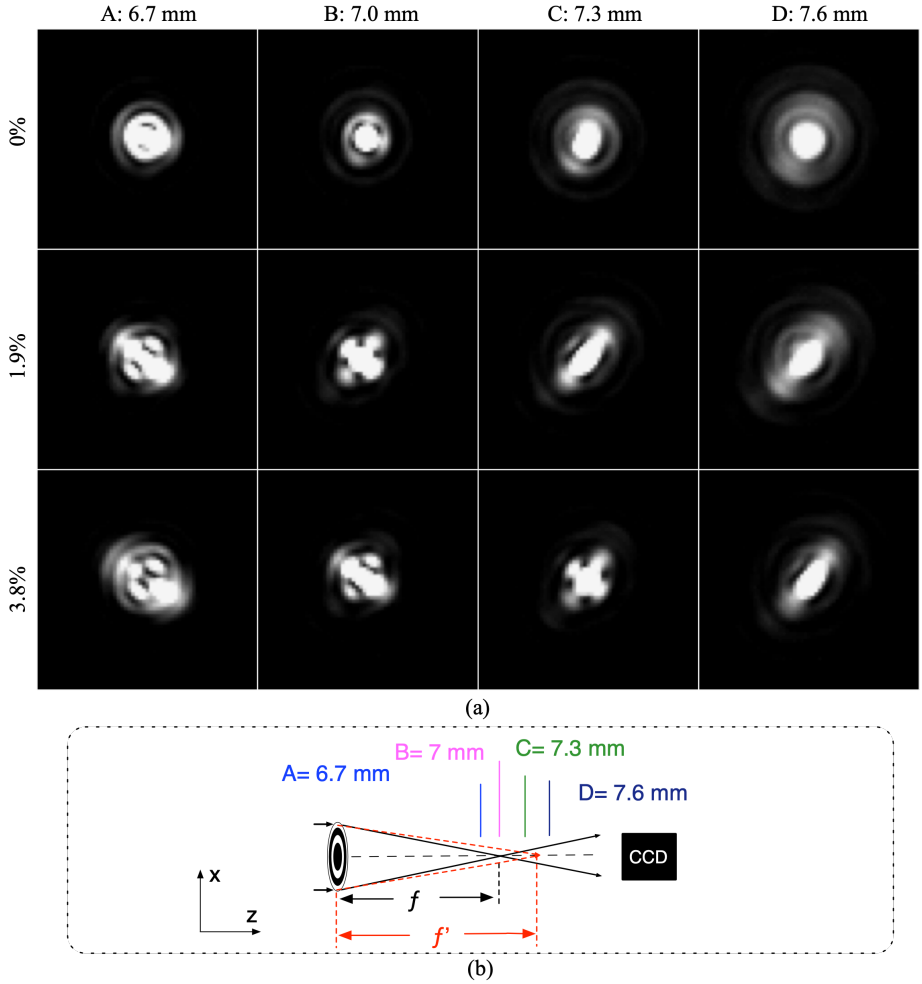

Figure 4.12: (a) Diffraction patterns captured with a CCD camera at four different positions along the z-axis, demonstrating the effect of stretching the lens. Bright light spot appears at 7 mm in the relaxed state of the lens; When applied with a small strain of 1.9% on the lens we observe changes in the diffraction patterns which can be identified as astigmatism; When the strain increases to 3.8%, we observe a focused light spot shift from 7 mm at relaxed state to around 7.3 mm. This indicates focus change has been realized due to the stretch; (b) The aforementioned four positions are indicated as A-D.

4.6. DISCUSSION

FIGURE 4.13 shows that a focus change can be achieved as lens size increases due to stretching. The measured focus change follows the same trend as the prediction made by Equation 4.1. In addition, the results agree with the computed simulation of the focus change before and after stretching (Figure 4.4). This validates the proposed

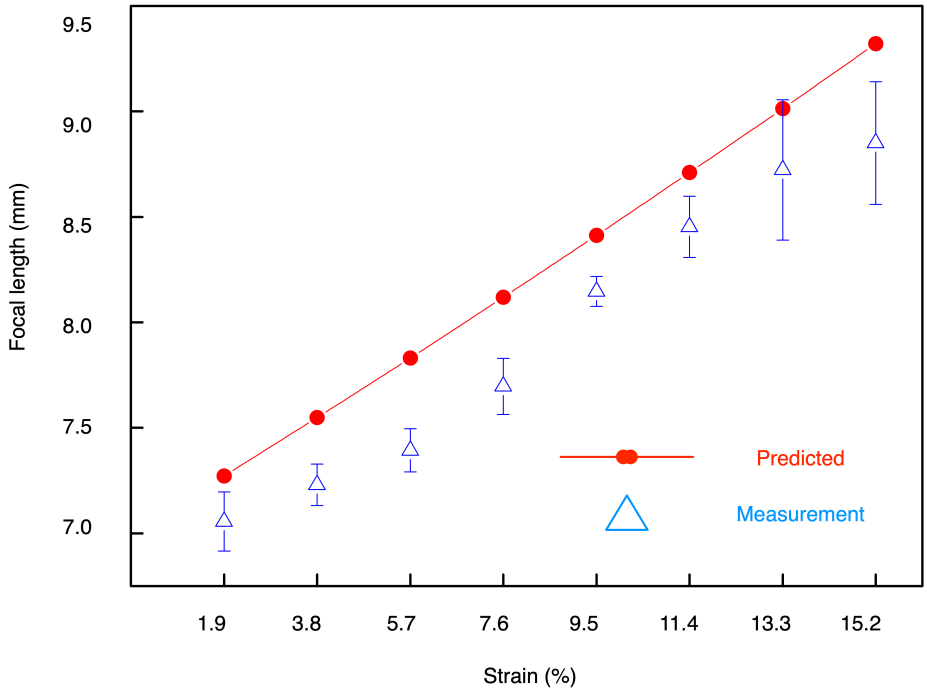

Figure 4.13: Measurement of the increase in focal length as the lens is stretched radially by the clamps on the holder. The measured focus change follows the predicted focus change. Straining the lens from 1.9% to 11.4%, causes the focal point to shift from 7 mm to 8.7 mm. The diffraction pattern becomes more distorted when strain is increased further to 13.3% and 15.2%, which is near the maximum extension of the lens. The data are presented as the mean ± standard deviation.

concept for a tuneable Fresnel lens through radial stretching.

A mismatch of the focus change between the theoretical calculation and the measurement was observed in Figure 4.13. A possible explanation is the somewhat non-linear deformation of the elastomeric PDMS substrate.

During the stretching of the lens, the strain distribution in radial direction is not linear. Simulation of the lens deformation is reported in Figure 4.14. Finite element analysis software (COMSOL Multiphysics 5.1) was used to analyze the deformation of the polymeric substrate. *Solid Mechanics model under Structural Mechanics* is used for the calculation. The material of the lens model was set to be PDMS. The effect of the CNT is not included because the thickness of PDMS (2 mm) is much higher than the height of CNT (10 μm). A hyper-elastic material model was used to describe non-linear material behavior under moderate strains accurately. The radial symmetric lens model has a radius of 15 mm and a thickness of 2 mm. A symmetry boundary constraint was added to the centre of the lens, while the prescribed displacement was enforced on the peripheral boundary. The displacement range increased from 0 to 2.32 mm with a step size of 0.0289 mm.

The solid lines show the non-linear deformation of the elastomeric PDMS when different strain is exerted, while the dashed line shows a perfect linear distribution of the deformation. For example, as depicted in the close-up view, for a strain of 15.2%, the deformation in the lens area is less than the predicted value, resulting in a smaller value of the zone radius for the diffractive lens, hence smaller focus change. This explains why the measured focal change is less than expected.

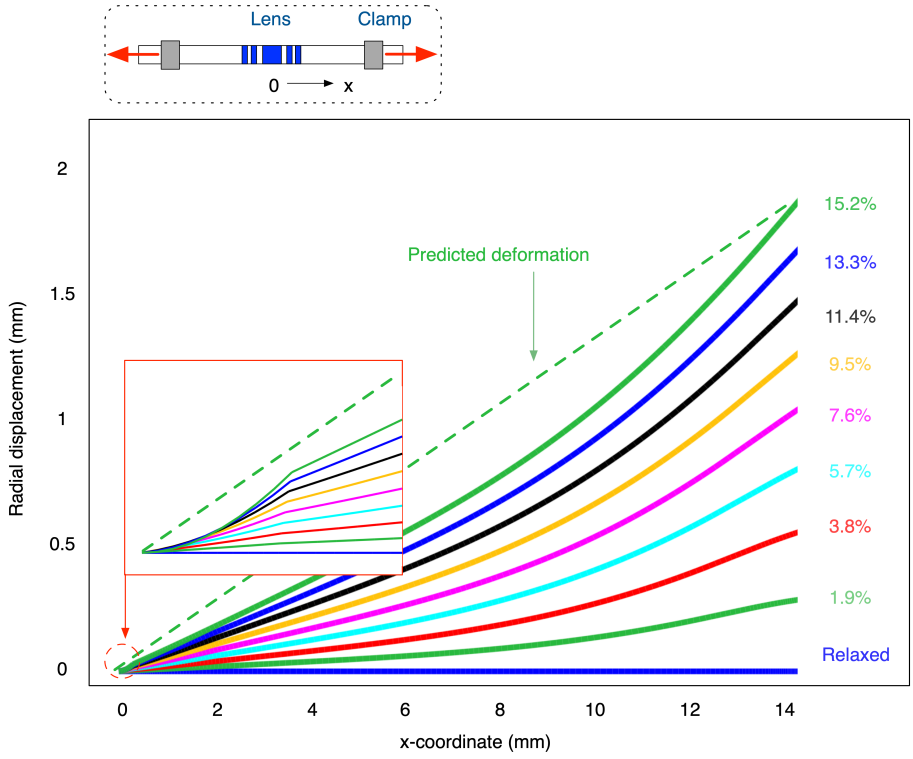

Figure 4.14: Simulation of the lens deformation in radial direction when the lens is stretched. The non-linear deformation of the polymeric substrate makes the deformation of the lens area near the center smaller than the linear prediction. The close-up view (inset) shows that in the center area, a clear difference between the substrate deformation and the predicted value is experienced by the lens.

A σ of 0.14 mm is observed at the first stretching for small strains of 1.9% in Figure 4.13. Clamping the lens on the holder generates some initial stress near the six clamps which causes some non-uniform deformation of the lens. While stretching the lens, the initial stress of the composite will be either compensated or covered by the stretching, which is unpredictable due to the limited control in the loading of the sample in the holder. This accounts for the large σ for the first stretching. When the stretching continues, the strain from the polymer deformation is dominant and the focal length changes with stretching accordingly. This behavior is reflected in the data reported in Figure 4.13 where a clear focal change is shown when strain goes from 3.8% to 11.4%, and with low

σ of around 0.1 mm.

Astigmatism is observed during the stretching, as shown by the elliptic patterns in Figure 4.12 . This is due to the somewhat non-uniform clamping of the lens in the sample holder. The diffractive patterns are very sensitive to the uniformity of the Fresnel lens. The σ of our measurement is increasing for larger applied strains because imperfections in uniformity are increased for larger strains. Secondly, the sample is unloaded, and reloaded after each experiment so the sample can relax back towards its original configuration without being clamped. We assume that the re-positioning of the lens, in combination with the somewhat non-uniform clamping contributes to the σ to the data. We recommend integrating an actuator which can provide a uniform radial deformation of the lens (similar to a diaphragm), which doesn't require mechanical clamps.

4.7. CONCLUSION

THE proposed Fresnel lens formed by embedding vertically aligned CNT bundles in a PDMS layer, utilizes the optical absorption properties of the CNT and the transparency and flexibility of the PDMS. Diffraction patterns of the lens were measured by a CCD camera to characterize the Fresnel lens. By stretching the lens radially, clear diffraction pattern changes were observed, which were in accordance with the simulation results. A maximum focus change of about 24% can be realized by stretching the lens radially 11.4%. Some imperfections of the clamping mechanism employed to stretch the lens introduced astigmatism. However, we think this problem can be solved by integrating a circular in-plane actuator, which can provide a more uniform deformation of the lens. The focus change obtained from the stretching agrees with the theoretical calculation, making it possible to predict the focus changing performance, which can assist in the design of stretchable Fresnel lenses. We demonstrate a straightforward approach for microfabrication of a tuneable Fresnel lens, making it compatible with the miniaturization and suitable for mass fabrication. Furthermore, the good optical performance of the tuneable diffractive lens indicates great potential in holography. Finally, the biocompatibility of the polymeric composites makes it promising for integration in biological applications in such as electronic eyes.

In this chapter we report on the achieved results using a lens with a focal length of 7 mm for demonstration, with the same concept and fabrication process, we fabricated lenses with focal lengths ranging from 100 μm to 20 mm, so as to match the specific application demands. For instance, a focal length ranging from 5 μm to 8.5 mm can be used in microscopy to investigate the fluorescence signal [25], [26]. Lens arrays with focal length ranging from 2 mm to 20 mm can also be used for compound eye applications and point of care devices [20], [27], [28]. With the same configuration, even larger focal lengths can be applicable.

With the function of controllable focal lengths, this configuration is also applicable for the multi-focus contact lens application. Due to that the opaque area in the binary amplitude Fresnel lens will cause the loss of incoming light. A trade-off between the multi focus function and incoming light must be considered.

The fabrication of the lens (array) is fast and reliable, of which the key process is the growth of patterned CNTs. This can be realized in wafer scale and thus large volume for mass manufacture.

The flat optics can be optical components on silicon based electronics for making miniaturized photonic chips in various applications, such as in integrated optics, optical interconnects, beam focusing, maskless lithography systems, deflecting and collimating tasks in optical sensor systems, optical computers, optical data transfer and optical communication is possible.

REFERENCES

[1] X. Li, L. Wei, S. Vollebregt, R. Poelma, Y. Shen, J. Wei, P. Urbach, P. Sarro, and G. Zhang, *Tunable binary Fresnel lens based on stretchable PDMS/CNT composite,* in *2015 Transducers - 2015 18th International Conference on Solid-State Sensors, Actuators and Microsystems (TRANSDUCERS)* (IEEE, 2015) pp. 2041–2044.

[2] X. Li, L. Wei, R. H. Poelma, S. Vollebregt, J. Wei, H. P. Urbach, P. M. Sarro, and G. Q. Zhang, *Stretchable Binary Fresnel Lens for Focus Tuning,* Scientific Reports **6**, 25348 (2016).

[3] J. Happich, *Stretchable Polymer Optics Embed Carbon Nanotubes for Better Focus,* (2016), accessed: 23-Feb-2020.

[4] H. Zappe, *Fundamentals of Micro-Optics* (Cambridge University Press, 2010) p. 646.

[5] N. Chronis, G. Liu, K.-H. Jeong, and L. Lee, *Tunable liquid-filled microlens array integrated with microfluidic network,* Optics Express **11**, 2370 (2003).

[6] F. Krogmann, W. Mönch, and H. Zappe, *A MEMS-based variable micro-lens system,* Journal of Optics A: Pure and Applied Optics **8**, S330 (2006).

[7] K. Mishra, C. Murade, B. Carreel, I. Roghair, J. M. Oh, G. Manukyan, D. Van Den Ende, and F. Mugele, *Optofluidic lens with tunable focal length and asphericity,* Scientific Reports **4**, 1 (2014).

[8] L. Liu, S. Pal, and H. Xie, *MEMS mirrors based on curved concentric electrothermal actuators with very small lateral shift and tilt,* in *2011 16th International Solid-State Sensors, Actuators and Microsystems Conference* (IEEE, 2011) pp. 2522–2525.

[9] X. LI, J. Wei, T. Ma, C. Yuan, L. Sarro, and K. Zhang, *Compact tunable optics for dynamic lighting,* in *Classical Optics 2014*, Vol. 1 (OSA, Washington, D.C., 2014) p. JTu5A.35.

[10] R. Rajasekharan, H. Butt, Q. Dai, T. D. Wilkinson, and G. a. J. Amaratunga, *Can nanotubes make a lens array?* Advanced Materials **24**, OP170 (2012).

[11] Y. Montelongo, H. Butt, T. Butler, T. D. Wilkinson, and G. a. J. Amaratunga, *Computer generated holograms for carbon nanotube arrays.* Nanoscale **5**, 4217 (2013).

[12] M. Hain, W. von Spiegel, M. Schmiedchen, T. Tschudi, and B. Javidi, *3D integral imaging using diffractive Fresnel lens arrays,* Optics Express **13**, 315 (2005).

[13] F. Yong-Qi, N. Kok Ann Bryan, and O. Shing, *Diffractive optical elements with continuous relief fabricated by focused ion beam for monomode fiber coupling.* Optics express **7**, 141 (2000).

[14] L. Lindvold, *Commercial aspects of diffractive optics,* Dops Nyt , 62 (2001).

[15] E. T. F. Rogers, J. Lindberg, T. Roy, S. Savo, J. E. Chad, M. R. Dennis, and N. I. Zheludev, *A super-oscillatory lens optical microscope for subwavelength imaging,* Nature Materials **11**, 432 (2012).

[16] C. Chang and A. Sakdinawat, *Ultra-high aspect ratio high-resolution nanofabrication for hard X-ray diffractive optics.* Nature communications **5**, 4243 (2014).

[17] X.-T. Kong, A. a. Khan, P. R. Kidambi, S. Deng, A. K. Yetisen, B. Dlubak, P. Hiralal, Y. Montelongo, J. Bowen, S. Xavier, K. Jiang, G. a. J. Amaratunga, S. Hofmann, T. D. Wilkinson, Q. Dai, and H. Butt, *Graphene-Based Ultrathin Flat Lenses,* ACS Photonics , 150120150220004 (2015).

[18] Z.-P. Yang, L. Ci, J. A. Bur, S.-Y. Lin, and P. M. Ajayan, *Experimental Observation of an Extremely Dark Material Made By a Low-Density Nanotube Array,* Nano Letters **8**, 446 (2008).

[19] R. H. Poelma, B. Morana, S. Vollebregt, E. Schlangen, H. W. van Zeijl, X. Fan, and G. Q. Zhang, *Tailoring the Mechanical Properties of High-Aspect-Ratio Carbon Nanotube Arrays using Amorphous Silicon Carbide Coatings,* Advanced Functional Materials **24**, 5737 (2014).

[20] M. J. Moghimi, J. Fernandes, A. Kanhere, and H. Jiang, *Micro-Fresnel-Zone-Plate Array on Flexible Substrate for Large Field-of-View and Focus Scanning,* Scientific Reports **5**, 15861 (2015).

[21] X. Li, Z. Wei, D. Zhao, H. Yan, Z. Liang, and Z. Li, *A flow-through electroporation chip integrated with viable cell sorting based on dielectrophoresis,* in *2012 IEEE 25th International Conference on Micro Electro Mechanical Systems (MEMS)*, February (IEEE, Paris, 2012) pp. 993–996.

[22] K. Rastani, a. Marrakchi, S. F. Habiby, W. M. Hubbard, H. Gilchrist, and R. E. Nahory, *Binary phase Fresnel lenses for generation of two-dimensional beam arrays.* Applied optics **30**, 1347 (1991).

[23] S. Vollebregt, F. D. Tichelaar, H. Schellevis, C. I. M. Beenakker, and R. Ishihara, *Carbon nanotube vertical interconnects fabricated at temperatures as low as 350 °c,* Carbon **71**, 249 (2014).

[24] I. Morison, *Star testing a telescope,* Popular Astronomy **January-Ma**, 12 (2009).

[25] P. Davidovits and M. D. Egger, *Scanning laser microscope for biological investigations.* Applied optics **10**, 1615 (1971).

[26] E. Schonbrun, W. N. Ye, and K. B. Crozier, *Scanning microscopy using a short-focal-length Fresnel zone plate*. Optics letters **34**, 2228 (2009).

[27] P. Vilmi, S. Varjo, R. Sliz, J. Hannuksela, and T. Fabritius, *Disposable optics for microscopy diagnostics*, Scientific Reports **5**, 16957 (2015).

[28] Y. M. Song, Y. Xie, V. Malyarchuk, J. Xiao, I. Jung, K.-J. Choi, Z. Liu, H. Park, C. Lu, R.-H. Kim, R. Li, K. B. Crozier, Y. Huang, and J. A. Rogers, *Digital cameras with designs inspired by the arthropod eye*, Nature **497**, 95 (2013).

5

CNT/PDMS FOR FLEXIBLE INTERPOSER APPLICATION

Parts of this chapter have been published in Yingjie Shen's master thesis **2015** [1].

In the previous chapter, the composite material which combines vertically aligned carbon nanotubes(CNT) and polydimethylsiloxane (PDMS) was used in the flat lens due to its unique optical properties and excellent stretchability. In this chapter, the electrical properties of the composite for potential interposer applications are investigated in this chapter.

5.1. INTRODUCTION

AN interposer is the intermediate tier between the chips and the packaging substrate, as one of the essential units, it benefits the packaging with heterogeneous integration and reduction in form factor [2]. A schematic illustration of an interposer is depicted in Figure 5.1. A conventional interposer is composed of conductive vias, which are embedded in the supporting substrate, and conductive contacts between interposer and chips. The interposer works as the support medium for the chip to be mounted. Meanwhile, the vias in the interposer connect the chips and distribute the connections into the packaging substrate. The interposer represents a convergence of the integration disciplines, optimizing the performance of the chips in the package.

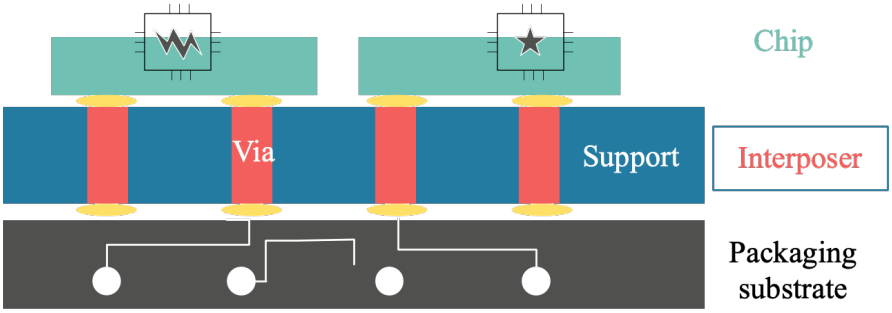

Figure 5.1: Schematic illustration of interposer. As the interface, interposer supports the chip to be mounted, meanwhile it connects the chips and spread the connections into the packaging substrate. The sizes of the components are not to scale.

An enormous amount of applications of flexible electronics have been demonstrated [3]. For instance, Lian et al. have designed a flexible organic light-emitting diodes on a Polyethylene terephthalate (PET) substrate for antimicrobial photodynamic therapy[4], while an electrically programmable hydrogel was proposed by Yu et al. which could be working as actuators in soft robotics[2], Jin et al. has proposed a stretchable and bio-implantable acoustic device using liquid metal coil on PDMS substrate[5], Lipomi et al. have designed skin like pressure and strain sensors with the elastic films[6]. Most of the studies have demonstrated the high performance of the dies, yet till now there's no perfect coverage on packaging the dies with a matching flexible printed circuit board (PCB) which is essential for devices to be commercially available[7].

In the application of flexible electronics, to achieve high performance for the pack-

aging, the interposers are required to have a fine interconnect pitch to match the ever increasing device density and shrinking chip feature sizes. In addition to that, the application of flexible electronics requires the support material to match the flexibility with the device[8].

Several polymer materials have been proposed as candidates for interposers, such as PDMS[9], parylene[10]. Both polymers are popular structure materials for flexible electronics, thanks to their great stretchability and biocompatibility. Thus, both materials are functioning well as the supporting material for flexible interposer. With reference to the interconnect within the interposer, till now, the mainstream solution is to use rigid metal as the conductive vias or electrodes [11, 12]. The metal vias work well electrically thanks to the low resistance, reliability and matured fabrication, however, the rigid metal vias mechanically doesn't match well with the flexible substrate, especially when the whole device is bent or stretched.

An alternative to the rigid metal is to use CNT dispersed into the polymer to form a conductive 3D structure[13]. The CNT enhanced polymer has demonstrated a conductivity of 102 S/cm and can achieve consistent conductance with up to 100% stretchability, however, the dispersion of the CNT tubes makes it hard to control the quality, especially the CNT bundles dispersed in the PDMS to make flexible electrodes. Besides, the inhomogeneity in terms of CNT length, lack of high purity and good homogeneity limit the device performance. The surfactant used to disperse CNTs is difficult to remove which can act as a barrier for electronics conduction [14].

Vertically aligned CNT has been proved to be a potential candidate as interconnect with standard fabrication and quality control, the theoretical electric properties of CNT match well with the purpose of interconnecting [15], while the Young's modulus of the vertically aligned CNT is three orders less than the rigid materials such as Cu and Au[16]. In order to use the vertically aligned CNT in the interposer, the high aspect ratio of the CNT narrowed down the options of polymers. While the CNTs can go up to hundreds of μm or even mm, polyimide can hardly reach to this height, on the other hand, the fabrication of parylene is based on evaporation, the parylene particles can only deposit on the top of the CNTs instead of penetrating into the CNT bundles. PDMS and vertically aligned carbon nanotubes could be a good configuration for flexible interposer to meet increasing demands on flexible interposer [1].

In this chapter, a CNT/PDMS for potential flexible interposer applications is proposed. The configuration is based on the PDMS as support material, while the embedded vertically aligned CNT bundles serve as conducting vias with its electrical conductivity.

5.2. DESIGN PRINCIPLE

THE proposed flexible interposer consists of the PDMS as a substrate, with the CNT/PDMS as an anisotropic electrical connection between the layers, as shown in Figure 5.2. The through-hole wires are vertically aligned CNT bundles embedded in the polymer substrate, which promises it to inherit the mechanical property of the substrate while integrating the anisotropic electrical conductivity into the wires. The metal pads are the medium to connect the CNT bundles with the wires for packaging. The CNT bundles are of different diameters, but all in the same height of 100 μm for demonstration purpose.

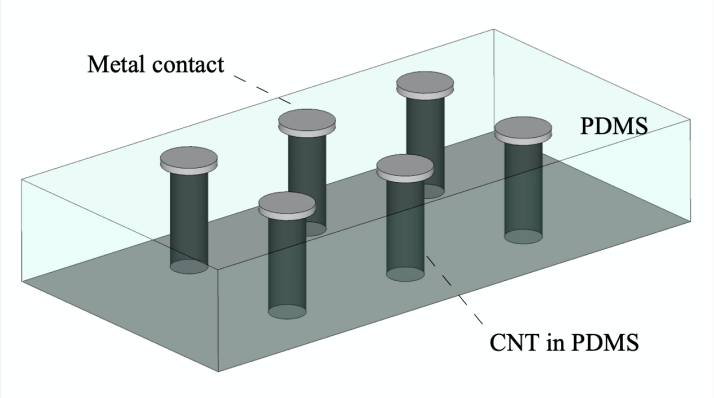

Figure 5.2: Schematic illustration of the flexible interposer. The through-hole vias are made by vertically aligned CNT bundles, penetrated by the PDMS polymer which also serves as the substrate for the interposer. The metal pads are the medium to connect the CNT bundles with the wires for packaging.

The aluminum contact is 2 μm in thickness.

5.3. FABRICATION

THE fabrication of the interposer involves growth of vertically aligned CNT bundles, penetration with PDMS to form the composite and metal pad patterning on the vias. The main fabrication steps, depicted in Figure 5.3, are as follows:

1. **Fe deposition and patterning**.

   As discussed in the previous chapter, CNT bundles are growing with the help of catalysts such as Fe. To prevent that the metal catalyst diffuses into the Si substrate, a barrier layer needs to be deposited before the Fe catalyst deposition. Similar to TiN used in the previous chapter, Al_2O_3 is another commonly used barrier layer. While the TiN layer is great for CNT growth of less than 70 μm in height, Al_2O_3 has been proved to be excellent for tall CNT growth[15], [17]. In this process, a 10 nm Al_2O_3 layer was deposited using reactive sputtering from a pure Al target. The CNTs were growing only in designed through hole via patterns, thus a patterned photoresist made by standard lithography process was conducted before the Fe deposition. The 1.5 nm Fe layer was then deposited on the patterned photoresist layer, followed by a lift off process with the same conditions which is also used in the fabrication process in the previous chapter.

2. **Synthesis of Vertically aligned CNT bundles**.

   The height of the CNT bundles is strongly dependent on the growing time. With 1.5 nm Fe catalyst layer and Al_2O_3 as the support layer, by measuring the CNT samples grew at different durations in the reactor at a fixed temperature of 650 °C, the relationship between the CNT bundle height and the growth time is as shown

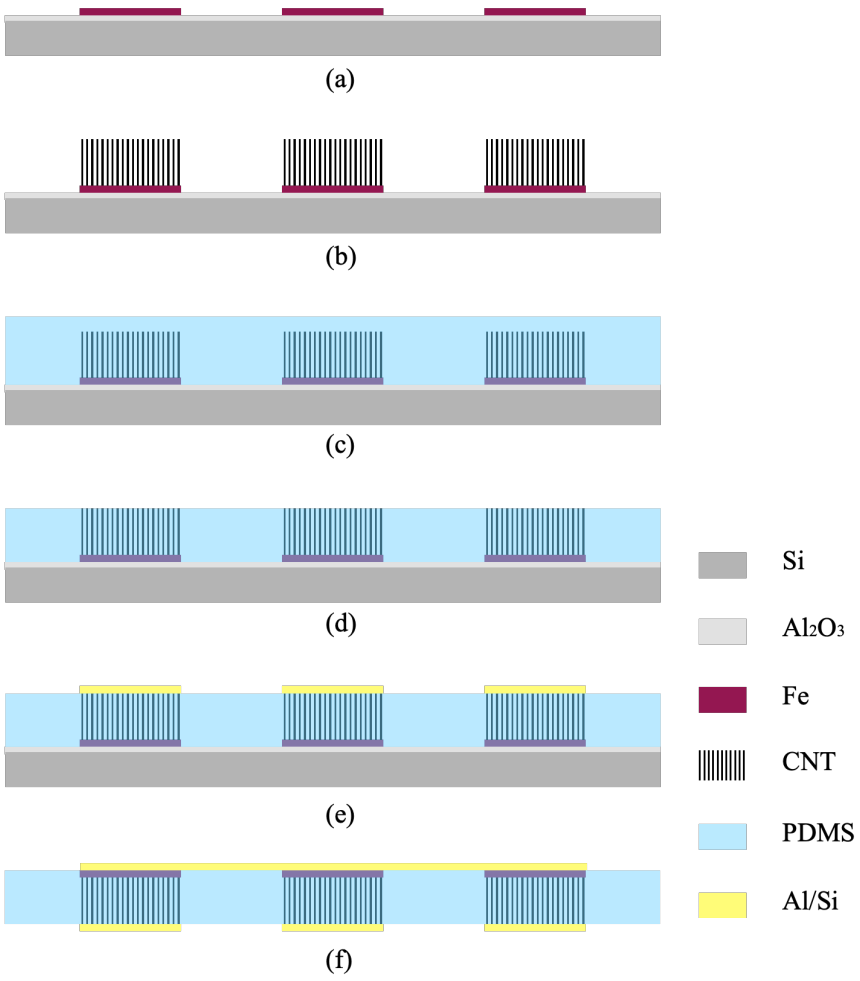

Figure 5.3: Illustration of the fabrication process: (a) Al_2O_3 deposition and Fe deposition and patterning for CNT growth; (b) Synthesis of vertically aligned CNT with height of 100 μm; (c) PDMS infiltration into the CNT bundles and curing of the polymer composite; (d) wet etching of the excess PDMS to expose the CNT tips for metal contact; (e) Deposit and pattern Al(1% Si) on the top; (f) Peel off the PDMS slab and flip it to expose the bottom part of CNT bundles, followed by sputtering Al(1% Si) for metal contact on the bottom part of the vias.

in Figure 5.4. The CNT grew with a relatively steep rate of around 1.2 μm/s at the beginning when the duration was no more than 120 sec. After around 120 sec, the growth rate slows down to about 0.9 μm/s. The measurement data are presented as the mean $\pm$ standard deviation ($\mu \pm \sigma$), while the mean is the average of the three times measurement, and the error bars indicate the standard deviation (σ). The plotted curve is without regression fitting, and the growth rates before and

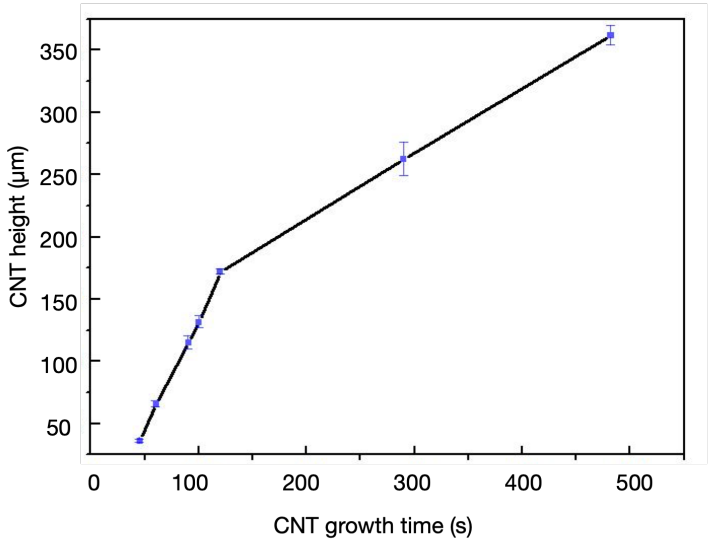

Figure 5.4: CNT height versus the growth time at 650 °C with 1.5 nm Fe as catalyst on Al_2O_3 support layer. The growth rate was around 1.2 μm/s at the beginning when growth time is less than 120 sec, the growth rate decreases to 0.9 μm/s as the growth time increases. The data are presented as the mean+ standard deviation ($\mu \pm \sigma$), without regression fit on the curve.

after 120 sec are based on the rough calculation.

SEM images of CNT bundles obtained at the temperature at 650 °C can be found in Figure 5.5. The bundles with different diameters can be found in Figure 5.5a. All the bundles appear to be straight, with no CNTs extruding outward from the bundles. The tips of the CNTs are even and flat in the close-up view in Figure 5.5b. The bottom part where CNTs grew on the substrate can be found in the close-up view in Figure 5.5c.

3. **PDMS penetration**

After the CNT synthesis, the PDMS was then poured on the CNT bundles for percolation. The PDMS was formed by Sylgard 184 prepolymer and curing agent, mixed at a standard ratio of 10:1. A thoroughly degassing process was required after the mixing, to prevent bubbles in the mixture from sticking to the CNT bundles. After degassing, the PDMS mixture was then poured on the wafer with CNT bundles. Another degassing process was conducted in the vacuum oven again to extract the air bubbles in the CNT bundles at room temperature. To get a uniform PDMS layer, the whole wafer was then moved to a spin coating machine running at a dominant speed for 60 seconds at 500 rpm, of which the detailed spinning speed can be found in Table 5.1. Higher PDMS thickness requires adjustment of the spinning speed and time, e.g. Table 5.2 shows spinning parameters for 200 μm PDMS

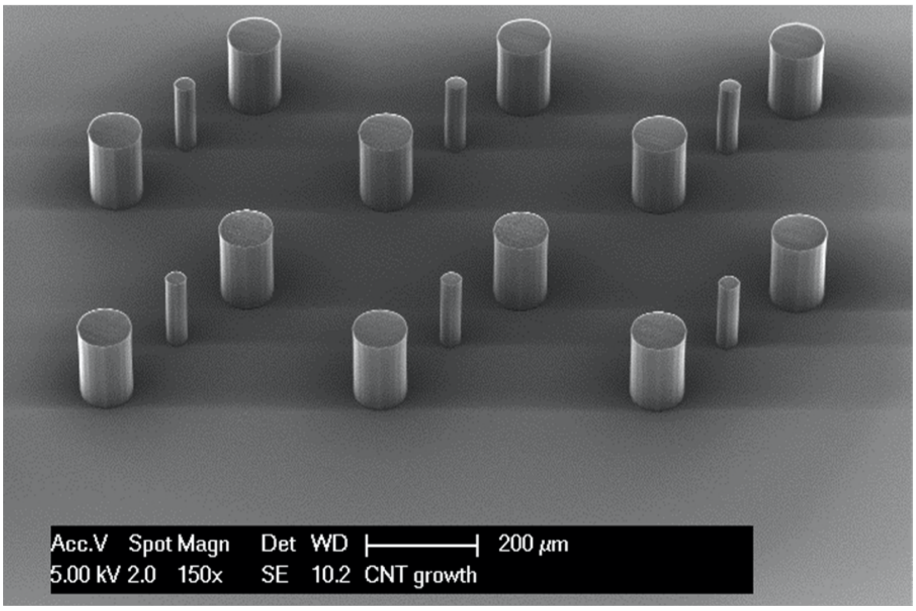

(a)

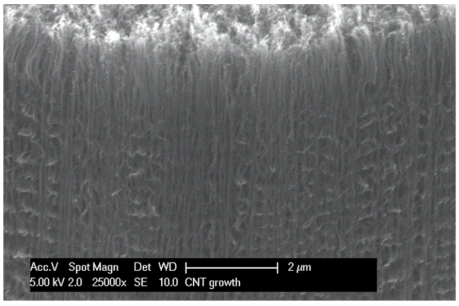

(b)

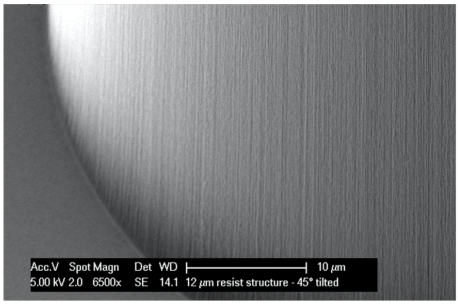

(c)

Figure 5.5: (a) SEM images of CNT bundles with different diameters grew at 650 °C, no tilted CNT tubes or deformed bundle were noticed; (b) close-up image of CNT tips which are even and flat; (c) bottom of the CNT bundle where CNTs grew on the Si substrate, the CNT tubes are well aligned.

membrane. After the spinning, the wafer was transferred into the oven to cure the PDMS at 65 °C for 1 hour.

4. **Etch the PDMS to expose the CNT bundle**

   In the previous step, the percolation of PDMS in the CNT also means the tips of the CNTs are covered by the PDMS, thereby after the PDMS penetration, the excess layer of PDMS on top of the CNT bundles needs to be removed so that the CNT tips

Spinning parameters for 100 μm PDMS membrane			
Step	**Speed (rpm)**	**Acceleration (rpm/s)**	**Time (s)**
Dispense	30	15	5
Spread	300	75	30
Spin	500	90	60

Spinning parameters for 200 μm PDMS membrane			
Step	**Speed (rpm)**	**Acceleration (rpm/s)**	**Time (s)**
Dispense	30	10	5
Spread	150	30	30
Spin	250	50	60

Table 5.1: Spinning parameters for PDMS membrane of 100 μm and 200 μm in thickness respectively

can be exposed and connected with metal pads afterward. An optimized etch rate of 0.33 μm/min can be achieved with a mixture of N-methyl pyrrolidinone (NMP) and tetra-butyl ammonium fluoride (TBAF) in a ratio of 3:1, respectively [18].

A steady etch rate of wet etching is critical for the PDMS etching results. In order to make sure the CNT tips are exposed, the PDMS covering the CNT must be removed so that the metal pads can connect with the CNT bundles. On the contrary, the overetching of the PDMS will remove too much of the PDMS material, causing cracks on the CNT bundle part. An uneven etched result is shown in Figure 5.6. Cracks can be found in the CNT bundle part as in (a), while small PDMS residuals can be found on the top of the bundle as in (b). The residual PDMS will block the contact between the metal and CNT tips. (c) Cracks of the CNT/PDMS as in Figure (c) will bring even more etching solution into the CNT bundle and further deteriorate the uneven etching; a close-up view of the crack shows that lots of detached CNT tubes in the cracks are not embedded in PDMS, yet there are PDMS residuals on the top of the bundle.

A moderate PDMS wet etching result was presented in Figure 5.7. (a) where all the CNT bundle tips can be observed by their clear shape on the PDMS surface without any cracks. A close-up view of the bundle top can be found in (b) that while the PDMS is etched, the CNT tips are exposed.

5. **Deposit and pattern Al(1% Si) contacts**

   A layer of 2 μm Aluminum with 1% Silicon was then sputtered on the top as the metal contact. The polymer easily gets burned during the sputtering process, thus only 500 nm Al was sputtered on the wafer and repeated four times which contributes to 2 μm Al in total.

   The Al(1% Si) layer was then patterned by plasma etching to form the metal contacts. As shown in Figure 5.8, the Al contact on each node is clean without any cracks, while the PDMS surface is also smooth without any wrinkles.

6. **Deposit and pattern Al(1% Si) on the backside**

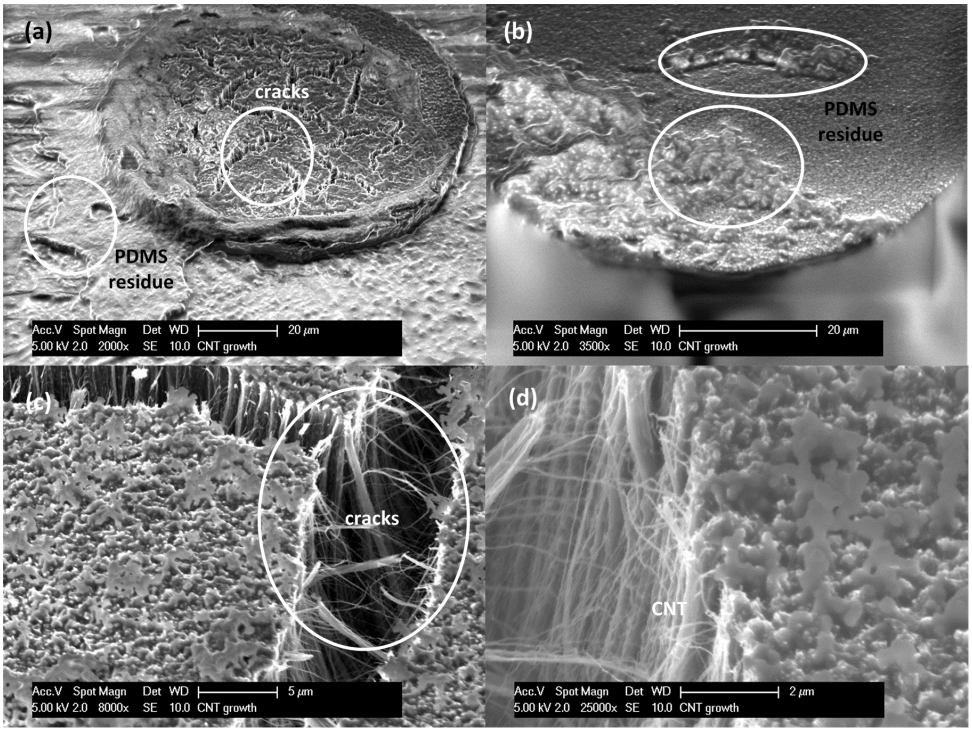

Figure 5.6: Failed etched results to emphasize that wet etching of PDMS is critical to get nice bundle and exposed CNT tips. (a) Overetching of the PDMS brings up the cracks in the bundle; (b) PDMS residuals on top of a bundle; (c) Cracks of the bundle will detoriate the uneven etching, (d) Some CNT tubes in the crack are not embedded in the PDMS, while there are still PDMS residuals on top of the bundle.

In order to sputter the metal contact layer on the backside, the wafer was peeled off from the original Si substrate and transferred to another Si wafer with the bottom part flipped to make sure the CNT vias exposed as frontside. Another layer of Al(1% Si) was sputtered and patterned on the bottom of the PDMS slab, with the same parameters as in the previous step. After finishing the process, the thin PDMS membrane with embedded CNT bundles and metal contacts was peeled off from the Si substrate. The thin membrane is easy to get wrinkled when peeling off. This can be avoided by placing the membrane in water to peel off and transfer it to the original substrate wafer for support.

5.4. FABRICATED DEVICE

THE fabricated device can be found in Figure 5.9. The device contains 2x3 units, each with 4 Al(1% Si) contacts on top of the CNT/PDMS composite. The etching of PDMS and Al(1% Si) appear to look clean and smooth, without clear damage on the surface. A close-up SEM image is shown in Figure 5.9(b). The Al(1% Si) has great coverage on the CNT bundles, with no extra CNT tips were exposed, which may bring issues to the

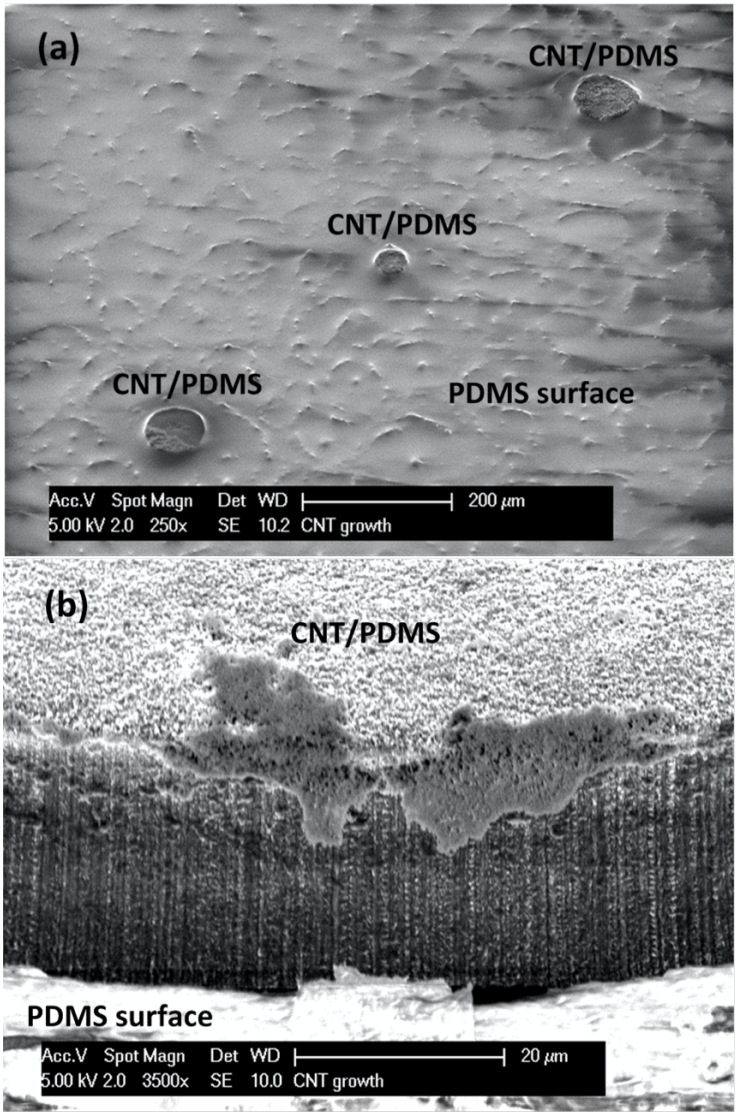

Figure 5.7: A fine PDMS wet etching result was presented. (a) all the CNT tips can be observed by their clear shape of the CNT bundles; (b) a close-up view shows that the PDMS surface is moderately etched, and the CNT tips are exposed with only very few PDMS redsidulas on the top of the bundle.

electrical property of the via.

CNT growth is dependent on various parameters. In addition to the catalyst and support layer materials, the growth rate and quality are highly related to the temperature during the synthesis. A moderate growth temperature helps to obtain a stable growth

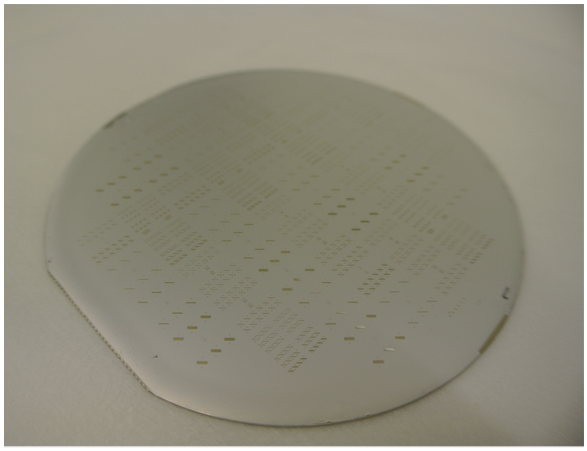

Figure 5.8: The wafer after the patterning of the Al(1% Si) for metal contacts. Al(1% Si) patterns on each node are clean without any cracks, while the sample surface is smooth without any wrinkles.

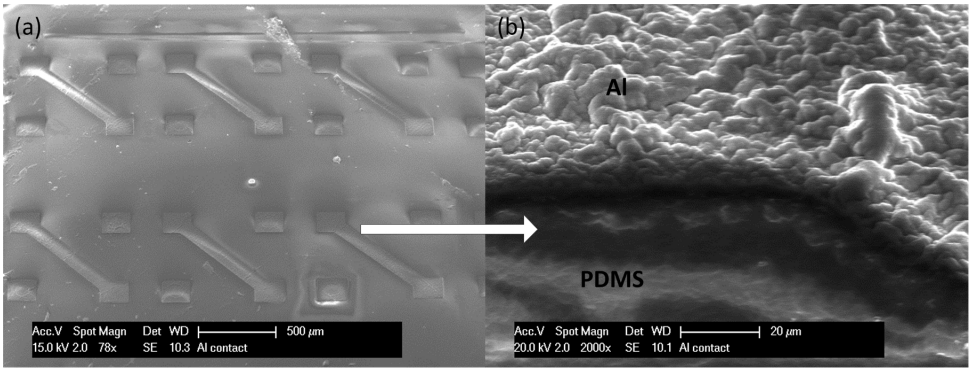

Figure 5.9: (a) Fabricated flexible vias with CNT/PDMS composite, with Al(1% Si) functioning as metal contact; (b) close-up SEM image of the Al(1% Si) coverage on the CNT bundle which was infiltrated in the PDMS.

rate and moderate quality for the CNTs [15]. As shown in Figure 5.10, four different CNT bundles were growing with the same support layer (Al_2O_3) and catalyst (Fe) for 60 seconds, but at different temperatures. Figure 5.10a shows that the CNTs growing at 500 °C has a length of only about 726 nm. At 550 °C, as in Figure 5.10b, the CNT bundle has a length of 8.4 μm, which is ten times higher than at 500 °C. Much taller CNT can be found in Figure 5.10c where CNT was grown at 600 °C, which led to a length of about 38.4 μm. When the temperature increased to 650 °C, the CNT retrieved a height of 113 μm, as shown in Figure 5.10d.

Raman spectroscopy has been used to investigate the quality of the four CNT groups growing at different temperatures. By checking the intensity ratio of D-band (around 1350 cm^{-1}, related to defects) and G-band (around 1582 cm^{-1}, Raman active mode of graphitic materials), also known as I_D and I_G. The smaller ratio of I_D/I_G is a good indi-

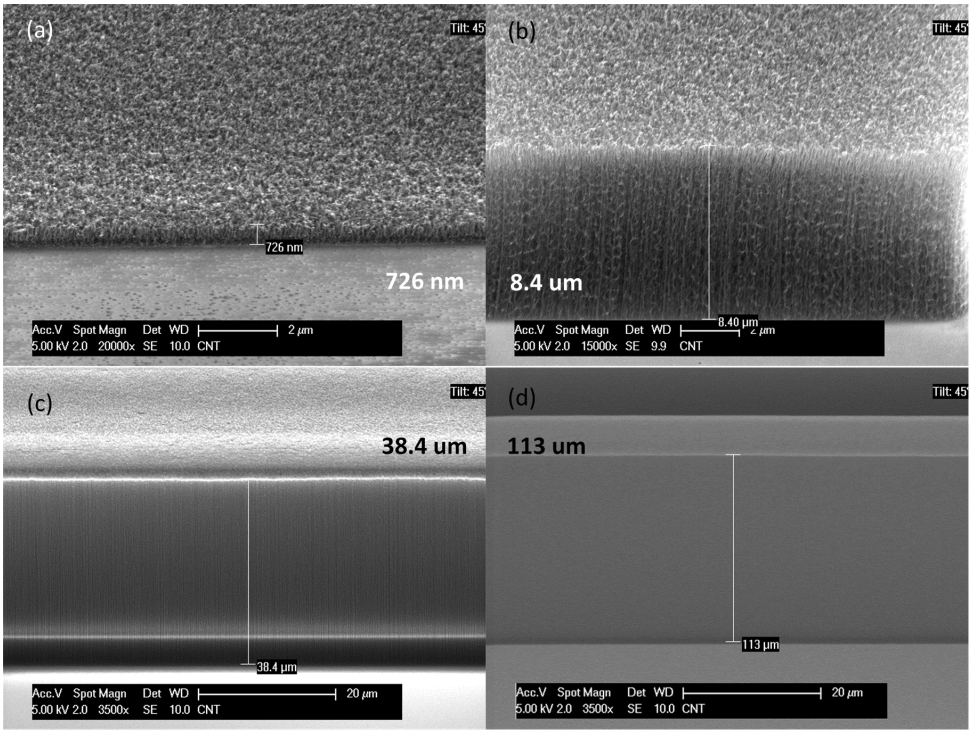

Figure 5.10: SEM images for CNT bundles grew for 60 seconds at four different temperatures using the same catalyst and support layer. (a) CNT grew at 500 °C has a length of only about 726 nm; (b) CNT grew at 550 °C has a length of 8.4 μm; (c) CNT grew at 600 °C has a length of 38.4 μm (d) CNT grew at 650 °C has a length of 113 μm.

cator for better CNT quality, a detailed explanation of the ratio and calculation can be found in Dr. Vollebregt's work [15]. As depicted in Figure 5.11, all four Raman shifts show the same pattern, while the ratio of I_D/I_G differs. With an I_D/I_G ratio of 1.53, the sample grown at 500 °C sample has the highest ratio among the four samples, as shown in Figure 5.11a; along with the increasing temperature, the I_D/I_G ratio are 1.47, 1.38 and 1.23 at 550 °C, 600 °C and 650 °C separately. The Raman spectra show that higher growing temperature contributes to a lower ratio of I_D/I_G, thereby a better CNT quality.

Since higher temperature promises lower I_D/I_G rate, meaning better CNT quality, we shall just choose the highest available temperature for the CNT synthesis. However, as discussed before, higher temperature also means the growth rate is higher. The growth rate for the temperature at 650 °C has reached 110 μm/min. In this work, we are investigating the CNT bundles to be 100 μm in height, thus temperature higher than 650 °C will make the CNT growing hard to control. Thus, the growth temperature of 650 °C was chosen for the growth rate and quality.

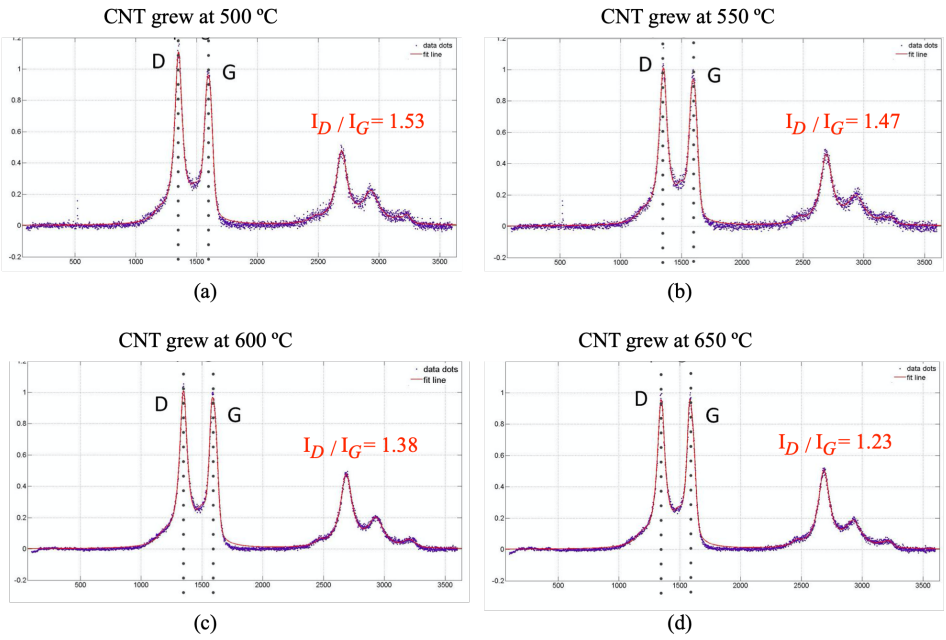

Figure 5.11: Raman spectra of four CNT groups growing at different temperatures. The I_D/I_G ratio are (a) 1.53, (b) 1.47, (c) 1.38 and (d) 1.23 at 500 °C, 550 °C, 600 °C and 650 °C separately. The Raman spectra shows that higher growing temperature contributes to a lower ratio of I_D/I_G, thereby a better CNT quality.

5.5. ELECTRIC CONDUCTIVITY OF THE CNT/PDMS COMPOSITE

To achieve the accurate measurements of the resistance, the four-point probe technique was used, as shown in Figure 5.12. To measure the resistance of the CNT/PDMS vias, two ends of the CNT bundle should be connected with measurement probes. Instead of using an extra conductive via, two other CNT bundles are functioning as the conductive vias for the measurement, indicated by 'CNT2' and 'CNT3'.

The four contacts in this figure are functioning as I_{out} , I_{in}, V_{high}, and V_{low} respectively. The driven current goes in from the point I_{in}, then goes through the CNT bundle in the center and followed by the other bundle ends at I_{out}. The potential drop on the center CNT bundle was then measured through the other two pads V_{high}, and V_{low}.

The equivalent circuit of the measurement is made as in Figure 5.13. In this method, the circuit consists of constants and CNT bundle related variable part. While the conductivity of the PDMS is only 2.5e-14 S/m[19], only the metal pads, contacts (where CNT connects with the metal pad) and CNT bundles are included in this model.

$$R_C = R_{contact} + R_{CNT} + R_{contact} \tag{5.1}$$

The I-V characteristics of CNT bundles were obtained from the four-point probe

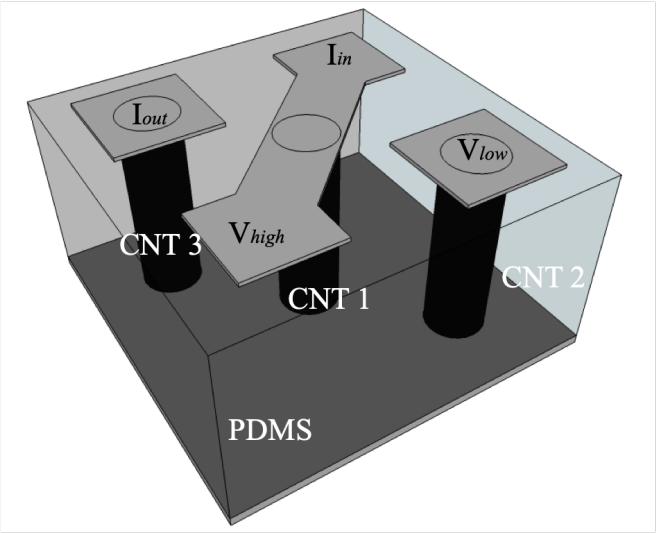

Figure 5.12: Four probe measurement structure for CNT vias. The driven current goes in from the point I_{in} through the CNT bundle in the center and followed by the other bundle ends at I_{out}. The potential drop on the center CNT bundle was then measured through the other two pads V_{high}, and V_{low}.

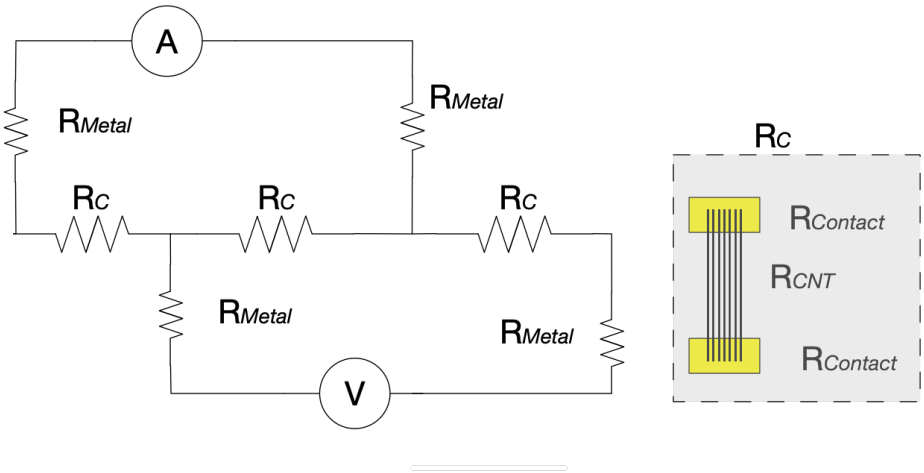

Figure 5.13: Equivalent circuit of the 4-probe measurement structure.

measurements. All the CNT bundles were grown at 650 °C, with the same length of 100 μm. Different bundle sizes, with a diameter of 50 μm, 80 μm, and 100 μm were made

for the test. As shown in Figure 5.14, the obtained I-V curve indicates different resistance of 1416 Ω, 462 Ω, and 297 Ω. The measured resistance includes the CNT/PDMS bundle and two times the contact resistance.

According to resistance Law, the electrical resistivity

$$\rho = R \times A/l \tag{5.2}$$

Thus the electrical resistivity of the three bundles are:

$$\begin{aligned} \rho_{50\mu m} &= R_{50\mu m} \times A_{50\mu m}/l \\ &= 1416 \times \pi \times (50/2 \times 10^{-6})^2 \times 100 \times 10^{-6} \\ &= 278\Omega m \end{aligned} \tag{5.3}$$

$$\begin{aligned} \rho_{80\mu m} &= R_{80\mu m} \times A_{80\mu m}/l \\ &= 462 \times \pi \times (80/2 \times 10^{-6})^2 \times 100 \times 10^{-6} \\ &= 232\Omega m \end{aligned} \tag{5.4}$$

$$\begin{aligned} \rho_{100\mu m} &= R_{100\mu m} \times A_{100\mu m}/l \\ &= 297 \times \pi \times (100/2 \times 10^{-6})^2 \times 100 \times 10^{-6} \\ &= 233\Omega m \end{aligned} \tag{5.5}$$

For top metal layer Al, with a thickness of 2 μm, a cross-section area of 502 μm^2, and electrical resistivity of $2.83 \times 10^{-8}\Omega m$. The bottom Au layer has an electrical resistivity of about $2.40 \times 10^{-8}\Omega m$. The resistance of top and bottom metal is calculated as 0.0566 Ω, and 0.06 Ω, respectively. These two resistances of metal are much lower compared with hundreds of Ohms of measured resistance, thus they can be ignored in the calculation.

In order to quickly verify the result, place the V_{low} probe to where contact I_{out} is, as shown in Figure 5.15(a). The measured resistance is 612 Ω, which includes two times the CNT bundles with a diameter of 100 μm. As shown in Figure 5.15(b), the resistance in the equivalent circuit is expected to be:

$$R_C = 2 \times (R_{contact} + R_{CNT} + R_{contact}) + R_{metal} \tag{5.6}$$

According to the Law of resistance, the resistance of the CNT bundle is dependent on the CNT length linearly:

$$R_{CNT} = 3.15 \times L_{CNT} - 18\Omega m \tag{5.7}$$

Extrapolating the CNT bundles to zero length, the resistance is -18 Ω, which is physically impossible. This can be explained by that the CNT tubes have uneven height, leading to their contacts with the metal partly buckle thus have different efficient lengths. This behavior also matches well with Dr. Vollebregt's found in his work on the CNT vias[15]. The relationship may be inaccurate to predict the exact resistance of the CNT bundles, however, it can be used to roughly evaluate the trend of the resistance for different CNT length.

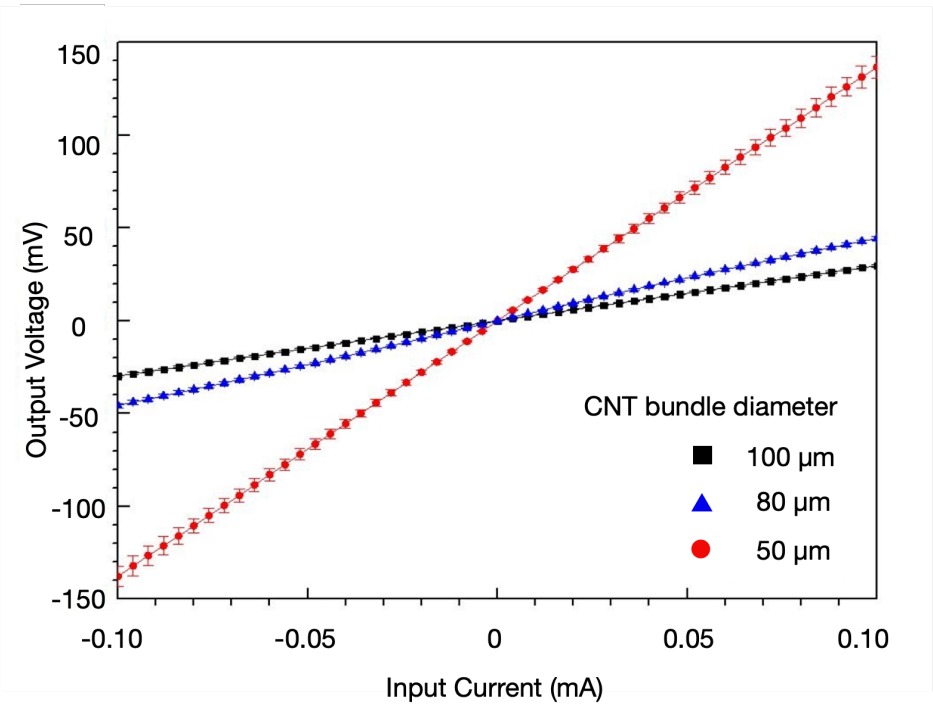

Figure 5.14: I-V characteristics obtained from CNT bundle diameters of 50 μm, 80 μm, and 100 μm separately. The curve indicates different resistance of 1416 Ω, 462 Ω, and 297 Ω separately.

5.6. DISCUSSION

THE electrical resistivity of the three vias are 278 Ωm, 232 Ωm, and 233 Ωm respectively. The electricial resistivity aligned well with each other, especially $\rho_{80\mu m}$ and $\rho_{100\mu m}$ are very close. There are several reasons that the small bundle diameter has slightly higher resistivity $\rho_{50\mu m}$:

1. The small CNT bundles are more sensitive to the uneven CNT tips. In the CNT/metal contact area, there are some tall tubes buckled, and short tips cannot reach to the metal contacts. A smaller CNT bundle has worse uniformity than the bigger bundles, which in turn led to fewer CNT tubes connected with the metal pads. With less contact of CNT tubes with the metal pads, the resistivity tends to be higher.

2. During the mask design of the CNT bundles, the round circles are formed by straight lines, as shown in Figure 5.16. When the designed circular shape has big diameter, the obtained shape area is close to the circle πR^2. The limitation of the mask design makes the small round bundles have less area of CNTs than the expected ⌀50 μm, thus the resistivity is higher. As the size goes down to, for instance ⌀20 μm, the straight lines can hardly align with the circle. This is also reflected by the

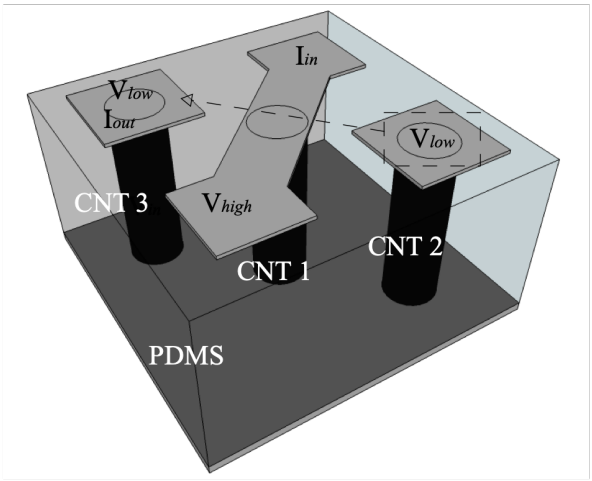

(a)

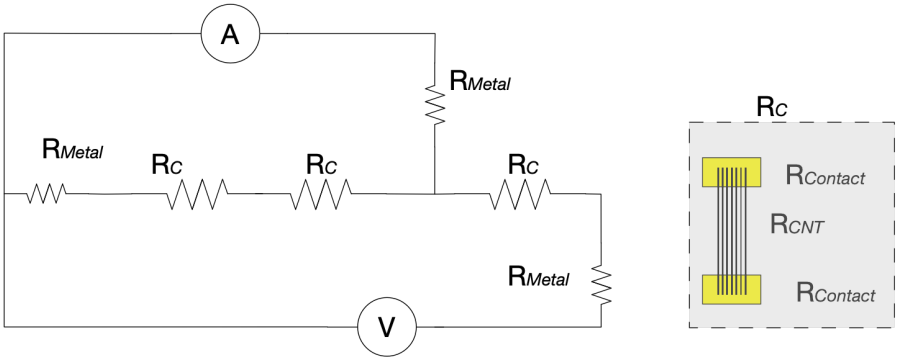

(b)

Figure 5.15: (a) By moving the V_{low} probe to the same metal pad as I_{out}, the measured resistance became two times the CNT bundles with extra metal contact; (b) the equivalent circuit.

fabricated CNT bundle shape, with clear edges, as shown in Figure 5.16b. A real bundle size of 50 μm in diameter has an area of

$$A_{50} = 8 \times R^2 \times (sin(22.5°) \times cos(22.5°) = 2.828 \times R^2 \tag{5.8}$$

Compared with the designed circular bundle size: πR^2

$$r_{50} = 2.828 \times R^2 / \pi R^2 = 0.90 \tag{5.9}$$

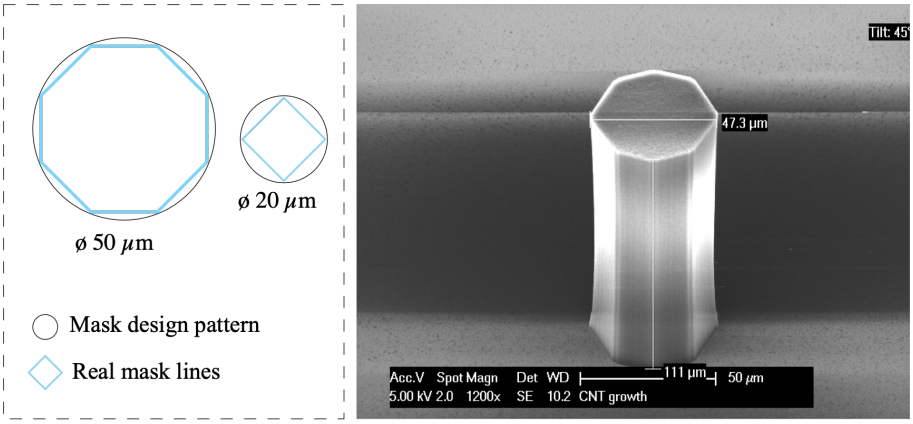

Figure 5.16: (a) The mask design for the round circles are formed by straight lines, which makes the real size of the bundles are less than the perfect round bundles. The limitation of the mask design makes the small round bundles have less area of CNTs than the expected ⌀50 μm, thus the resistivity is higher. (b), the fabricated CNT bundle has clear edges instead of a round shape.

While a real bundle size of 20 μm in diameter has an area of

$$A_{20} = 4 \times 1/2 \times R^2 = 2 \times R^2 \tag{5.10}$$

Compared with the designed circular bundle size: πR^2

$$r_{20} = 2 \times R^2 / \pi R^2 = 0.64 \tag{5.11}$$

As the diameter of the bundle size goes down, the obtained shape has a much smaller area than expected. This also led to a higher resistivity for smaller bundles.

A comparison of the resistivity from different materials are listed in Table 5.2. The resistivity of the composite is approximately 233 Ωm, compared with the vertically aligned

Material	**Resistivity (Ωm)**
CNT/PDMS	233
CNT [15]	0.94
CNT [20]	1.79×10^{-3}
Si [21]	640
PDMS[19]	4×10^{13}
Cu [21]	1.7×10^{-8}
Au [21]	2.44×10^{-8}

Table 5.2: Comparison of the resistivity with the other materials

CNT, this result is much higher than the pure CNT bundles in [15]and [20], though both references mentioned that the resistivity of the CNT bundles doesn't scale with the bundle diameter, yet the reported resistivity is in the same order with different bundle diameter. The reason which causes the resistivity in this work might be caused by the cracks on the top of the CNT bundles during the wet etching, as shown in Figure 5.6. The existence of the cracks results in less CNT the coverage by metal layer in the Al(1% Si) sputtering process, which led to a higher resistance observed. In another way, though it is also way much higher than Cu and Au, yet the existence of CNT makes it 10^{-10} times smaller than the resistivity of pure PDMS. To fix these two challenges, decorating the CNT with coatings such as Titanium shall help protect the CNT bundle top thus can avoid the cracking during the wet etching since Titanium is resistant to the NMP solution used in the wet etching of PDMS. Furthermore, the conductive Titanium material also helps to increase the conductivity of the bundle, a better conductive via makes this CNT/PDMS configuration closer to its real applications [16], [22], [23].

Besides the electrical property, the mechanical property of the composite is also essential to the interposer application. As the support and rerouting intermediate, steady mechanical reliability and thermal management are critical for the material. These are required to be investigated in future work.

5.7. CONCLUSION

IN summary, we proposed a new concept of using CNT/PDMS for flexible interposer. This concept is appealing to specific applications that require strong flexibility where rigid vias will easily get cracked when being bended or stretched [24].

The electrical property of the CNT/PDMS interconnection was investigated in this chapter. The resistivity of the composite is approximately 1e-10 times smaller than the resistivity of PDMS, yet its electrical performance falls short of expectations, thus further research is required to improve the material, e.g., by coating materials on CNT bundles to improve the coverage of the metal contact coverage on the vias. Mechanical property is also required to be investigated for the material in future work.

REFERENCES

[1] Y. Shen, *Flexible Interposer Based on Carbon Nanotubes and PDMS Composite,* (2015).

[2] C. Yu, Z. Duan, P. Yuan, Y. Li, Y. Su, X. Zhang, Y. Pan, L. L. Dai, R. G. Nuzzo, Y. Huang, H. Jiang, and J. A. Rogers, *Electronically programmable, reversible shape change in two- and three-dimensional hydrogel structures,* Advanced Materials **25**, 1541 (2013).

[3] T. Sekitani and T. Someya, *Stretchable, large-area organic electronics,* (2010).

[4] C. Lian, M. Piksa, K. Yoshida, S. Persheyev, K. J. Pawlik, K. Matczyszyn, and I. D. W. Samuel, *Flexible organic light-emitting diodes for antimicrobial photodynamic therapy,* npj Flexible Electronics **3**, 1 (2019).

[5] S. W. Jin, J. Park, S. Y. Hong, H. Park, Y. R. Jeong, J. Park, S. S. Lee, and J. S. Ha, *Stretchable Loudspeaker using Liquid Metal Microchannel,* Scientific Reports **5**, 1 (2015).

[6] D. J. Lipomi, M. Vosgueritchian, B. C. Tee, S. L. Hellstrom, J. A. Lee, C. H. Fox, and Z. Bao, *Skin-like pressure and strain sensors based on transparent elastic films of carbon nanotubes,* Nature Nanotechnology (2011), 10.1038/nnano.2011.184.

[7] S. Biswas, A. Schoeberl, Y. Hao, J. Reiprich, T. Stauden, J. Pezoldt, and H. O. Jacobs, *Integrated multilayer stretchable printed circuit boards paving the way for deformable active matrix,* Nature Communications **10**, 1 (2019).

[8] J. Vanfleteren, M. Gonzalez, F. Bossuyt, Y. Y. Hsu, T. Vervust, I. De Wolf, and M. Jablonski, *Printed circuit board technology inspired stretchable circuits,* MRS Bulletin **37**, 254 (2012).

[9] K. Pitschmann, D. Wagner, S. Brinkhues, B. Schmidt, and M. Detert, *Highly flexible and biocompatible interposer for medical applications,* Proceedings of the International Spring Seminar on Electronics Technology **2016-Septe**, 71 (2016).

[10] J. Maeng, B. Kim, D. Ha, and W. J. Chappell, *Parylene Interposer as Thin Flexible 3-D Packaging Enabler for Wireless Applications,* IEEE Transactions on Microwave Theory and Techniques **59**, 3410 (2011).

[11] A. Usman, E. Shah, N. B. Satishprasad, J. Chen, S. A. Bohlemann, S. H. Shami, A. A. Eftekhar, and A. Adibi, *Interposer Technologies for High-Performance Applications,* IEEE Transactions on Components, Packaging and Manufacturing Technology **7**, 819 (2017).

[12] B. Khorramdel, J. Liljeholm, M.-M. Laurila, T. Lammi, G. Mårtensson, T. Ebefors, F. Niklaus, and M. Mäntysalo, *Inkjet printing technology for increasing the I/O density of 3D TSV interposers,* Microsystems & Nanoengineering **3**, 17002 (2017).

[13] J. H. Kim, J. Y. Hwang, H. R. Hwang, H. S. Kim, J. H. Lee, J. W. Seo, U. S. Shin, and S. H. Lee, *Simple and cost-effective method of highly conductive and elastic carbon nanotube/polydimethylsiloxane composite for wearable electronics,* Scientific Reports **8**, 1 (2018).

[14] L. Cai and C. Wang, *Carbon Nanotube Flexible and Stretchable Electronics,* Nanoscale Research Letters **10** (2015), 10.1186/s11671-015-1013-1.

[15] S. Vollebregt, F. D. Tichelaar, H. Schellevis, C. I. M. Beenakker, and R. Ishihara, *Carbon nanotube vertical interconnects fabricated at temperatures as low as 350 °c,* Carbon **71**, 249 (2014).

[16] R. H. Poelma, B. Morana, S. Vollebregt, E. Schlangen, H. W. van Zeijl, X. Fan, and G. Q. Zhang, *Tailoring the Mechanical Properties of High-Aspect-Ratio Carbon Nanotube Arrays using Amorphous Silicon Carbide Coatings,* Advanced Functional Materials **24**, 5737 (2014).

[17] S. Esconjauregui, M. Fouquet, B. C. Bayer, C. Ducati, R. Smajda, S. Hofmann, and J. Robertson, *Growth of ultrahigh density vertically aligned carbon nanotube forests for interconnects,* ACS Nano (2010), 10.1021/nn1025675.

[18] B. Balakrisnan, S. Patil, and E. Smela, *Patterning PDMS using a combination of wet and dry etching,* Journal of Micromechanics and Microengineering (2009), 10.1088/0960-1317/19/4/047002.

[19] A. Todri-Sanial, J. Dijon, and A. Maffucci, *Carbon nanotubes for interconnects: Process, design and applications,* Carbon Nanotubes for Interconnects: Process, Design and Applications , 1 (2016).

[20] C.-T. Lin, C.-Y. Lee, T.-S. Chin, R. Xiang, K. Ishikawa, J. Shiomi, and S. Maruyama, *Anisotropic electrical conduction of vertically-aligned single-walled carbon nanotube films,* Carbon **49**, 1446 (2011).

[21] R. A. Serway and J. R. Gordon, *Principles of Physics*, Principles of Physics No. v. 2 (Saunders College Pub., 1998) p. 602.

[22] X. Zang, C. Shen, E. Kao, R. Warren, R. Zhang, K. S. Teh, J. Zhong, M. Wei, B. Li, Y. Chu, M. Sanghadasa, A. Schwartzberg, and L. Lin, *Titanium Disulfide Coated Carbon Nanotube Hybrid Electrodes Enable High Energy Density Symmetric Pseudocapacitors,* Advanced Materials **30** (2018), 10.1002/adma.201704754.

[23] X. Gao, Y. Huang, X. He, X. Fan, Y. Liu, H. Xu, D. Wu, and C. Wan, *Mechanically enhanced electrical conductivity of polydimethylsiloxane-based composites by a hot embossing process,* Polymers **11** (2019), 10.3390/polym11010056.

[24] E. C. Nyns, R. H. Poelma, L. Volkers, J. J. Plomp, C. I. Bart, A. M. Kip, T. J. van Brakel, K. Zeppenfeld, M. J. Schalij, G. Q. Zhang, A. A. de Vries, and D. A. Pijnappels, *An automated hybrid bioelectronic system for autogenous restoration of sinus rhythm in atrial fibrillation,* Science Translational Medicine **11**, 1 (2019).

6

Conclusions And Outlook

The concept of *More than illumination* for solid state lighting (SSL) development can be interpreted in different packaging levels. An SSL system is in principle a micro electronic optical system. The similarity of SSL with microelectronics made MEMS integration with SSL a logical step. This thesis presents several MEMS solutions to different packaging levels of SSL applications. Different topics, ranging from tunable optics to particle sensors, from which extended research was also conducted.

6.1. TUNABLE OPTICS

TUNABLE optics for dynamic lighting is explored in two different packaging levels in this thesis. A tunable optical system that can be mounted directly on the currently available light source is introduced in chapter 2. The system consists of a biconvex lens with a fixed focal length and a magnetic actuator. The biconvex lens was driven by the magnetic actuator along the focal length to shape the beam of the light source. In chapter 4, a smaller size flat fresnel lens with an adjustable focal length is presented. This diffractive optics changes its focal length based on the radial deformation of the device. The flat lens can be integrated with LED chips which makes it a lower level packaging.

6.1.1. TUNABLE OPTICAL SYSTEM

A tunable optics with a flexible actuator was demonstrated in chapter 2. Light distribution, specifically different outgoing angles from 22° to 16.2°, was achieved by applying direct current (DC) input to control the distance of the optics from the light source.

The actuation mechanism in this work is based on electromagnetic actuation. The actuator with copper coil on a polyimide substrate was fabricated using standard flexible PCB fabrication. In this work, we use one polyimide layer with Cu coils on both sides to drive the lens. Large displacement was achieved with the two layers of coils. In order to achieve more significant displacement, more layers of coils on multi-layer of polyimide/Cu can be stacked together to function the actuation.

The concept of this work can be applied to broader applications, such as collimator. Furthermore, in applications with stricter requirements on the compact size, the magnet used in this system can be replaced with another current carrying coil as the source of Lorentz force. With one of the coils fixed, by applying opposite DC input, the other coil plate can be driven in the same behavior.

6.1.2. FLAT LENS

In chapter 4 we reported, for the first time, a flat binary lens with a tunable focal length, made by CNT/PDMS composite. The demonstrated lens has a static focal length of 7 mm. A massive focus change ($\geq$ 24%) was achieved by stretching lenses up to 11.4%.

The key to the fabrication of the lens array is the growth of patterned CNTs. Vertically aligned CNT bundles were grown at a temperature of 550 °C in 10 min, which led to a bundle height of 10 μm with 93.9% pf transmittance. This makes a high contrast with the transmittance of PDMS (0.06%) and contributes good optical performance of the optics.

The CNT inside the PDMS remains well aligned after the PDMS percolation, thus maintaining the CNT patterns and the excellent optical absorption properties. Further-

more, the thorough penetration of PDMS promises good flexibility for the composite, which is essential for the tuneability of the lens.

The focal length change is achieved by stretching the lens radially. During the stretching of the lens, astigmatism is observed. This is due to the non-uniform clamping of the lens in the sample holder. The diffractive patterns are very susceptible to the uniformity of the Fresnel lens. We recommend integrating an actuator that can provide a uniform radial deformation of the lens, which doesn't require mechanical clamps.

The CNT/PDMS configuration is also applicable for different focal lengths for the multi-focus contact lens application. The opaque area in the binary amplitude Fresnel lens will cause the loss of incoming light. A trade-off between the multi focus function and incoming light must be considered.

6.2. $PM_{2.5}$ SENSOR

APART from the tunable optics application, in chapter 3 we explored the solution to integrate with sensors that can be applied in a lighting sensory network. The fabricated particle sensor observes the scattered light triggered by particles in a microchamber. The principle is validated by exposing the sensor to cigarette smoke, one of the most common sources of PM2.5. Preliminary measurements have demonstrated that the device is capable of detecting the presence of cigarette smoke. The sensor output (1.235V) is in a factor of 4.47% higher in the presence of cigarette smoke than in clean air [1].

The MEMS PM sensor can respond differently to particles of varying compositions and the MEMS device will require a separate mass calibration factor for specific aerosols. In this work, only the design, fabrication and measurement principle of the sensor is presented. The calibration of the device requires extensive work and has been mentioned in Dr. Mingzhi Dong's work[2].

6.3. CNT/PDMS COMPOSITE

INSPIRED by the CNT/PDMS composite used in the fresnel lens in chapter 4, the electrical property of the CNT/PDMS interconnection was investigated in chapter 5 to explore its potential application as an interposer.

CNT with 10 μm and 100 μm in height were fabricated using different methods in the thesis. For the micro Fresnel lens application, the requirements on the CNT is focused on its optical property. The height of 10 μm for the flat lens application was chosen due to that CNT at this height has low transmittance. Ti/TiN (10nm/50nm) substrate was used and the sample grew at 550 °C for 10 min. While for interposer application, CNT's electrical property was explored, and 100 μm is used for demonstration purposes, a 10 nm Al_2O_3 layer was used as the substrate, and the sample grew at 650 °C for 10min.

The resistivity of the composite is approximately 1×10^{-10} times smaller than the resistivity of PDMS, yet its electrical performance falls short of expectations. Its resistivity is approximately 233 Ωm, compared with the vertically aligned CNT, this result is much higher than the pure CNT bundles in [3]and [4], though both references mentioned that the resistivity of the CNT bundles doesn't scale with the bundle size. The reason might be caused by the cracks on the top of the CNT bundles during the wet etching. The existence of the cracks results in less CNT the coverage by metal layer in the Al(1% Si)

sputtering process, which led to a higher resistance.

Further investigation is required to improve the electrical performance of the composite. Decorating the CNT with coatings such as Titanium shall help protect the CNT bundle top thus can avoid the cracking during the wet etching since Titanium is resistant to the NMP solution used in the wet etching of PDMS. Furthermore, the conductive Titanium material also helps to increase the conductivity of the bundle, a better conductive via makes this CNT/PDMS configuration closer to its real applications [5–7].

Besides the electrical property, the mechanical property of the composite is also essential to the interposer application. As the support and rerouting intermediate, steady mechanical reliability and thermal management are critical for the material. These are required to be investigated in future work.

REFERENCES

[1] X. Li, E. Iervolino, F. Santagata, J. Wei, C. A. Yuan, P. Sarro, and G. Zhang, *Miniaturized particulate matter sensor for portable air quality monitoring devices,* in *IEEE SENSORS 2014 Proceedings* (IEEE, 2014) pp. 2151–2154.

[2] M. Dong, *TU Delft*, Ph.D. thesis, TU Delft (2016).

[3] S. Vollebregt, F. D. Tichelaar, H. Schellevis, C. I. M. Beenakker, and R. Ishihara, *Carbon nanotube vertical interconnects fabricated at temperatures as low as 350 °c,* Carbon **71**, 249 (2014).

[4] C.-T. Lin, C.-Y. Lee, T.-S. Chin, R. Xiang, K. Ishikawa, J. Shiomi, and S. Maruyama, *Anisotropic electrical conduction of vertically-aligned single-walled carbon nanotube films,* Carbon **49**, 1446 (2011).

[5] R. H. Poelma, B. Morana, S. Vollebregt, E. Schlangen, H. W. van Zeijl, X. Fan, and G. Q. Zhang, *Tailoring the Mechanical Properties of High-Aspect-Ratio Carbon Nanotube Arrays using Amorphous Silicon Carbide Coatings,* Advanced Functional Materials **24**, 5737 (2014).

[6] X. Gao, Y. Huang, X. He, X. Fan, Y. Liu, H. Xu, D. Wu, and C. Wan, *Mechanically enhanced electrical conductivity of polydimethylsiloxane-based composites by a hot embossing process,* Polymers **11** (2019), 10.3390/polym11010056.

[7] X. Zang, C. Shen, E. Kao, R. Warren, R. Zhang, K. S. Teh, J. Zhong, M. Wei, B. Li, Y. Chu, M. Sanghadasa, A. Schwartzberg, and L. Lin, *Titanium Disulfide Coated Carbon Nanotube Hybrid Electrodes Enable High Energy Density Symmetric Pseudocapacitors,* Advanced Materials **30** (2018), 10.1002/adma.201704754.

ACKNOWLEDGEMENTS

The four-year PhD term is a unique chapter in my life. Throughout these years, I've met lots of people that have contributed to this experience. Without them, this thesis could not have been accomplished.

First and foremost, I would like to thank my promoter, Prof. Kouchi Zhang. Kouchi has been helping me formulate the research questions and methodology. The way he pushed me to take initiatives on the project management and improve my communication skills benefits me not only with my research, but also my current career in industry.

The four-year PhD experience was stressful for me. I am indebted to my co-promoter Prof. Lina Sarro, who has never stopped to give me the most generous support and encouragement. Without her help, my PhD period would have been more frustrating and miserable.

My PhD journey started from an interview with Jia, Cadmus, Sau and Prof. Kees Beenakker. I am grateful that they handed me the key to this experience. Jia and Qinwen not only guided me the way to Delft, but also brought two lovely cats to my life.

I wish to thank the members of my dissertation committee: Prof. Paddy French, Prof. Willem van Driel, Dr. Sten Vollebregt, Prof. Xuejun Fan, and Prof. Chris Bailey, for generously offering your time to participate the defense.

A special thank goes to Sten, the master of carbon, who has also helped me a lot with the black magic fabricating CNTs, and offered massive help to review this thesis.

In ECTM, no one can survive without *Dr. Henk*, who absorbs energy from *waffee* (water+coffee) and transformed them into insightful advice on the processing techniques. I am also grateful that Henk sacrificed his holiday time to offer massive help for reviewing this dissertation.

My gratitude extends to Marian and Bianca. They are the moms of ECTM, who organize everything in good order.

Most of the work in this thesis was carried on in the cleanroom. Great thanks to the cleanroom staff, Gregory, Silvana, Tom, Mario, Johannes, Joost, Koos, Robert, Loek, Alex, Cassan, Johan, Jan Cornelis, Jan, Ron, and Wim. Thank you all for your help to guarantee the machines running.

Regarding the collaboration in this thesis, lots of credits are going to my project partners. Elina and Fabio took the initiative on the particle detector project and provided lots of detailed ideas. Prof. Paul Urbach and Dr. Lei Wei contributed lots of time helping with the optical measurements in the flat lens project.

I would like to thank the cool people who I could spend time with. Pengfei is not only good at research but also finding authentic Chinese restaurants. Jin is the friend that I can always chat with, although she once picked a terrible movie Godzilla, which traumatized our movie buddy Aslihan and me badly. Lin is the walking Wikipedia who teaches me lots of lifehacks. Amir is the king of party, hanging out with him is always full of joy. It's always cool to hang out with an artsy friend like Violeta, who is also a sweet

and wild Berliner. Aleksandar is the greatest officemate who brought me hair gel when mine is running out. Joost provides me lots of advice about workouts. Yelena organizes excellent parties. Rene never fails to surprise me with his insightful thinking on every single problem.

Speaking the same language in a foreign country helps me to relieve my homesickness. Yingjie, Jing, Pan, Jianlin, Huaiyu, Jiaqi, Teng Ma, Mingzhi, Alice, Boyao, Hongyu, Daniel, Jian Li, Bo Sun, Hao Zhang, Xin Guo, Yuan Gao, Qiyu, Yiming, Yu Xin, Caroline, and Thomas, thank you for bringing me the great time.

Our colleagues are the ones who contribute to the incredible working environment in ECTM. Zahra, Maryam, Yorick, Manju, Luke, Amir, Brahim, Andrei, Robert, Cinzia, Hong Wah, Miki, Joan, Hang, Marta, Bruno, Niko, William, Paolo. You all have contributed to this thesis, though not always explicitly.

Right after I arrived Delft, I happened to join a board game community where I found the awesome board game buddies, Zhen Yang, Lin Xiao, Ming Li, Yuling, Xin Li, Xin Tian, Jinhu, Feifei, Xiaocheng, Jingyu, Xiaowei, Cui Wei. Thank you for the great time playing all types of board games, and of course, enjoying different kinds of Chinese cuisines.

A special thank goes to Gijs Romain, who helped with the Dutch translation in this thesis.

I've always been feeling lucky that I have found my better half, who shares my joy when I am happy and holds my hands when I am down. Endre, thank you for making the home a place that we feel comfortable, and I cannot wait to continue traveling around the world with you.

来荷多年，比我更爱惜我的，是远在家乡的父母。感谢爸妈多年的关心与疼爱。人的一生，会遇到各式各色的精彩，也必然会有不期而遇的挫折，我很庆幸能够一直有你们为我加油，为我喝彩。

APPENDIX-A

LINEAR CHANGE OF R WHEN STRETCHING IN CHAPTER 4

ACCORDING to

$$r_n^2 = nf\lambda \tag{6.1}$$

For each ring, the radius is

$$r_1 = \sqrt{f\lambda} \tag{6.2}$$

$$r_2 = \sqrt{2f\lambda} \tag{6.3}$$

$$r_3 = \sqrt{3f\lambda} \tag{6.4}$$

...

$$r_n = \sqrt{nf\lambda} \tag{6.5}$$

To investigate the changing of the radius:

$$\frac{r_n}{r_1} = \frac{\sqrt{nf\lambda}}{\sqrt{f\lambda}} = \sqrt{n} \tag{6.6}$$

Which is a constant.

While after stretching,

$$r_1' = xr_1 \tag{6.7}$$

$$r_n' = xr_n \tag{6.8}$$

so we can get

$$\frac{r_n'}{r_1'} = \frac{xr_n}{xr_1} = \frac{\sqrt{nf\lambda}}{\sqrt{f\lambda}} = \sqrt{n} \tag{6.9}$$

which doesn't change, and

$$f' = \frac{r'^2}{n\lambda} = x^2 f \tag{6.10}$$

which means when stretching the sample uniformly from r to xr, the focal length f will increase to $x^2 f$.

APPENDIX-B

ASTIGMATISM IN THE OBSERVED DIFFRACTION PATTERNS IN CHAPTER 4

THE focal length information is obtained by visual inspection of the diffraction patterns at different distances between the lens and CCD camera. The focal length is read from the translational stage. Figure 4.3 shows the diffraction patterns at different distances between the lens and CCD camera for small lens strains of respectively 0%, 1.9% and 3.8%. Figure 4.13 shows the focal length information for larger strains ranging from 0% to 15.2%, with increment of 1.9%. The focus position with astigmatism depicted in Figure 6.1 can be determined when the two axes of the cross are symmetric. When out of focus, an ellipse with a major axis appears, as described in reference [1].

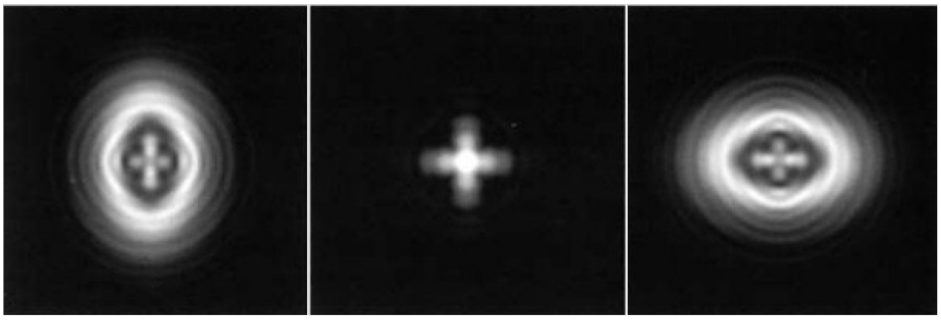

Figure 6.1: The focus position with astigmatism can be determined when the two axes of the cross are completely symmetric(center), while when out of focus (left, right), an ellipse with major axis appears.

REFERENCES

[1] I. Morison, *Star testing a telescope,* Popular Astronomy **January-Ma**, 12 (2009).

CURRICULUM VITÆ

Xueming LI

25-06-1987 Born in Pingxiang, Jiangxi, China.

EDUCATION

2005–2009 BSc. Electronics Science & Technology
China University of Mining and Technology

2009 – 2012 MSc. Microelectronics
Peking University
Thesis: Micro Electroporation Chip Integrated With Dielectrophoretic Sorting Based On Cell Viability
Promotor: Prof. dr. Zhihong Li

2012 PhD. Microelectronics
Delft University of Technology
Thesis: MEMS Solutions For More Than Illumination
Promotor: Prof. dr. Kouchi (G.Q.) Zhang
Copromotor: Prof. dr. Lina (Pasqualina M.) Sarro

LIST OF PUBLICATIONS

7. **Xueming Li**, Wei Lei, Poelma H. René, Vollebregt Sten, Wei Jia, Hendrik Paul Urbach, Pasqualina M. Sarro and Guo Qi Zhang, *Stretchable Binary Fresnel Lens for Focus Tuning*, Scientific Reports **6**, 25348 (2016).

6. **Xueming Li**, Wei Lei, Vollebregt Sten, Poelma H. René, Yingjie Shen, Wei Jia, Hendrik Paul Urbach, Pasqualina M. Sarro and Guo Qi Zhang, *Tunable binary Fresnel lens based on stretchable PDMS/CNT composite*, 2015 Transducers - 2015 18th International Conference on Solid-State Sensors, Actuators and Microsystems (TRANSDUCERS) **2041-2044**, (2015).

5. **Xueming Li**, Elina Iervolino, Fabio Santagata, Wei Jia, C. A. Yuan, Pasqualina M. Sarro and Guo Qi Zhang *Miniaturized particulate matter sensor for portable air quality monitoring devices*, SENSORS, 2014 IEEE, Valencia, pp. **2151-2154**, (2014).

4. Zewen Wei and **Xueming Li***, Deyao Zhao, HaoYan, Zhiyuan Hu, Zicai Liang and Zhihong Li, *Flow-through cell electroporation microchip integrating dielectrophoretic viable cell sorting*, Analytical chemistry **86**, 10215–22 (2014). *Coauthor

3. Teng Ma, **Xueming Li**, Wei Jia, Guo Qi Zhang and Pasqualina M. Sarro, *Numerical modeling of flexible actuator for dynamic lighting*, 2014 15th International Conference on Thermal, Mechanical and Mulit-Physics Simulation and Experiments in Microelectronics and Microsystems (EuroSimE), Ghent, pp. **1-4**, (2014).

2. **Xueming Li**, Wei Jia, Teng Ma, C. A. Yuan, Pasqualina M. Sarro, and Guo Qi Zhang, *Compact tunable optics for dynamic lighting*, Classical Optics 2014, OSA Technical Digest (online) (Optical Society of America, 2014), pp. **JTu5A.35**, (2014).

1. **Xueming Li**, Zewen Wei, Deyao Zhao, HaoYan, Zicai Liang and Zhihong Li, *A flow-through electroporation chip integrated with viable cell sorting based on dielectrophoresis*, 2012 IEEE 25th International Conference on Micro Electro Mechanical Systems (MEMS), Paris, pp. **993-996**, (2012).